

1 **SSWD-EvoEpi: A Coupled Eco-Evolutionary**
2 **Epidemiological Model**
3 **for Sea Star Wasting Disease in *Pycnopodia***
4 ***helianthoides***

5 Technical Report — Model Development and Sensitivity Analysis

6 Willem Weertman^{1,2}

¹Department of Psychology, University of Washington, Seattle, WA

²Friday Harbor Laboratories, University of Washington, Friday Harbor, WA

7 February 21, 2026

8 **Abstract**

9 Sea star wasting disease (SSWD) caused one of the largest wildlife mass mor-
10 tality events in marine ecosystems, driving the sunflower sea star (*Pycnopodia he-*
11 *lianthoides*) to a 90.6% range-wide decline and IUCN Critically Endangered sta-
12 tus. The recent identification of *Vibrio pectenicida* strain FHCF-3 as a causative
13 agent, combined with active captive breeding and the first experimental outplanting
14 of captive-bred juveniles, creates an urgent need for quantitative tools to guide
15 recovery. We present SSWD-EvoEpi, an individual-based, spatially explicit eco-
16 evolutionary epidemiological model coupling *V. pectenicida* transmission dynamics
17 with polygenic host evolution under sweepstakes reproductive success. Each agent
18 carries a diploid genotype across 51 loci governing three fitness-related traits — re-
19 sistance (immune exclusion), tolerance (damage limitation), and recovery (pathogen
20 clearance) — that evolve in response to disease-driven selection. Disease dynam-
21 ics follow an SEIR-type compartmental structure with an environmental pathogen
22 reservoir, pathogen evolution along a virulence–transmission tradeoff, temperature-
23 dependent forcing, and recovery returning individuals to the susceptible pool (re-
24 flecting the absence of adaptive immunity in echinoderms). Reproduction imple-
25 ments sweepstakes reproductive success with $N_e/N \sim 10^{-3}$, sex-asymmetric spawn-
26 ing induction, and post-spawning immunosuppression. Four rounds of global sen-
27 sitivity analysis (Morris screening and Sobol variance decomposition) across up to
28 47 parameters reveal that model behavior is dominated by nonlinear interactions

29 among disease mortality rate, host susceptibility, environmental pathogen pressure,
30 and genetic architecture, with resistance replacing recovery as the dominant adap-
31 tive response when reinfection is permitted. The model provides a framework for
32 evaluating captive-bred release strategies, assisted gene flow, and the feasibility of
33 evolutionary rescue on conservation-relevant timescales.

34 Contents

35	1 Introduction	7
36	1.1 Sea Star Wasting Disease and the Collapse of <i>Pycnopodia helianthoides</i>	7
37	1.2 Etiology: A Decade-Long Mystery Resolved	7
38	1.3 Conservation Urgency and Active Recovery Efforts	8
39	1.4 The Need for an Eco-Evolutionary Framework	9
40	1.5 Model Overview	10
41	1.6 Paper Outline	11
42	2 Model Architecture	11
43	2.1 Agent Representation	11
44	2.2 Node Structure	13
45	2.3 Simulation Loop	13
46	2.4 Design Rationale	14
47	3 Disease Module	15
48	3.1 Compartmental Structure	15
49	3.1.1 Erlang-Distributed Stage Durations	16
50	3.2 Force of Infection	17
51	3.2.1 Dose–Response Function	17
52	3.2.2 Salinity Modifier	17
53	3.2.3 Size-Dependent Susceptibility	18
54	3.2.4 Post-Spawning Immunosuppression	18
55	3.3 Disease Progression and Recovery	18
56	3.3.1 Transition Rates	18
57	3.3.2 Temperature Scaling (Arrhenius)	19
58	3.3.3 Tolerance: Extending I_2 Duration	19
59	3.3.4 Recovery	19
60	3.4 Vibrio Dynamics	20
61	3.4.1 Shedding	20
62	3.4.2 Carcass Shedding	20
63	3.4.3 Vibrio Decay	21
64	3.4.4 Environmental Reservoir	21
65	3.5 Pathogen Evolution	21
66	3.5.1 Virulence–Tradeoff Curves	22
67	3.5.2 Transmission and Mutation	22
68	3.6 Basic Reproduction Number	22
69	3.7 Daily Update Sequence	23

70	4 Genetics Module	23
71	4.1 Three-Trait Architecture	23
72	4.2 Trait Score Computation	25
73	4.2.1 Effect Size Distribution	25
74	4.2.2 Coupling to Disease Dynamics	25
75	4.3 Genotype Initialization	26
76	4.4 Mendelian Inheritance and Mutation	26
77	4.5 Sweepstakes Reproductive Success	27
78	4.6 Genetic Diagnostics and Tracking	28
79	4.7 Genotype Bank (Tier 2 Nodes)	28
80	5 Population Dynamics	29
81	5.1 Life Stages	29
82	5.2 Growth	29
83	5.3 Natural Mortality	30
84	5.4 Spawning System	30
85	5.4.1 Spawning Season and Phenology	31
86	5.4.2 Spontaneous Spawning	31
87	5.4.3 Cascade Induction	31
88	5.4.4 Post-Spawning Immunosuppression	32
89	5.5 Fecundity	32
90	5.6 Fertilization Kinetics and the Allee Effect	33
91	5.7 Larval Phase	33
92	5.8 Settlement and Recruitment	33
93	5.9 Continuous Settlement	34
94	5.10 Demographic–Genetic–Epidemiological Coupling	35
95	6 Spatial Module and Environmental Forcing	35
96	6.1 Metapopulation Network Structure	36
97	6.1.1 Node Definition	36
98	6.1.2 Internode Distance Computation	36
99	6.2 Connectivity Matrices	37
100	6.2.1 Larval Connectivity Matrix C	37
101	6.2.2 Pathogen Dispersal Matrix D	38
102	6.2.3 Dispersal Dynamics	38
103	6.3 Environmental Forcing	39
104	6.3.1 Sea Surface Temperature	39
105	6.3.2 Temperature-Dependent Rate Scaling	40
106	6.3.3 Salinity Modifier	40

107	6.3.4 Flushing Rate	40
108	6.4 Agent Movement	41
109	6.5 Network Configurations	42
110	6.5.1 5-Node Validation Network	42
111	6.5.2 11-Node Sensitivity Analysis Network	42
112	6.5.3 Full-Range Network (Planned)	43
113	6.6 Network Construction	43
114	7 Sensitivity Analysis	44
115	7.1 Methods	44
116	7.1.1 Morris Elementary Effects Screening	44
117	7.1.2 Sobol Variance Decomposition	44
118	7.1.3 Output Metrics	45
119	7.2 Progressive Sensitivity Analysis Design	45
120	7.3 Round 4 Morris Results	47
121	7.3.1 Global Parameter Ranking	47
122	7.3.2 Key Rank Shifts from Round 3	48
123	7.3.3 New Three-Trait Parameters	51
124	7.3.4 Universal Nonlinearity	51
125	7.3.5 Module-Level Sensitivity	52
126	7.4 Cross-Round Parameter Trajectories	53
127	7.5 Sobol Variance Decomposition: Rounds 1–2 and Ongoing	54
128	7.5.1 R1–R2 Sobol Results	54
129	7.5.2 Round 4 Sobol (In Progress)	55
130	7.6 Summary and Implications	55
131	8 Validation	60
132	8.1 K = 5,000 Validation	60
133	8.2 K = 100,000 Scale-Up Validation	63
134	8.3 Cross-Scale Comparison	64
135	8.4 Reinfection Dynamics: R→S Validation	65
136	8.5 Key Scientific Findings	67
137	8.5.1 Evolutionary Rescue Is Insufficient	67
138	8.5.2 Recovery as the Primary Adaptive Pathway	67
139	8.5.3 The Extinction Vortex Persists at Realistic Scales	68
140	8.5.4 Implications for Captive Breeding	68
141	9 Discussion	69
142	9.1 Summary of Contributions	69
143	9.2 Comparison with Clement et al. (2024)	70

144	9.3	The Environmental Pathogen Reservoir as a Multi-Species Abstraction	71
145	9.4	Conservation Implications	72
146	9.4.1	Evolutionary Rescue Is Too Slow	72
147	9.4.2	Breeding Target: Resistance over Recovery	73
148	9.4.3	Release Site Selection	73
149	9.5	Model Limitations	73
150	9.6	Future Directions	74
151	9.6.1	ABC-SMC Calibration	74
152	9.6.2	Conservation Scenario Evaluation	75
153	9.6.3	Full Coastline Network	75
154	9.6.4	Integration with Empirical Data	75
155	9.7	Conclusions	76
156	A Parameter Tables		83

157 **1 Introduction**

158 **1.1 Sea Star Wasting Disease and the Collapse of *Pycnopodia***
159 ***helianthoides***

160 Sea star wasting disease (SSWD) caused one of the largest documented wildlife mass
161 mortality events in marine ecosystems when it swept through populations of over 20
162 asteroid species along the northeastern Pacific coast beginning in 2013 [24, 31, 50]. The
163 disease, characterized by behavioral changes (arm twisting, lethargy), loss of turgor,
164 body wall lesions, ray autotomy, and rapid tissue degradation, devastated populations
165 from Baja California to the Gulf of Alaska within months [34, 49]. Among the species
166 affected, the sunflower sea star (*Pycnopodia helianthoides*) suffered the most catastrophic
167 decline, losing an estimated 5.75 billion individuals and experiencing a 90.6% range-wide
168 population reduction based on 61,043 surveys across 31 datasets [20, 26]. Along the outer
169 coast from Washington to Baja California, declines exceeded 97%, with many regions
170 recording zero individuals in subsequent surveys [20, 23]. The species was assessed as
171 Critically Endangered by the IUCN in 2021 [20] and is under consideration for listing as
172 Threatened under the U.S. Endangered Species Act [42].

173 As a large-bodied, mobile, generalist predator capable of consuming sea urchins at
174 rates sufficient to structure entire subtidal communities, *Pycnopodia helianthoides* func-
175 tions as a keystone species in northeastern Pacific kelp forest ecosystems [6, 15, 47].
176 Its precipitous decline has been linked to cascading trophic effects, including sea urchin
177 population explosions and extensive kelp forest deforestation, with northern California
178 losing 96% of its kelp canopy since the 2014 marine heatwave [48, 56]. The loss of this
179 apex predator thus represents not only a conservation crisis for a single species but a
180 destabilization of an entire marine ecosystem [23, 39].

181 **1.2 Etiology: A Decade-Long Mystery Resolved**

182 For over a decade following the initial outbreak, the causative agent of SSWD remained
183 contested. An early hypothesis implicating sea star associated densovirus (SSaDV; Hew-
184 son et al. 31) was subsequently retracted after repeated failures to reproduce the original
185 challenge experiments and the discovery that the virus is endemic in healthy echinoderm
186 populations worldwide [32–34]. An alternative hypothesis invoking boundary layer oxygen
187 depletion (BLODL) at the animal–water interface proposed that microbial respiration on
188 sea star surfaces draws down dissolved oxygen, leading to tissue hypoxia [2, 29]. While
189 this mechanism may contribute to disease susceptibility, it did not identify a specific
190 pathogen.

191 The breakthrough came with Prentice et al. [54], who fulfilled Koch’s postulates by
192 demonstrating that *Vibrio pectenicida* strain FHCF-3, a Gram-negative marine bac-

terium, is a causative agent of SSWD in *Pycnopodia helianthoides*. Through seven controlled exposure experiments using captive-bred, quarantined sea stars, the authors showed that injection of cultured *V. pectenicida* FHCF-3 into the coelomic cavity reliably produced disease signs — arm twisting, lesion formation, autotomy, and death within approximately two weeks. Heat-treated and 0.22 µm filtered controls remained healthy, confirming a living bacterial agent. Critically, the pathogen was re-isolated from experimentally infected animals, completing Koch’s postulates. Earlier investigations had missed *V. pectenicida* because they sampled body wall tissue rather than coelomic fluid, where the bacterium resides.

However, the etiological picture is not entirely resolved. Hewson [30] demonstrated that *V. pectenicida* FHCF-3 was not consistently detected in non-*Pycnopodia helianthoides* species during the 2013–2014 mass mortality, suggesting it may be specific to *Pycnopodia helianthoides* or may function as an opportunistic pathogen rather than a universal SSWD agent across all affected asteroid taxa. The bacterium also exhibits explosive growth in the presence of decaying echinoderm tissue, raising questions about whether it acts primarily as a pathogen or a saprobe under different conditions [30]. Nonetheless, for *Pycnopodia helianthoides* — the focus of this study — the evidence for *V. pectenicida* as the primary causative agent is robust. The identification of a specific bacterial pathogen with known temperature-dependent growth dynamics [45] provides a mechanistic basis for modeling disease transmission and environmental forcing.

1.3 Conservation Urgency and Active Recovery Efforts

The failure of *Pycnopodia helianthoides* populations to recover naturally in the decade following the initial epizootic — contrasting with partial recovery observed in some co-occurring asteroid species [19] — has motivated intensive conservation action. The species’ long generation time (~30 years), broadcast spawning reproductive strategy, and vulnerability to Allee effects at low density [16, 43] compound the challenge of natural recovery. Historical precedent is sobering: the Caribbean long-spined sea urchin *Diadema antillarum*, which suffered a comparable 93–100% mass mortality in 1983–1984, achieved only ~12% recovery after three decades [40]. Another asteroid, *Heliaster kubiniji*, has never recovered from a 1975 mass mortality event in the Gulf of California [12].

In response, a coordinated multi-partner recovery effort has emerged. The Association of Zoos and Aquariums (AZA) Saving Animals From Extinction (SAFE) program maintains over 2,500 captive juveniles and 130+ reproductive adults across 17 AZA institutions [5]. Experimental outplanting of captive-bred *Pycnopodia helianthoides* has progressed through three phases: caged trials off San Juan Island, Washington in 2023 established initial feasibility; the first uncaged release of 20 captive-bred juveniles (ages 1–3 yr) off the Friday Harbor Laboratories dock in July–August 2024 represented the first-ever re-

lease of captive-bred *Pycnopodia helianthoides* into the wild [57]; and the first California outplanting in Monterey Bay in December 2025, where 47 of 48 juveniles survived after four weeks [66]. A Roadmap to Recovery developed by over 30 leading experts defines regionally nested recovery objectives, from local demographic benchmarks to range-wide genetic structure targets [26]. Cryopreservation of gametes has been demonstrated for a congener and is under development for *Pycnopodia helianthoides* to enable assisted gene flow from genetically diverse founders [22, 63]. In 2025, the California Ocean Protection Council approved \$630,000 in funding for captive breeding, disease diagnostics, and experimental outplanting [7]. A reference genome has also been published [62], laying the groundwork for genome-wide association studies (GWAS) to identify resistance loci.

These recovery efforts require quantitative predictions: How many captive-bred individuals should be released, where, and when? What are the genetic consequences of releasing animals from a limited captive founder population? Can natural selection drive resistance evolution fast enough to matter on conservation timescales? How do pathogen evolution, environmental change, and spatial structure interact to shape recovery trajectories? Answering these questions demands a modeling framework that integrates disease dynamics with population genetics in an explicitly spatial context.

1.4 The Need for an Eco-Evolutionary Framework

Existing models of SSWD dynamics have focused on either epidemiological or ecological aspects in isolation. Aalto et al. [1] coupled an SIR-type model with ocean circulation to explain the rapid continental-scale spread of SSWD, finding that temperature-dependent mortality best matched observed patterns. Tolimieri [68] conducted a population viability analysis using stage-structured matrix models but did not incorporate disease dynamics or host genetics. Arroyo-Esquivel et al. [4] recently modeled epidemiological consequences of managed reintroduction following disease-driven host decline, but their framework lacks genetic evolution. None of these approaches captures the interplay between disease-driven selection, host genetic adaptation, and demographic recovery that is central to predicting conservation outcomes.

The theoretical motivation for coupling these processes is compelling. Mass mortality events impose intense directional selection on host populations [60], and in *Pisaster ochraceus* — a co-occurring sea star affected by SSWD — rapid allele frequency shifts ($\Delta q \approx 0.08\text{--}0.15$ at outlier loci) were detected within a single generation of the epizootic, with geographic consistency across sites indicating selection rather than drift [60]. However, in broadcast-spawning marine invertebrates, the genetic consequences of mass mortality are filtered through sweepstakes reproductive success (SRS), whereby variance in individual reproductive success is so large that effective population size (N_e) is orders of magnitude smaller than census size ($N_e/N \sim 10^{-3}$; Árnason et al. 3, Hedgecock and

267 Pudovkin 27). SRS amplifies genetic drift on ecological timescales [69], can facilitate rapid
268 adaptation when coupled with bottlenecks [14], and generates chaotic genetic patchiness
269 that confounds simple predictions of evolutionary trajectories. Any model of evolutionary
270 rescue in *Pycnopodia helianthoides* must therefore account for this fundamental feature
271 of marine broadcast spawner genetics.

272 The closest methodological precedent is the eco-evolutionary individual-based model
273 (IBM) developed by Clement et al. [10] for coevolution between Tasmanian devils (*Sar-*
274 *cophilus harrisii*) and devil facial tumour disease (DFTD). That model coupled an SEI
275 epidemiological framework with polygenic quantitative genetics, parameterized from two
276 decades of field data and GWAS results, and found a high probability of host persistence
277 over 50 generations through coevolutionary dynamics. Our model extends this approach
278 to a marine system with fundamentally different reproductive biology — broadcast spawn-
279 ing with sweepstakes reproductive success, external fertilization subject to Allee effects,
280 and a pelagic larval phase mediating spatial connectivity — challenges that no existing
281 eco-evolutionary disease model has addressed.

282 1.5 Model Overview

283 We present SSWD-EvoEpi, an individual-based, spatially explicit, eco-evolutionary epi-
284 demiological model designed to simulate SSWD dynamics and evolutionary responses in
285 *Pycnopodia helianthoides* metapopulations across the northeastern Pacific. The model
286 tracks individual sea stars as agents within a network of habitat nodes connected by larval
287 dispersal and pathogen transport. Each agent carries a diploid genotype across 51 loci
288 governing three fitness-related traits: resistance (r_i , 17 loci; immune exclusion reducing
289 infection probability), tolerance (t_i , 17 loci; damage limitation extending survival dur-
290 ing late-stage infection), and recovery (c_i , 17 loci; pathogen clearance enabling transition
291 from infected to recovered states). Per-locus allele frequencies are drawn from a Beta(2,8)
292 distribution, reflecting polygenic architecture with most loci at low frequency [36].

293 Disease dynamics follow an SEIR-type compartmental structure with exposed (E),
294 early infected (I_1), and late infected (I_2) stages, coupled with an environmental pathogen
295 reservoir (P) whose dynamics are temperature-dependent [18, 45]. Pathogen evolution
296 is modeled through a heritable virulence phenotype that evolves along a mechanistic
297 tradeoff curve linking shedding rate to host survival duration. Reproduction incorpo-
298 rates sweepstakes reproductive success via a heavy-tailed offspring distribution producing
299 N_e/N ratios consistent with empirical estimates for marine broadcast spawners [27], with
300 sex-asymmetric spawning induction and post-spawning immunosuppression derived from
301 species-specific observations. Spatial connectivity is implemented through distinct larval
302 exchange and pathogen dispersal matrices computed from overwater distances across the
303 model domain.

304 The model is implemented in Python with NumPy-vectorized agent operations, achieving
305 sufficient performance for large-scale sensitivity analysis and calibration (75,000 agents
306 across 150 nodes in \sim 72 s). Four rounds of sensitivity analysis using Morris screening and
307 Sobol variance decomposition across up to 47 parameters have identified the key drivers of
308 model behavior, revealing strong nonlinear interactions and highlighting priority targets
309 for empirical calibration.

310 1.6 Paper Outline

311 The remainder of this paper is organized as follows. Section 2 describes the overall model
312 architecture, agent representation, and simulation flow. Sections 3–6 detail the disease,
313 genetics, population dynamics, and spatial modules, respectively. Section 7 presents four
314 rounds of global sensitivity analysis, identifying the parameters with greatest influence
315 on epidemiological, demographic, and evolutionary outcomes. Section 8 describes model
316 validation against available empirical data. Section 9 synthesizes findings, discusses lim-
317 itations, and outlines the path toward calibrated conservation scenario evaluation. Pa-
318 rameter tables and supplementary analyses are provided in Appendix A.

319 2 Model Architecture

320 SSWD-EvoEpi is an individual-based model (IBM) that couples epidemiological, demo-
321 graphic, genetic, and spatial dynamics to simulate the eco-evolutionary consequences of
322 sea star wasting disease in *Pycnopodia helianthoides*. Each agent represents a single sea
323 star tracked through its complete life history, carrying a diploid genotype at 51 loci that
324 determines three quantitative defense traits against *Vibrio pectenicida*. We chose an
325 individual-based approach over compartmental (ODE/PDE) models because SSWD dy-
326 namics depend critically on individual-level heterogeneity in genetic resistance, body size,
327 spatial position, and disease stage—features that compartmental models cannot represent
328 without substantial loss of biological realism [11, 21].

329 2.1 Agent Representation

330 Each individual is represented as a record in a NumPy structured array (**AGENT_DTYPE**)
331 comprising approximately 59 bytes per agent. Table 1 summarizes the principal state
332 variables grouped by functional module.

Table 1: Agent state variables in SSWD-EvoEpi.

Module	Field	Description
Spatial	x, y	Position within node habitat (m)
	heading	Movement heading (rad)
	speed	Instantaneous speed (m min^{-1})
	node_id	Home node index
Life history	size	Arm-tip diameter (mm)
	age	Age (years, fractional)
	stage	Life stage (0–4; Table 2)
	sex	Sex (0 = female, 1 = male)
Disease	disease_state	Compartment (S/E/I ₁ /I ₂ /D/R)
	disease_timer	Days remaining in current disease stage
Genetics	resistance	Resistance score $r_i \in [0, 1]$
	tolerance	Tolerance score $t_i \in [0, 1]$
	recovery_ability	Recovery/clearance score $c_i \in [0, 1]$
Spawning	has_spawned	Bout count this season
	immunosuppression_timer	Post-spawning immunosuppression (days)
Administrative	alive	Active flag
	origin	Wild / captive-bred / AGF / wild-source
	pathogen_virulence	Virulence of infecting strain v_i

333 Genotypes are stored in a separate array of shape $(N_{\text{max}}, 51, 2)$ with `int8` entries,
 334 where axis 1 indexes loci and axis 2 indexes the two allele copies (diploid). This separation
 335 from the agent record improves cache performance during non-genetic operations (disease
 336 transmission, movement), which need not touch the genotype array.

 Table 2: Life stages and size thresholds for *Pycnopodia helianthoides*.

Index	Stage	Size threshold (mm)	Reproductive
0	Egg/Larva	—	No
1	Settler	Settlement	No
2	Juvenile	≥ 10	No
3	Subadult	≥ 150	No
4	Adult	≥ 400	Yes

337 **2.2 Node Structure**

338 The spatial domain is represented as a metapopulation network of K discrete habitat
339 nodes. Each node encapsulates:

- 340 • A population of agents (structured array + genotype array), initialized at local
341 carrying capacity;
- 342 • Environmental state: sea surface temperature $T(t)$ (sinusoidal annual cycle with
343 warming trend), salinity S , and tidal flushing rate ϕ_k ;
- 344 • A local Vibrio concentration $P_k(t)$ (bacteria mL⁻¹);
- 345 • Node metadata: latitude, habitat area, fjord classification.

346 Inter-node coupling occurs through two connectivity matrices:

- 347 1. **Pathogen dispersal matrix D:** governs daily exchange of waterborne *Vibrio*
348 *pectenicida* between nodes, parameterized with an exponential distance kernel (scale
349 $D_P = 15$ km);
- 350 2. **Larval connectivity matrix C:** governs annual dispersal of competent larvae
351 among nodes, parameterized with a broader kernel (scale $D_L = 400$ km) reflecting
352 the extended pelagic larval duration of *Pycnopodia helianthoides*.

353 **2.3 Simulation Loop**

354 The simulation advances in daily timesteps ($\Delta t = 1$ day) nested within an annual cycle.
355 At each daily step, the following operations are executed in sequence at every node
356 (Figure ??):

- 357 1. **Environment update.** Compute $T_k(t)$ from a sinusoidal annual SST function
358 with linear warming trend; update flushing rate ϕ_k (seasonally modulated for fjord
359 nodes); salinity is constant per node.
- 360 2. **Movement.** Agents execute a correlated random walk (CRW) with 24 hourly
361 substeps per day. Movement speed is modulated by disease state ($\times 0.5$ for I₁, $\times 0.1$
362 for I₂, $\times 0$ for D). Elastic boundary reflection constrains agents within the habitat.
- 363 3. **Disease dynamics.** Vibrio concentration is updated via an Euler step of the
364 pathogen ODE. Susceptible agents are exposed to a force of infection that depends
365 on local pathogen density, individual resistance, salinity, and body size. Infected
366 agents progress through the SEIPD compartments with Erlang-distributed stage
367 durations (Section 3).

- 368 4. **Pathogen dispersal.** Vibrio is exchanged between neighboring nodes via the **D**
 369 matrix, representing waterborne transport.
- 370 5. **Settlement.** Larval cohorts whose pelagic larval duration (PLD) has elapsed are
 371 settled into the local population via Beverton–Holt density-dependent recruitment,
 372 modulated by an adult-presence settlement cue (Allee effect).
- 373 6. **Spawning.** During the spawning season (November–July), reproductively mature
 374 adults spawn stochastically with daily probability modulated by a seasonal Gaus-
 375 sian envelope centered on the peak spawning day. Female and male multi-bout
 376 spawning, sex-asymmetric cascade induction, and post-spawning immunosuppres-
 377 sion are modeled explicitly.
- 378 7. **Daily demographics.** Natural mortality is applied as a daily probability con-
 379 verted from stage-specific annual survival rates:

$$p_{\text{death,daily}} = 1 - S_{\text{annual}}^{1/365}, \quad (1)$$

380 with a senescence overlay for individuals exceeding the senescence age ($\tau_{\text{sen}} = 50 \text{ yr}$).
 381 Growth follows the von Bertalanffy differential form with daily-scaled stochastic
 382 noise; stage transitions are one-directional based on size thresholds (Table 2).

383 At the end of each simulated year, an annual step performs:

- 384 1. **Larval dispersal** via the connectivity matrix **C**: unsettled cohorts from all nodes
 385 are pooled, redistributed probabilistically among destination nodes, and settled at
 386 receiving nodes or retained in a pending queue for next-year daily settlement.
- 387 2. **Disease introduction** (at the designated epidemic year): a fixed number of agents
 388 per node are seeded in the Exposed (E) compartment.
- 389 3. **Genetic recording**: per-node allele frequencies, additive genetic variance V_A , and
 390 trait means are logged annually. Pre- and post-epidemic allele frequency snapshots
 391 are captured for calibration against genomic data.

392 2.4 Design Rationale

393 Several design choices distinguish SSWD-EvoEpi from previous SSWD models:

394 **Individual-based representation.** SSWD mortality is strongly size-dependent [OR
 395 = 1.23 per 10 mm; 13], genetically mediated [61], and spatially heterogeneous. A compart-
 396 mental SIR/SEIR model would require aggregating these axes of variation into homoge-
 397 neous classes, losing the emergent eco-evolutionary dynamics that arise from individual

398 heterogeneity in resistance, tolerance, and recovery. Following Clement et al. [9], who
399 demonstrated that individual-based eco-evolutionary models are essential for predicting
400 host-pathogen coevolution in Tasmanian devil facial tumor disease, we track each indi-
401 vidual’s genotype, phenotype, and infection history explicitly.

402 **Continuous daily demographics.** Rather than applying mortality, growth, and re-
403 production as annual pulses, SSWD-EvoEpi evaluates natural mortality and growth daily
404 (Eq. 1), with spawning resolved to individual daily events across a multi-month season.
405 This avoids artificial synchronization artifacts and allows disease-demography interac-
406 tions (e.g., post-spawning immunosuppression) to operate on their natural timescales.

407 **Separated genotype storage.** The 51-locus diploid genotype array (102 bytes per
408 agent) is stored separately from the agent state record. This ensures that the most
409 frequently accessed fields during daily disease and movement updates (position, disease
410 state, size) occupy contiguous memory, improving CPU cache performance by a factor of
411 $\sim 2\text{--}3\times$ in profiled benchmarks.

412 **Three-trait genetic architecture.** The 51 loci are partitioned into three indepen-
413 dently segregating trait blocks of 17 loci each, controlling resistance (immune exclusion),
414 tolerance (damage limitation), and recovery (pathogen clearance). This architecture
415 captures the empirical observation that host defense against infectious disease operates
416 through mechanistically distinct pathways that can evolve semi-independently [55].

417 3 Disease Module

418 The disease module implements a stochastic, environmentally driven SEIPD compart-
419 mental framework (Susceptible–Exposed–Infectious₁–Infectious₂–Dead, with recovery re-
420 turning individuals to the susceptible pool) operating at the individual level. Each agent
421 carries its own disease state, countdown timer, genetic defense traits (r_i , t_i , c_i), and
422 (when pathogen evolution is enabled) the virulence phenotype v_i of its infecting strain.
423 Disease dynamics are resolved daily at each spatial node, coupled to the environmental
424 forcing module for temperature-dependent rates and to the genetics module for individual
425 susceptibility.

426 3.1 Compartmental Structure

427 The disease pathway consists of five compartments with a recovery transition back to the
428 susceptible state (Figure ??):

- 429 • **S (Susceptible):** Healthy, at risk of infection.

- **E (Exposed):** Latently infected; not yet shedding pathogen. Duration is Erlang-distributed with shape $k_E = 3$.
- **I₁ (Early infectious):** Pre-symptomatic shedding at rate $\sigma_1(T)$. Duration is Erlang-distributed with shape $k_{I_1} = 2$. Agents with high clearance ability ($c_i > 0.5$) may recover early.
- **I₂ (Late infectious):** Symptomatic wasting with high shedding rate $\sigma_2(T)$. Duration is Erlang-distributed with shape $k_{I_2} = 2$. Agents may recover with probability $p_{\text{rec}} = \rho_{\text{rec}} \times c_i$ per day.
- **D (Dead from disease):** Carcass continues to shed pathogen saprophytically for a 3-day window at rate σ_D .
- **Recovery ($\rightarrow S$):** Recovered individuals return to the susceptible pool and may be reinfected. Echinoderms lack adaptive immunity and show no evidence of acquired resistance to SSWD; stars treated for wasting via iodine dip and probiotic protocols have subsequently developed wasting again, confirming absence of immunological memory [70]. Heritable genetic traits (resistance, tolerance, recovery) represent the only defense mechanism.

3.1.1 Erlang-Distributed Stage Durations

Durations in compartments E, I₁, and I₂ are drawn from Erlang distributions rather than geometric (exponential) distributions. The Erlang distribution with shape parameter k and rate parameter $k\mu$ has mean $1/\mu$ and coefficient of variation $CV = 1/\sqrt{k}$, producing more realistic, peaked duration distributions compared to the memoryless exponential [72]. For each individual entering a compartment, a duration is sampled as:

$$\tau \sim \text{Erlang}(k, k\mu(T)), \quad \text{rounded to } \max(1, \text{round}(\tau)) \text{ days}, \quad (2)$$

where $\mu(T)$ is the temperature-dependent transition rate at the current SST (Section 3.3.2). The shape parameters are:

$$k_E = 3 \quad (CV = 0.58), \quad k_{I_1} = 2 \quad (CV = 0.71), \quad k_{I_2} = 2 \quad (CV = 0.71). \quad (3)$$

Timers count down by one each day; when the timer reaches zero, the agent transitions to the next compartment.

456 3.2 Force of Infection

457 The per-individual instantaneous hazard rate of infection is:

$$\lambda_i = a_{\text{exp}} \underbrace{\frac{P_k}{K_{1/2} + P_k}}_{\text{dose-response}} \underbrace{(1 - r_i)}_{\text{resistance}} \underbrace{S_{\text{sal}}}_{\text{salinity}} \underbrace{f_{\text{size}}(L_i)}_{\text{size}}, \quad (4)$$

458 where:

- 459 • $a_{\text{exp}} = 0.75 \text{ d}^{-1}$ is the baseline exposure rate;
- 460 • P_k is the local Vibrio concentration (bacteria mL^{-1}) at node k ;
- 461 • $K_{1/2} = 87,000 \text{ bacteria mL}^{-1}$ is the half-infective dose (Michaelis–Menten dose–
462 response);
- 463 • $r_i \in [0, 1]$ is the individual's resistance score (immune exclusion; Section 4);
- 464 • S_{sal} is the salinity modifier (Section 3.2.2);
- 465 • $f_{\text{size}}(L_i)$ is the size-dependent susceptibility modifier (Section 3.2.3).

466 The discrete daily probability of infection is:

$$p_{\text{inf}} = 1 - \exp(-\lambda_i \Delta t), \quad \Delta t = 1 \text{ day.} \quad (5)$$

467 3.2.1 Dose–Response Function

468 Pathogen exposure follows a Michaelis–Menten (saturating) dose–response:

$$D(P_k) = \frac{P_k}{K_{1/2} + P_k}. \quad (6)$$

469 At low concentrations ($P_k \ll K_{1/2}$), infection probability scales linearly with pathogen
470 density; at high concentrations ($P_k \gg K_{1/2}$), it saturates at $D \rightarrow 1$, reflecting physiolog-
471 ical limits on pathogen uptake.

472 3.2.2 Salinity Modifier

473 Vibrio viability is suppressed at low salinities, providing a mechanistic basis for the
474 reduced SSWD prevalence observed in fjord systems:

$$S_{\text{sal}} = \begin{cases} 0 & \text{if } S \leq S_{\text{min}} = 10 \text{ psu,} \\ \left(\frac{S - S_{\text{min}}}{S_{\text{full}} - S_{\text{min}}} \right)^{\eta} & \text{if } S_{\text{min}} < S < S_{\text{full}}, \\ 1 & \text{if } S \geq S_{\text{full}} = 28 \text{ psu,} \end{cases} \quad (7)$$

475 where $\eta = 2$ produces a convex response (low salinity is strongly protective).

476 3.2.3 Size-Dependent Susceptibility

477 Larger *Pycnopodia helianthoides* are more susceptible to SSWD, consistent with the em-
478 pirical finding of Eisenlord et al. [13] (odds ratio 1.23 per 10 mm increase in radius). The
479 size modifier is:

$$f_{\text{size}}(L_i) = \exp\left(\beta_L \frac{L_i - \bar{L}}{\sigma_L}\right), \quad (8)$$

480 where $\beta_L = 0.021 \text{ mm}^{-1}$ ($= \ln 1.23/10$), $\bar{L} = 300 \text{ mm}$ is the reference size, and $\sigma_L =$
481 100 mm normalizes the deviation. An individual of diameter $L_i = 500 \text{ mm}$ has $\sim 1.5 \times$ the
482 infection hazard of a 300 mm individual.

483 3.2.4 Post-Spawning Immunosuppression

484 Spawning imposes a transient immune cost. Following each spawning event, an individ-
485 ual enters a 28-day immunosuppression window during which its effective resistance is
486 reduced:

$$r_{i,\text{eff}} = \frac{r_i}{\psi_{\text{spawn}}}, \quad \psi_{\text{spawn}} = 2.0, \quad (9)$$

487 clamped to $[0, 1]$. This halves effective resistance during the immunosuppressed period,
488 creating an evolutionary coupling between reproductive investment and disease vulnera-
489 bility.

490 3.3 Disease Progression and Recovery

491 Disease progression rates are temperature-dependent via an Arrhenius function (Sec-
492 tion 3.3.2). At each daily step, disease timers are decremented; when a timer reaches
493 zero, the agent transitions to the next state. Recovery can occur before timer expiry.

494 3.3.1 Transition Rates

495 The base progression rates at reference temperature $T_{\text{ref}} = 20^\circ\text{C}$ are:

$$\mu_{E \rightarrow I_1} = 0.57 \text{ d}^{-1} \quad (E_a/R = 4,000 \text{ K}), \quad (10)$$

$$\mu_{I_1 \rightarrow I_2} = 0.40 \text{ d}^{-1} \quad (E_a/R = 5,000 \text{ K}), \quad (11)$$

$$\mu_{I_2 \rightarrow D} = 0.173 \text{ d}^{-1} \quad (E_a/R = 2,000 \text{ K}). \quad (12)$$

496 The activation energy for $I_2 \rightarrow D$ is notably lower ($E_a/R = 2,000 \text{ K}$ vs. $5,000\text{--}6,000 \text{ K}$ for
497 other transitions), reflecting evidence that terminal wasting is less temperature-sensitive
498 than earlier disease stages (Errata E1).

499 **3.3.2 Temperature Scaling (Arrhenius)**

500 All temperature-dependent rates are scaled via the Arrhenius equation:

$$k(T) = k_{\text{ref}} \exp \left[\frac{E_a}{R} \left(\frac{1}{T_{\text{ref}}} - \frac{1}{T} \right) \right], \quad (13)$$

501 where $T_{\text{ref}} = 293.15 \text{ K}$ (20°C) is the reference temperature corresponding to the *Vibrio*
502 *pectenicia* thermal optimum [38], and E_a/R is the activation energy divided by the
503 gas constant. The Arrhenius formulation ensures that colder temperatures slow disease
504 progression (longer E, I₁, I₂ durations) and reduce shedding rates, consistent with the
505 observed latitudinal gradient in SSWD severity.

506 **3.3.3 Tolerance: Extending I₂ Duration**

507 The tolerance trait t_i operates as a damage-limitation mechanism that reduces the effec-
508 tive I₂ → D mortality rate, extending survival time while infected:

$$\mu_{I_2 \rightarrow D, \text{eff}} = \mu_{I_2 \rightarrow D}(T) \times (1 - t_i \tau_{\max}), \quad \text{floored at } 0.05 \times \mu_{I_2 \rightarrow D}(T), \quad (14)$$

509 where $\tau_{\max} = 0.85$ is the maximum mortality reduction at $t_i = 1$. The floor prevents
510 biologically implausible indefinite survival. The effective rate is used when sampling the
511 I₂ timer (Eq. 2), so tolerant individuals spend longer in I₂— which may prolong both
512 recovery opportunity and pathogen shedding.

513 **3.3.4 Recovery**

514 Recovery from infection proceeds via the clearance trait c_i , which represents the host's
515 capacity for pathogen elimination.

516 **Recovery from I₂.** Each day, an I₂ individual has probability:

$$p_{\text{rec}, I_2} = \rho_{\text{rec}} \times c_i, \quad \rho_{\text{rec}} = 0.05 \text{ d}^{-1}, \quad (15)$$

517 of clearing infection and returning to the susceptible pool (I₂ → S). At $c_i = 0$ (no
518 clearance ability), recovery is impossible; at $c_i = 1$, the daily recovery probability is 5%.
519 Recovered individuals are immediately susceptible to reinfection, reflecting the absence
520 of adaptive immunity in echinoderms.

521 **Early recovery from I₁.** Individuals with exceptionally high clearance ability ($c_i >$
522 0.5) can recover during the pre-symptomatic stage:

$$p_{\text{rec},I_1} = \begin{cases} 0 & \text{if } c_i \leq 0.5, \\ \rho_{\text{rec}} \times 2(c_i - 0.5) & \text{if } c_i > 0.5. \end{cases} \quad (16)$$

523 At $c_i = 1.0$, the early recovery probability equals ρ_{rec} , identical to I₂ recovery at maximum
524 clearance. The threshold at $c_i = 0.5$ ensures that only rare, high-clearance individuals
525 can clear infection before progressing to the symptomatic stage.

526 3.4 Vibrio Dynamics

527 The concentration of waterborne *Vibrio pectenicida* at node k evolves according to:

$$\frac{dP_k}{dt} = \underbrace{\sigma_1(T) n_{I_1} + \sigma_2(T) n_{I_2} + \sigma_D n_{D,\text{fresh}}}_{\text{shedding}} - \underbrace{\xi(T) P_k}_{\text{decay}} - \underbrace{\phi_k P_k}_{\text{flushing}} + \underbrace{P_{\text{env}}(T, S)}_{\text{reservoir}} + \underbrace{\sum_j d_{jk} P_j}_{\text{dispersal}}, \quad (17)$$

528 integrated via forward Euler with $\Delta t = 1$ day, subject to $P_k \geq 0$.

529 3.4.1 Sheding

530 Pathogen shedding from live infectious hosts is temperature-dependent:

$$\sigma_1(T) = 5.0 \times \text{Arr}(T) \quad (\text{I}_1: \text{pre-symptomatic}), \quad (18)$$

$$\sigma_2(T) = 50.0 \times \text{Arr}(T) \quad (\text{I}_2: \text{symptomatic}), \quad (19)$$

531 where $\text{Arr}(T)$ denotes the Arrhenius factor (Eq. 13) with $E_a/R = 5,000$ K. The 10-
532 fold difference between early and late shedding reflects the dramatic increase in tissue
533 degradation and pathogen release during the wasting phase. Rates are given in bacte-
534 ria $\text{mL}^{-1} \text{d}^{-1}$ host $^{-1}$ and represent field-effective values (Errata E2).

535 3.4.2 Carcass Sheding

536 Dead individuals (D compartment) continue to shed pathogen saprophytically for a 3-day
537 window at a constant rate $\sigma_D = 15 \text{ bacteria mL}^{-1} \text{d}^{-1} \text{ carcass}^{-1}$ (field-effective; Code Er-
538 rata CE-6). A ring buffer of daily disease death counts over the most recent 3 days tracks
539 the number of “fresh” carcasses contributing to shedding:

$$n_{D,\text{fresh}}(t) = \sum_{\tau=0}^2 \text{deaths}(t - \tau). \quad (20)$$

540 **3.4.3 Vibrio Decay**

541 *Vibrio pectenicida* survives longer in warmer water. The natural decay rate $\xi(T)$ is
 542 interpolated log-linearly between empirical estimates:

$$\xi(T) = \begin{cases} 1.0 \text{ d}^{-1} & T \leq 10^\circ\text{C} \text{ (half-life } \approx 0.7 \text{ d}), \\ 0.33 \text{ d}^{-1} & T \geq 20^\circ\text{C} \text{ (half-life } \approx 2.1 \text{ d}), \\ \exp[(1-f) \ln \xi_{10} + f \ln \xi_{20}] & \text{otherwise,} \end{cases} \quad (21)$$

543 where $f = (T - 10)/10$ and values are clamped outside the 10–20 °C range. This counter-
 544 intuitive pattern (faster decay at cold temperatures) reflects the environmental Vibrio
 545 literature [44].

546 **3.4.4 Environmental Reservoir**

547 In the ubiquitous scenario (default), *Vibrio pectenicida* is assumed to persist in the sed-
 548 iment as viable-but-non-culturable (VBNC) cells that resuscitate when SST exceeds a
 549 threshold. The background input rate is:

$$P_{\text{env}}(T, S) = P_{\text{env,max}} \underbrace{\frac{1}{1 + e^{-\kappa_{\text{VBNC}}(T - T_{\text{VBNC}})}}}_{\text{VBNC sigmoid}} \underbrace{g_{\text{peak}}(T)}_{\text{thermal performance}} \underbrace{S_{\text{sal}}}_{\text{salinity}}, \quad (22)$$

550 where:

- 551 • $P_{\text{env,max}} = 500 \text{ bacteria mL}^{-1} \text{ d}^{-1}$ is the maximum input rate;
- 552 • $\kappa_{\text{VBNC}} = 1.0 \text{ }^\circ\text{C}^{-1}$ controls the steepness of VBNC resuscitation;
- 553 • $T_{\text{VBNC}} = 12^\circ\text{C}$ is the midpoint temperature;
- 554 • $g_{\text{peak}}(T)$ is a thermal performance curve with Arrhenius increase below $T_{\text{opt}} = 20^\circ\text{C}$
 555 and quadratic decline above, reaching zero at $T_{\text{max}} = 30^\circ\text{C}$.

556 In the invasion scenario, $P_{\text{env}} = 0$ everywhere until the pathogen is explicitly intro-
 557 duced.

558 **3.5 Pathogen Evolution**

559 When pathogen evolution is enabled, each infectious agent carries a continuous virulence
 560 phenotype v_i that modulates disease rates via mechanistic tradeoff functions.

561 **3.5.1 Virulence–Tradeoff Curves**

562 More virulent strains kill faster, shed more, and progress more rapidly, but also remove
 563 themselves from the host population sooner:

$$\sigma_{1,v}(T) = \sigma_1(T) \times \exp(\alpha_{\text{shed}} \gamma_{\text{early}} (v - v^*)), \quad (23)$$

$$\sigma_{2,v}(T) = \sigma_2(T) \times \exp(\alpha_{\text{shed}} (v - v^*)), \quad (24)$$

$$\mu_{I_1 \rightarrow I_2,v}(T) = \mu_{I_1 \rightarrow I_2}(T) \times \exp(\alpha_{\text{prog}} (v - v^*)), \quad (25)$$

$$\mu_{I_2 \rightarrow D,v}(T) = \mu_{I_2 \rightarrow D}(T) \times \exp(\alpha_{\text{kill}} (v - v^*)), \quad (26)$$

564 where $v^* = 0.5$ is the ancestral virulence (identity point), $\alpha_{\text{shed}} = 1.5$, $\alpha_{\text{prog}} = 1.0$,
 565 $\alpha_{\text{kill}} = 2.0$, and $\gamma_{\text{early}} = 0.3$ attenuates the shedding effect in the pre-symptomatic stage.

566 **3.5.2 Transmission and Mutation**

567 When a new infection occurs, the infecting strain is inherited either from a shedding
 568 individual (weighted by shedding rate) or from the environmental reservoir (with virulence
 569 $v_{\text{env}} = 0.5$). The probability of inheriting from a shedder is proportional to the total host-
 570 derived shedding relative to total pathogen input:

$$P(\text{from shedder}) = \frac{\sum_j \sigma_j(v_j, T)}{\sum_j \sigma_j(v_j, T) + P_{\text{env}}(T, S)}. \quad (27)$$

571 The inherited virulence is then subject to mutation:

$$v_{\text{new}} = \text{clip}\left(v_{\text{parent}} + \mathcal{N}(0, \sigma_{v,\text{mut}}^2), v_{\text{min}}, v_{\text{max}}\right), \quad (28)$$

572 with $\sigma_{v,\text{mut}} = 0.02$, $v_{\text{min}} = 0$, $v_{\text{max}} = 1$.

573 **3.6 Basic Reproduction Number**

574 The basic reproduction number provides a summary measure of epidemic potential at a
 575 node:

$$R_0 = \frac{a_{\text{exp}} S_0 (1 - \bar{r}) S_{\text{sal}}}{K_{1/2} (\xi(T) + \phi_k)} \left[\frac{\sigma_1(T)}{\mu_{I_1 \rightarrow I_2}(T)} + \frac{\sigma_2(T)}{\mu_{I_2 \rightarrow D,\text{eff}}(T) + \rho_{\text{rec}} \bar{c}} + \sigma_D \tau_D \right], \quad (29)$$

576 where S_0 is the number of susceptibles, \bar{r} and \bar{c} are population-mean resistance and
 577 recovery scores, $\mu_{I_2 \rightarrow D,\text{eff}}$ incorporates population-mean tolerance (Eq. 14), $\rho_{\text{rec}} \bar{c}$ adds the
 578 recovery exit rate from I_2 , and $\tau_D = 3$ days is the carcass shedding duration. The three
 579 bracketed terms represent the pathogen contribution from each infectious compartment
 580 (I_1 , I_2 , and D carcasses, respectively).

581 **3.7 Daily Update Sequence**

582 Within each daily timestep, the disease module executes the following steps in order:

- 583 1. **Update Vibrio concentration** via Euler integration of Eq. 17, using current
584 compartment counts and environmental conditions.
- 585 2. **Transmission ($S \rightarrow E$)**: For each susceptible agent, compute the force of infection
586 λ_i (Eq. 4), convert to daily probability (Eq. 5), and draw a Bernoulli infection event.
587 Newly exposed agents receive an Erlang-sampled E-stage timer. When pathogen
588 evolution is active, the infecting strain is inherited and mutated (Section 3.5.2).
- 589 3. **Disease progression**: Decrement all disease timers. For agents with expired
590 timers: $E \rightarrow I_1$, $I_1 \rightarrow I_2$ (with tolerance-adjusted timer), $I_2 \rightarrow D$. For agents with
591 active timers: check recovery from I_2 (Eq. 15) and early recovery from I_1 (Eq. 16).
- 592 4. **Carcass tracking**: Record today's disease deaths in the 3-day ring buffer for
593 saprophytic shedding.
- 594 5. **Update diagnostics**: Recount compartments, update cumulative statistics (total
595 infections, deaths, recoveries), track peak prevalence and peak Vibrio.

596 All operations are vectorized using NumPy batch sampling and array-level random
597 draws for computational efficiency, achieving $O(N)$ scaling in population size.

598 **4 Genetics Module**

599 The genetics module tracks a diploid genotype at 51 biallelic loci for every individual,
600 partitioned into three quantitative defense traits: *resistance*, *tolerance*, and *recovery*.
601 Genotypes are transmitted via Mendelian inheritance with free recombination, mutated
602 at a per-allele rate $\mu = 10^{-8}$ per generation [46], and subject to natural selection through
603 the coupling of trait scores to disease dynamics (Section 3). The module additionally
604 implements sweepstakes reproductive success (SRS) to capture the extreme reproductive
605 variance characteristic of broadcast-spawning marine invertebrates [27].

606 **4.1 Three-Trait Architecture**

607 Each individual carries a (51×2) genotype array of `int8` alleles, where the 51 loci are
608 partitioned into three contiguous blocks:

Table 3: Three-trait genetic architecture. The partition is configurable (constraint: $n_R + n_T + n_C = 51$); the default 17/17/17 split is used in all analyses reported here.

Trait	Symbol	Loci	Indices	Mechanistic role
Resistance	r_i	$n_R = 17$	0–16	Immune exclusion: reduces probability of S → E transition
Tolerance	t_i	$n_T = 17$	17–33	Damage limitation: extends I ₂ survival via mortality rate reduction
Recovery	c_i	$n_C = 17$	34–50	Pathogen clearance: daily probability of I ₁ /I ₂ → S transition (recovery)

These three traits represent biologically distinct immune strategies with different epidemiological consequences [55]:

- **Resistance** (r_i) acts *before* infection via receptor polymorphisms, barrier defenses, and innate pathogen recognition. Resistant individuals reduce pathogen pressure on the population by preventing shedding entirely.
- **Tolerance** (t_i) acts *during* infection via tissue repair, anti-inflammatory regulation, and metabolic compensation. Tolerant hosts survive longer while infected but continue to shed pathogen—they are epidemiological “silent spreaders” that maintain transmission pressure while saving themselves.
- **Recovery** (c_i) acts *during late infection* via coelomocyte phagocytosis and immune effector mobilization. Recovering hosts actively clear the pathogen and return to the susceptible pool (S), removing a shedding host from the population. Because echinoderms lack adaptive immunity, recovered individuals may be reinfected.

The locus count of 51 is motivated by Schiebelhut et al. [60], who identified ~51 loci under selection in *Pisaster ochraceus* SSWD survivors. No genome-wide association study (GWAS) data currently distinguish resistance, tolerance, and recovery loci in *P. helianthoides*; the equal 17/17/17 partition is a simplifying assumption whose sensitivity is explored via the n_R parameter in the global sensitivity analysis (Section 7). A reference genome for *P. helianthoides* is now available [62], enabling future empirical partitioning.

Removal of EF1A overdominant locus. An earlier model version included a 52nd locus representing the EF1A elongation factor with overdominant fitness effects, based on Wares and Schiebelhut [71] who documented allele frequency shifts at this locus in *Pisaster ochraceus* following SSWD. We removed this locus because (1) the EF1A finding is specific to *Pisaster* with no evidence of overdominance in *P. helianthoides*, and (2) a single overdominant locus imposed a hard floor on heterozygosity loss that was biologically unjustified for our focal species.

635 4.2 Trait Score Computation

636 At each locus ℓ , an individual carries two alleles $g_{\ell,0}, g_{\ell,1} \in \{0, 1\}$, where 1 denotes the
 637 derived (protective) allele and 0 the ancestral allele. Each locus within a trait block has
 638 a fixed effect size $e_\ell > 0$, and an individual's trait score is the effect-weighted mean allele
 639 dosage:

$$\theta_i = \sum_{\ell \in \mathcal{L}_\theta} e_\ell \frac{g_{\ell,0} + g_{\ell,1}}{2} \quad (30)$$

640 where \mathcal{L}_θ denotes the locus set for trait $\theta \in \{r, t, c\}$ and $\theta_i \in [0, \sum e_\ell]$. Effect sizes within
 641 each trait block are normalized so $\sum_{\ell \in \mathcal{L}_\theta} e_\ell = 1$, bounding all trait scores to $[0, 1]$.

642 4.2.1 Effect Size Distribution

643 Per-locus effect sizes are drawn from an exponential distribution $e_\ell \sim \text{Exp}(\lambda = 1)$, nor-
 644 malized to sum to 1.0 within each trait, and sorted in descending order. This produces
 645 a distribution where a few loci have large effects and the remainder have small effects,
 646 consistent with empirical QTL architectures for disease resistance traits [41]. A fixed
 647 seed ensures identical effect sizes across simulation runs. Each trait block receives inde-
 648 pendently drawn effect sizes.

649 4.2.2 Coupling to Disease Dynamics

650 The three traits feed into the disease module (Section 3) as follows:

651 1. **Resistance** reduces the per-individual force of infection:

$$\lambda_i = a \cdot \frac{P}{K_{1/2} + P} \cdot (1 - r_i) \cdot S_{\text{sal}} \cdot f_L(L_i) \quad (31)$$

652 where a is the exposure rate, P the local *Vibrio pectenicida* concentration, $K_{1/2}$
 653 the half-infective dose, S_{sal} the salinity modifier, and $f_L(L_i)$ the size-dependent
 654 susceptibility factor.

655 2. **Tolerance** reduces the $I_2 \rightarrow D$ transition rate via a timer-scaling mechanism:

$$\mu_{I_2D,i}^{\text{eff}} = \mu_{I_2D}(T) \cdot (1 - t_i \cdot \tau_{\max}) \quad (32)$$

656 where $\tau_{\max} = 0.85$ is the maximum mortality reduction achievable at $t_i = 1$. A
 657 floor of 5% of the baseline rate prevents complete elimination of disease mortality.
 658 Tolerant individuals survive longer while infected but continue shedding, creating
 659 a selective conflict between individual and population-level fitness.

660 3. Recovery determines the daily clearance probability:

$$p_{\text{rec},i} = \rho_{\text{rec}} \times c_i \quad (33)$$

661 where $\rho_{\text{rec}} = 0.05 \text{ d}^{-1}$ is the base recovery rate. Recovery from I_1 requires $c_i > 0.5$
662 (early clearance); recovery from I_2 has no threshold. Successful recovery transitions
663 the agent to the susceptible pool (S), as echinoderms lack acquired immunity.

664 4.3 Genotype Initialization

665 Initial allele frequencies are drawn independently for each locus from a Beta distribution:

$$q_\ell \sim \text{Beta}(a, b) \quad (\text{default } a = 2, b = 8) \quad (34)$$

666 producing a right-skewed frequency spectrum where most protective alleles are rare
667 ($\mathbb{E}[q] = a/(a + b) = 0.2$), consistent with standing variation in immune genes main-
668 tained by mutation–selection balance. The raw frequencies are then rescaled per-trait so
669 that the expected population-mean trait score equals a configurable target:

Table 4: Default target population-mean trait scores at initialization.

Trait	Target mean	Rationale
Resistance (r_i)	0.15	Pre-epidemic standing variation
Tolerance (t_i)	0.10	Moderate damage limitation
Recovery (c_i)	0.02	Rare standing variation for clearance

670 Recovery is initialized with the lowest mean because active pathogen clearance is assumed
671 to be the rarest phenotype prior to epidemic exposure. Per-locus frequencies are clipped
672 to $[0.001, 0.5]$ to prevent fixation at initialization while ensuring the derived allele never
673 begins at majority frequency. Genotypes are then sampled assuming Hardy–Weinberg
674 equilibrium at each locus: each allele copy is independently drawn as a Bernoulli trial
675 with probability q_ℓ .

676 4.4 Mendelian Inheritance and Mutation

677 At reproduction, each offspring inherits one randomly chosen allele from each parent at
678 every locus (independent assortment, no linkage). The vectorized implementation draws
679 allele choices for all $n_{\text{offspring}} \times 51 \times 2$ positions simultaneously, then indexes into parental
680 genotype arrays.

681 Mutations are applied to offspring genotypes at rate $\mu = 10^{-8}$ per allele per genera-
682 tion [46]. The total number of mutations per cohort is drawn from a Poisson distribution:

683 $n_{\text{mut}} \sim \text{Pois}(\mu \times n_{\text{offspring}} \times 51 \times 2)$. Each mutation flips the allele at a randomly chosen
 684 position ($0 \rightarrow 1$ or $1 \rightarrow 0$), providing bidirectional mutational pressure. At the de-
 685 fault mutation rate, mutations are negligible within the 20–100 year simulation horizon
 686 (expected $\sim 10^{-6}$ mutations per offspring), and evolution proceeds primarily through
 687 selection on standing variation.

688 4.5 Sweepstakes Reproductive Success

689 Broadcast-spawning marine invertebrates exhibit sweepstakes reproductive success (SRS):
 690 a tiny fraction of adults contribute the majority of surviving offspring in any given cohort
 691 [27]. This phenomenon produces N_e/N ratios on the order of 10^{-3} in empirical obser-
 692 vations [3] and dramatically amplifies genetic drift while simultaneously accelerating the
 693 fixation of favorable alleles in post-epidemic populations [14].

694 SSWD-EvoEpi implements SRS via a Pareto-weighted reproductive lottery. Each
 695 spawning adult receives a random weight drawn from a Pareto distribution with shape
 696 parameter α_{SRS} (default 1.35):

$$w_i \sim \text{Pareto}(\alpha_{\text{SRS}}) + 1 \quad (35)$$

697 Female weights are additionally multiplied by size-dependent fecundity (Section 5.5),
 698 so larger females that win the sweepstakes lottery contribute disproportionately:

$$\tilde{w}_{i,\text{female}} = w_i \times \left(\frac{L_i}{L_{\text{ref}}} \right)^b \quad (36)$$

699 where $b = 2.5$ is the fecundity allometric exponent and $L_{\text{ref}} = 500$ mm. Male weights
 700 use the raw Pareto draw without fecundity modulation. Parents are then sampled with
 701 replacement from the normalized weight distributions, and offspring receive Mendelian-
 702 inherited genotypes.

703 The Pareto shape $\alpha_{\text{SRS}} = 1.35$ was chosen to produce N_e/N ratios consistent with
 704 empirical estimates of $\sim 10^{-3}$ in marine broadcast spawners [3, 27]. A small annual
 705 variation in α (drawn from $\mathcal{N}(\alpha_{\text{SRS}}, \sigma_\alpha^2)$ with $\sigma_\alpha = 0.10$) produces temporal fluctuation
 706 in the variance of reproductive success across cohorts.

707 **Effective population size.** N_e is computed from the realized offspring distribution
 708 using the standard formula [27]:

$$N_e = \frac{4N - 2}{V_k + 2} \quad (37)$$

709 where N is the number of spawning parents and V_k is the variance in offspring number.
 710 Sex-specific N_e values are computed for females and males separately, then combined via
 711 harmonic mean: $N_e = 4N_{e,f}N_{e,m}/(N_{e,f} + N_{e,m})$.

712 4.6 Genetic Diagnostics and Tracking

713 The model records a suite of genetic summary statistics at each node at annual intervals:

- 714 • **Per-trait means and variances:** \bar{r} , \bar{t} , \bar{c} and $\text{Var}(r)$, $\text{Var}(t)$, $\text{Var}(c)$.

- 715 • **Additive genetic variance (V_A) per trait:**

$$V_{A,\theta} = \sum_{\ell \in \mathcal{L}_\theta} 2 e_\ell^2 q_\ell (1 - q_\ell) \quad (38)$$

716 where q_ℓ is the derived allele frequency at locus ℓ . V_A determines the potential rate
717 of evolutionary response to selection.

- 718 • **Heterozygosity:** Observed (H_o) and expected (H_e) heterozygosity averaged across
719 all 51 loci.

- 720 • **F_{ST} :** Weir–Cockerham-style F_{ST} across nodes, computed as $F_{ST} = \text{Var}(\bar{q})/[\bar{q}(1-\bar{q})]$
721 averaged across polymorphic loci.

- 722 • **Pre- and post-epidemic allele frequency snapshots:** Full 51-locus allele fre-
723 quency vectors taken immediately before pathogen introduction and two years after
724 the epidemic onset, enabling direct measurement of allele frequency shifts (Δq) at-
725 tributable to selection.

726 **No cost of resistance.** A cost-of-resistance parameter (fecundity penalty for high r_i)
727 was considered but excluded following discussion with the senior author. No empirical
728 evidence supports a measurable fecundity cost for disease resistance alleles in *P. he-
729 lianthoides*, and including an unparameterized cost would introduce a free parameter
730 with no calibration target. Fecundity depends solely on body size (Section 5.5).

731 4.7 Genotype Bank (Tier 2 Nodes)

732 For Tier 2 spatial nodes that use simplified demographics rather than full agent tracking,
733 the genetics module maintains a *genotype bank* of $N_{\text{bank}} = 100$ representative diploid
734 genotypes with associated frequency weights. The bank is created by random sampling
735 from the alive population and preserves all three trait scores and allele frequencies. When
736 agents migrate from a Tier 2 to a Tier 1 node, genotypes are expanded from the bank
737 using SRS-weighted sampling (Pareto weights \times bank frequency weights) to reconstruct
738 individual-level genetic variation.

739 5 Population Dynamics

740 The population dynamics module governs the complete life history of *Pycnopodia helianthoides*: growth, natural mortality, reproduction, larval dispersal, and settlement.
 741 All demographic processes operate on a daily timestep, integrated within the master simulation loop described in Section 2. Disease-driven mortality is handled by the disease
 742 module (Section 3); coupling occurs through shared access to the agent array.

745 5.1 Life Stages

746 Each individual progresses through five life stages defined by size thresholds (Table 5).
 747 Stage transitions are unidirectional: agents can only advance, never regress.

Table 5: Life stages and transition thresholds for *P. helianthoides*.

Stage	Size range	Transition at	Duration
Egg/Larva	Planktonic	Settlement event	49–146 days PLD
Settler	0.5–10 mm	≥ 10 mm	~1 year
Juvenile	10–150 mm	≥ 150 mm	~1–5 years
Subadult	150–400 mm	≥ 400 mm	~5–10 years
Adult	>400 mm	—	10–50+ years

748 5.2 Growth

749 Individual growth follows the von Bertalanffy (VB) growth model in differential form,
 750 resolved daily:

$$L(t + \Delta t) = L_\infty - (L_\infty - L(t)) \cdot \exp(-k_{\text{growth}} \cdot \Delta t) \quad (39)$$

751 where $L_\infty = 1000$ mm is the asymptotic arm-tip diameter, $k_{\text{growth}} = 0.08 \text{ yr}^{-1}$ is the
 752 Brody growth coefficient, and $\Delta t = 1/365 \text{ yr}$ for the daily timestep. Individual growth
 753 variation is introduced through a multiplicative log-normal noise term applied to the daily
 754 increment:

$$\Delta L_i = (L_{\text{det}} - L_i) \cdot \exp(\varepsilon_i), \quad \varepsilon_i \sim \mathcal{N}\left(0, \frac{\sigma_g}{\sqrt{365}}\right) \quad (40)$$

755 where $\sigma_g = 2.0$ mm is the annual growth noise scale and the $\sqrt{365}$ scaling preserves the
 756 annual CV when integrated over daily steps. Size is constrained to never decrease (no
 757 shrinking). Stage transitions are evaluated after each growth step based on the thresholds
 758 in Table 5.

759 Aging proceeds at 1/365 years per day, producing fractional ages that drive size-at-age
 760 trajectories and determine eligibility for senescence mortality.

761 5.3 Natural Mortality

762 Natural mortality is resolved daily using continuous hazard rates derived from stage-
 763 specific annual survival probabilities. The daily death probability for individual i is:

$$p_{\text{death},i} = 1 - (1 - m_{\text{annual}}(s_i))^{1/365} \quad (41)$$

764 where $m_{\text{annual}}(s) = 1 - S_{\text{annual}}(s)$ is the annual mortality rate for stage s . The annual sur-
 765 vival schedule (Table 6) produces a type III survivorship curve with high settler/juvenile
 766 mortality and low adult mortality, consistent with demographic estimates for long-lived
 767 asteroids.

Table 6: Stage-specific annual survival rates.

Stage	Annual survival (S)	Annual mortality
Settler	0.001	0.999
Juvenile	0.03	0.97
Subadult	0.90	0.10
Adult	0.95	0.05
Senescent	0.98	0.02 (base)

768 **Senescence.** Individuals exceeding the senescence age ($a_{\text{sen}} = 50$ yr) accumulate addi-
 769 tional mortality linearly:

$$m_{\text{total}}(s_i, a_i) = m_{\text{annual}}(s_i) + m_{\text{sen}} \cdot \frac{a_i - a_{\text{sen}}}{20} \quad (42)$$

770 where $m_{\text{sen}} = 0.10$ and the divisor of 20 scales the senescence ramp such that a 70-year-old
 771 individual experiences an additional 10% annual mortality.

772 Daily mortality is applied via a single vectorized random draw across all alive agents,
 773 converting stage-dependent annual rates to daily hazard probabilities. This continuous
 774 approach avoids the artificial synchronization artifacts of annual batch mortality and
 775 permits realistic within-year population fluctuations.

776 5.4 Spawning System

777 SSWD-EvoEpi implements a biologically detailed spawning system reflecting the ex-
 778 tended reproductive season and cascading spawning behavior observed in *P. helianthoides*.

779 **5.4.1 Spawning Season and Phenology**

780 The spawning season extends from day 305 (\approx November 1) through day 196 (\approx July 15)
781 of the following year, spanning approximately 270 days and wrapping across the calendar
782 year boundary. Spawning intensity follows a Normal envelope centered on a latitude-
783 adjusted peak:

$$P_{\text{season}}(d) = \exp\left(-\frac{(\Delta d)^2}{2\sigma_{\text{peak}}^2}\right) \quad (43)$$

784 where Δd is the shortest circular distance between day d and the peak day (accounting
785 for year wrapping), and $\sigma_{\text{peak}} = 60$ days is the standard deviation of the seasonal peak.

786 The peak day-of-year is latitude-dependent:

$$d_{\text{peak}}(\phi) = d_{\text{peak,base}} + \lceil (\phi - 40^\circ\text{N}) \times 3 \text{ d}/^\circ \rceil \quad (44)$$

787 where $d_{\text{peak,base}} = 105$ (\approx April 15) is the reference peak at 40°N , and higher-latitude
788 populations spawn approximately 3 days later per degree northward.

789 **5.4.2 Spontaneous Spawning**

790 Each day during the spawning season, mature adults (≥ 400 mm, Susceptible or Recovered
791 disease state) are first evaluated for *readiness*, a stochastic physiological state modulated
792 by the seasonal envelope $P_{\text{season}}(d)$. Once ready, individuals attempt spontaneous spawning
793 with sex-specific daily probabilities:

$$p_{\text{spawn,female}} = 0.012 \quad (45)$$

$$p_{\text{spawn,male}} = 0.0125 \quad (46)$$

794 These rates were calibrated to produce $\geq 80\%$ female spawning participation per season
795 and a mean of ~ 2.2 male bouts per season, consistent with the observation that males
796 spawn more frequently than females in broadcast-spawning asteroids.

797 **Bout limits and refractory periods.** Females are limited to a maximum of 2 spawning
798 bouts per season; males are limited to 3 bouts. Males enter a brief refractory period
799 between bouts (default 0 days, configurable) during which they cannot spawn, reflecting
800 the physiological recovery time for spermatogenesis.

801 **5.4.3 Cascade Induction**

802 Spawning by one individual can trigger spawning in nearby conspecifics via waterborne
803 chemical cues (spawning-induced spawning), producing the synchronous mass spawning

804 events observed in broadcast spawners. Induction operates over a 3-day chemical cue
805 persistence window and is strongly sex-asymmetric:

$$\kappa_{fm} = 0.80 \quad (\text{female} \rightarrow \text{male induction}) \quad (47)$$

$$\kappa_{mf} = 0.60 \quad (\text{male} \rightarrow \text{female induction}) \quad (48)$$

806 where κ_{fm} is the probability that a ready male spawns when a female within the cas-
807 cade radius (200 m) has spawned within the cue window. The female-to-male asymmetry
808 reflects the stronger spawning trigger provided by egg-associated chemical signals. Readi-
809 ness induction also operates: individuals not yet physiologically ready can be driven to
810 readiness by nearby spawning activity, with a daily probability of 0.5 when within a 300 m
811 detection radius.

812 5.4.4 Post-Spawning Immunosuppression

813 Spawning imposes a 28-day immunosuppression period during which the individual's force
814 of infection is multiplied by a susceptibility factor of 2.0:

$$\lambda_i^{\text{eff}} = \lambda_i \times \begin{cases} \chi_{\text{immuno}} = 2.0 & \text{if immunosuppression timer} > 0 \\ 1.0 & \text{otherwise} \end{cases} \quad (49)$$

815 This reflects the metabolic cost of gamete production and the documented increase in
816 disease susceptibility following reproductive investment in marine invertebrates. The
817 immunosuppression timer is reset each time an individual spawns, so multiple spawning
818 bouts within a season extend the vulnerability window. Immunosuppression timers are
819 decremented daily regardless of spawning season status.

820 5.5 Fecundity

821 Female fecundity follows an allometric relationship with body size:

$$F_i = F_0 \cdot \left(\frac{L_i}{L_{\text{ref}}} \right)^b \quad (50)$$

822 where $F_0 = 10^7$ eggs is the reference fecundity at $L_{\text{ref}} = 500$ mm and $b = 2.5$ is the
823 allometric exponent. Only females at or above the minimum reproductive size $L_{\text{min}} =$
824 400 mm produce eggs. No cost-of-resistance penalty is applied to fecundity (Section 4.6).

825 **5.6 Fertilization Kinetics and the Allee Effect**

826 Broadcast spawners face a fertilization Allee effect: at low population density, sperm lim-
827 itation reduces the fraction of eggs successfully fertilized [16, 43]. We model fertilization
828 success using a mean-field approximation of the Lundquist and Botsford [43] broadcast
829 fertilization model:

$$\mathcal{F}(\rho_m) = 1 - \exp(-\gamma_{\text{fert}} \cdot \rho_{m,\text{eff}}) \quad (51)$$

830 where $\gamma_{\text{fert}} = 4.5 \text{ m}^2$ is the sperm contact parameter and $\rho_{m,\text{eff}}$ is the effective male density,
831 potentially enhanced by spawning aggregation behavior. The aggregation factor increases
832 effective local density within spawning clumps above the spatially uniform average when
833 adult count exceeds a threshold.

834 This produces a quadratic relationship between zygote production and density at low
835 density: zygotes $\propto \rho_f \times \mathcal{F}(\rho_m) \propto \rho^2$ when $\rho \rightarrow 0$, creating a strong demographic Allee
836 effect. For high-fecundity broadcast spawners like *P. helianthoides*, the deterministic
837 Allee threshold is near zero density; the practical Allee effect operates through stochastic
838 processes at low N .

839 **5.7 Larval Phase**

840 Fertilized eggs enter a temperature-dependent pelagic larval duration (PLD):

$$\text{PLD}(T) = \text{PLD}_{\text{ref}} \cdot \exp(-Q_{\text{dev}} \cdot (T - T_{\text{ref}})) \quad (52)$$

841 where $\text{PLD}_{\text{ref}} = 63$ days at $T_{\text{ref}} = 10.5^\circ\text{C}$ [35], and $Q_{\text{dev}} = 0.05 \text{ }^\circ\text{C}^{-1}$ produces shorter
842 PLD at warmer temperatures. PLD is clamped to $[30, 150]$ days.

843 Larval survival during the pelagic phase follows a constant daily mortality model:

$$S_{\text{larval}} = \exp(-\mu_{\text{larva}} \cdot \text{PLD}) \quad (53)$$

844 with $\mu_{\text{larva}} = 0.05 \text{ d}^{-1}$. At the reference PLD of 63 days, this yields $S_{\text{larval}} \approx 4.3\%$ — high
845 mortality that is compensated by the enormous fecundity of *P. helianthoides*.

846 Larval cohorts carry genotypes inherited via the SRS lottery (Section 4.5) and are
847 tracked as discrete objects during the pelagic phase. Upon completion of PLD, competent
848 larvae are available for settlement. In the spatial simulation (Section 6), cohorts are
849 dispersed between nodes via the larval connectivity matrix \mathbf{C} before settlement.

850 **5.8 Settlement and Recruitment**

851 Competent larvae settle into the benthic population through a three-stage process:

852 **1. Settlement cue (Allee effect).** Settlement success is modulated by the presence
853 of conspecific adults via a Michaelis–Menten function representing biofilm-mediated
854 settlement cues:

$$C_{\text{settle}}(N_{\text{adults}}) = 0.2 + \frac{0.8 \cdot N_{\text{adults}}}{5 + N_{\text{adults}}} \quad (54)$$

855 where the baseline of 0.2 represents settlement on coralline algae in the absence of adults,
856 and the additional 0.8 reflects enhanced settlement induced by adult biofilm. The half-
857 saturation constant of 5 adults means that even a small remnant population provides
858 strong settlement cues.

859 **2. Density-dependent recruitment (Beverton–Holt).** The number of recruits is
860 governed by a standard Beverton–Holt stock-recruitment relationship:

$$R = \frac{K \cdot s_0 \cdot S}{K + s_0 \cdot S} \quad (55)$$

861 where S is the number of effective settlers (after cue modulation), K is the carrying
862 capacity, and $s_0 = 0.03$ is the density-independent per-settler survival rate. At low S ,
863 $R \approx s_0 S$ (supply-limited); at high S , $R \rightarrow K$ (habitat-limited). For broadcast spawners
864 with $S \gg K$, recruitment is typically habitat-limited and population self-regulates.

865 **3. Agent initialization.** Recruited settlers are placed in dead agent slots, assigned
866 size 0.5 mm, age 0, Settler stage, random sex (1:1 ratio), Susceptible disease state, and
867 random position within the node’s habitat area. Genotypes are copied from the SRS-
868 selected settler genotypes, and all three trait scores (r_i , t_i , c_i) are computed from the
869 inherited genotype.

870 **Juvenile immunity.** Newly settled individuals can optionally be granted a juvenile
871 immunity period (configurable, default 0 days) during which they are not susceptible
872 to infection. The settlement day is recorded for each recruit to enable age-dependent
873 susceptibility calculations.

874 5.9 Continuous Settlement

875 Rather than settling all larvae in an annual pulse, the model tracks individual larval
876 cohorts and settles them daily as their PLD elapses. Cohorts generated by daily spawning
877 events throughout the extended spawning season (Section 5.4.1) are stored in a per-node
878 pending list sorted by settlement day. Each simulation day, cohorts whose PLD has
879 elapsed are popped from the sorted list front (amortized $O(1)$) and passed through the
880 settlement pipeline. This continuous approach produces realistic seasonal recruitment

881 pulses that peak several months after the spawning peak, consistent with the observed
882 temporal offset between spawning and juvenile recruitment in *P. helianthoides*.

883 At the annual boundary, any remaining unsettled cohorts from each node are collected
884 for spatial dispersal via the connectivity matrix \mathbf{C} (Section 6), then redistributed to
885 destination nodes where they continue to settle daily as PLD elapses.

886 5.10 Demographic–Genetic–Epidemiological Coupling

887 The population dynamics module is bidirectionally coupled to the disease and genetics
888 modules:

- 889 • **Disease → demographics:** Disease kills individuals ($I_2 \rightarrow D$), reducing popula-
890 tion size and altering age/size structure. Post-spawning immunosuppression (Sec-
891 tion 5.4.4) increases disease risk for recent spawners, creating a temporal alignment
892 between peak reproductive effort and peak epidemic severity during warm months.
- 893 • **Demographics → disease:** Reduced population density lowers contact rates and
894 environmental pathogen concentration. The fertilization Allee effect (Section 5.6)
895 amplifies population collapse by reducing reproductive output at low density, po-
896 tentially trapping populations in an extinction vortex.
- 897 • **Genetics → demographics:** The SRS lottery (Section 4.5) produces extreme
898 reproductive variance that amplifies genetic drift while accelerating the fixation
899 of resistance, tolerance, and recovery alleles enriched by selection during epidemic
900 episodes.
- 901 • **Demographics → genetics:** Population bottlenecks from disease reduce N_e far
902 below census N , compounded by SRS ($N_e/N \sim 10^{-3}$). The interaction of selection
903 with small effective population size determines whether evolutionary rescue is fast
904 enough to prevent extinction.

905 6 Spatial Module and Environmental Forcing

906 SSWD-EvoEpi represents the NE Pacific range of *Pycnopodia helianthoides* as a metapop-
907 ulation network of discrete spatial nodes connected by larval dispersal and pathogen
908 transport. Each node carries its own environmental forcing (sea surface temperature,
909 salinity, flushing rate) that modulates local disease and demographic dynamics. This sec-
910 tion describes the spatial architecture, connectivity matrices, environmental time series,
911 and agent movement model.

912 6.1 Metapopulation Network Structure

913 The metapopulation is a graph $\mathcal{G} = (\mathcal{N}, \mathbf{C}, \mathbf{D})$ where each node $k \in \mathcal{N}$ represents a geo-
 914 graphically delineated habitat patch and \mathbf{C} , \mathbf{D} are the larval and pathogen connectivity
 915 matrices, respectively.

916 6.1.1 Node Definition

917 Each node is parameterized by a `NodeDefinition` record with the following fields:

Table 7: Node definition fields.

Field	Units	Description
<code>lat, lon</code>	°N, °E	Geographic coordinates
<code>carrying_capacity</code>	individuals	Local K ($=$ habitat area $\times \rho_{\max}$)
<code>is_fjord</code>	bool	Fjord vs. open coast classification
<code>sill_depth</code>	m	Sill depth (∞ for open coast)
<code>flushing_rate</code>	d^{-1}	Mean annual hydrodynamic flushing ϕ_k
<code>mean_sst</code>	°C	Baseline annual mean SST
<code>sst_amplitude</code>	°C	Annual cycle half-range
<code>sst_trend</code>	°C yr $^{-1}$	Linear warming trend
<code>salinity</code>	psu	Effective mean salinity
<code>depth_range</code>	m	Min–max habitat depth
<code>subregion</code>	—	Biogeographic subregion code

918 At runtime, each `NodeDefinition` is wrapped in a `SpatialNode` object that holds the
 919 local population arrays (agents and genotypes), current environmental state (SST, salin-
 920 ity, flushing rate), Vibrio concentration, and diagnostic flags. The `MetapopulationNetwork`
 921 aggregates all nodes together with the \mathbf{C} , \mathbf{D} , and distance matrices.

922 6.1.2 Internode Distance Computation

923 Connectivity kernels require pairwise waterway distances between nodes. Two methods
 924 are available:

925 **Haversine with tortuosity.** For small networks (≤ 11 nodes), geodesic great-circle
 926 distances are computed via the Haversine formula and multiplied by a uniform tortuosity
 927 factor $\tau = 1.5$ (intermediate between open-coast ~ 1.2 and fjord ~ 2.5) to approximate
 928 along-coast path lengths:

$$d_{jk}^{\text{water}} = \tau \times d_{jk}^{\text{Haversine}}. \quad (56)$$

929 **Precomputed overwater distances.** For full-range simulations, a 489-site overwater
930 distance matrix was computed from GEBCO 2022 bathymetric data at 15 arc-second res-
931 olution. Land cells were rasterized from Natural Earth 10 m land polygons, and Dijkstra's
932 algorithm on a 4-connected ocean grid yielded shortest overwater paths. The resulting
933 489×489 matrix spans 2.0–7,187 km, with 98.4% of pairs connected (1,946 disconnected
934 pairs involve western Aleutian sites near the antimeridian). Model nodes are matched
935 to the nearest precomputed site within a 50 km tolerance; unmatched nodes fall back to
936 Haversine $\times \tau$.

937 6.2 Connectivity Matrices

938 Two connectivity matrices govern inter-node exchange: \mathbf{C} for annual larval dispersal and
939 \mathbf{D} for daily pathogen transport (Errata E5). Both use exponential distance kernels but
940 operate at different spatial and temporal scales.

941 6.2.1 Larval Connectivity Matrix \mathbf{C}

942 C_{jk} gives the probability that a competent larva produced at node j settles at node k . The
943 matrix is constructed from an exponential dispersal kernel with explicit self-recruitment:

$$C_{jk} = \begin{cases} \alpha_j & \text{if } j = k, \\ (1 - \alpha_j) \exp\left(-\frac{d_{jk}}{D_L}\right) b_{jk} & \text{if } j \neq k, \end{cases} \quad (57)$$

944 where:

- 945 • $D_L = 400$ km is the larval dispersal length scale, reflecting the 4–8 week pelagic
946 larval duration (PLD) of *Pycnopodia helianthoides* [65];
- 947 • α_j is the self-recruitment fraction: $\alpha_{\text{fjord}} = 0.30$ for fjord nodes (reflecting enhanced
948 retention behind sills) and $\alpha_{\text{open}} = 0.10$ for open-coast nodes;
- 949 • $b_{jk} \in [0, 1]$ is an optional barrier attenuation factor for biogeographic breaks (e.g.,
950 Cape Mendocino).

951 Rows are then normalized so that:

$$\sum_k C_{jk} = r_{\text{total}} = 0.02, \quad (58)$$

952 where r_{total} represents the total per-larva settlement success probability, accounting for
953 the compounding losses of pelagic mortality, failed metamorphosis, and post-settlement
954 predation.

955 The elevated self-recruitment fraction for fjord nodes ($\alpha_{\text{fjord}} = 3\alpha_{\text{open}}$) encodes the em-
 956 pirical observation that fjords act as larval retention zones [67]: sill-mediated circulation
 957 traps larvae near their natal site, reducing export to the open coast.

958 **6.2.2 Pathogen Dispersal Matrix D**

959 D_{jk} gives the fraction of waterborne *Vibrio pectenicida* at node j that reaches node k per
 960 day. Pathogen dispersal operates at much shorter range than larval dispersal:

$$D_{jk} = \phi_j f_{\text{out}} \exp\left(-\frac{d_{jk}}{D_P}\right) S_{jk} \quad \text{for } d_{jk} \leq 50 \text{ km}, \quad (59)$$

961 where:

- 962 • $D_P = 15$ km is the pathogen dispersal scale (reflecting tidal-current transport);
- 963 • ϕ_j is the source node's flushing rate (d^{-1});
- 964 • $f_{\text{out}} = 0.2$ is the fraction of flushed water reaching neighboring sites;
- 965 • S_{jk} is the sill attenuation factor.

966 Pairs beyond $d_{jk} > 50$ km receive zero pathogen transfer. Total export from any node
 967 is capped at its flushing rate: $\sum_k D_{jk} \leq \phi_j$.

968 **Sill attenuation.** Fjord sills impede pathogen exchange between basins. The attenu-
 969 ation factor is computed from the minimum sill depth across the pair:

$$S_{jk} = \min\left(1, \left[\frac{\min(z_j^{\text{sill}}, z_k^{\text{sill}})}{\max(z_j^{\text{max}}, z_k^{\text{max}})}\right]^2\right), \quad (60)$$

970 where z^{sill} is sill depth and z^{max} is maximum habitat depth. For open-coast nodes ($z^{\text{sill}} =$
 971 ∞), $S_{jk} = 1$ (no attenuation). For Howe Sound (sill = 30 m, max depth = 100 m),
 972 $S \approx 0.09$, reducing pathogen exchange by $\sim 91\%$.

973 **6.2.3 Dispersal Dynamics**

974 **Pathogen dispersal (daily).** At each timestep, the dispersal input to node k is:

$$\Delta P_k^{\text{dispersal}} = \sum_j D_{jk} P_j = (\mathbf{D}^\top \mathbf{P})_k, \quad (61)$$

975 which enters the Vibrio ODE (Eq. 17) as an additive source term.

976 **Larval dispersal (annual).** At the end of each reproductive season, competent larvae
 977 from each source node are distributed to receiving nodes via \mathbf{C} . For source node j
 978 producing n_j competent larvae: (i) a binomial draw $n_{\text{settle}} \sim \text{Bin}(n_j, \sum_k C_{jk})$ determines
 979 total settlement; (ii) a multinomial draw allocates settlers across destinations proportional
 980 to the conditional probabilities $C_{jk} / \sum_k C_{jk}$; (iii) settler genotypes are sampled with
 981 replacement from the source pool.

982 6.3 Environmental Forcing

983 Each node receives a locally parameterized environmental forcing that drives disease
 984 and demographic rates through temperature-dependent, salinity-dependent, and flushing-
 985 dependent mechanisms.

986 6.3.1 Sea Surface Temperature

987 The model supports two SST forcing modes, selected via the `sst_source` configuration
 988 parameter:

989 **Satellite climatology (default for validation).** Daily SST forcing uses climatologi-
 990 cal means derived from the NOAA Optimum Interpolation SST v2.1 dataset [53], a 0.25°
 991 daily global product spanning 1981–present. For each node, the 365-day climatology is
 992 computed as the 2002–2025 day-of-year average, extracted via ERDDAP for the node’s
 993 geographic coordinates. This approach captures real seasonal dynamics including asym-
 994 metric warming/cooling profiles and coastal upwelling effects that a symmetric sinusoidal
 995 function cannot represent. A configurable linear warming trend γ_k ($^\circ\text{C yr}^{-1}$; default 0.02)
 996 is overlaid for future projection scenarios:

$$T_k(d, y) = T_{k,\text{clim}}(d) + \gamma_k (y - y_{\text{ref}}), \quad (62)$$

997 where $T_{k,\text{clim}}(d)$ is the satellite-derived climatological SST for day-of-year d at node k .

998 **Sinusoidal approximation (fallback).** For nodes lacking satellite data or for rapid
 999 prototyping, SST follows a sinusoidal annual cycle:

$$T_k(d, y) = \underbrace{\bar{T}_k + \gamma_k (y - y_{\text{ref}})}_{\text{trend-adjusted mean}} + \underbrace{A_k \cos\left(\frac{2\pi(d - d_{\text{peak}})}{365}\right)}_{\text{annual cycle}}, \quad (63)$$

1000 where \bar{T}_k is the baseline annual mean SST, A_k the annual cycle half-range, and $d_{\text{peak}} = 227$
 1001 (day of year \approx August 15) corresponds to the late-summer SST maximum characteristic
 1002 of the NE Pacific.

1003 For the 11-node stepping-stone network used in sensitivity analysis, satellite climatolo-
 1004 gies produce a $\sim 6^\circ\text{C}$ latitudinal gradient from Sitka ($\sim 8^\circ\text{C}$ annual mean) to Monterey
 1005 ($\sim 13^\circ\text{C}$), consistent with published SST atlases. The satellite forcing also captures site-
 1006 specific features such as the narrow summer peak at upwelling-dominated sites (Newport,
 1007 Crescent City) versus the broader warm season at sheltered sites (Howe Sound).

1008 SST time series are precomputed at initialization via `generate_satellite_sst_series`
 1009 (satellite mode) or `make_sst_timeseries` (sinusoidal mode) and stored as dense 1-D ar-
 1010 rays of shape ($n_{\text{years}} \times 365$) for efficient daily lookup.

1011 6.3.2 Temperature-Dependent Rate Scaling

1012 All temperature-dependent biological rates—disease progression, pathogen shedding, Vib-
 1013 ryo decay—are scaled via the Arrhenius function:

$$k(T) = k_{\text{ref}} \exp \left[\frac{E_a}{R} \left(\frac{1}{T_{\text{ref}}} - \frac{1}{T} \right) \right], \quad (64)$$

1014 with $T_{\text{ref}} = 293.15\text{ K}$ (20°C), the thermal optimum of *Vibrio pectenicida* [38]. This
 1015 formulation ensures that the latitudinal SST gradient (Eq. 63) produces emergent north–
 1016 south gradients in disease severity, matching the observed pattern of southward-increasing
 1017 SSWD mortality during the 2013–2015 outbreak [25, 51].

1018 6.3.3 Salinity Modifier

1019 Vibrio viability is suppressed at low salinities via a quadratic ramp (Eq. 7), reproduced
 1020 here for completeness:

$$S_{\text{sal}} = \text{clip} \left(\left[\frac{S_k - S_{\min}}{S_{\text{full}} - S_{\min}} \right]^2, 0, 1 \right), \quad S_{\min} = 10 \text{ psu}, \quad S_{\text{full}} = 28 \text{ psu}. \quad (65)$$

1021 Fjord nodes receive lower salinities (e.g., Howe Sound $S = 22\text{ psu}$ due to freshwater
 1022 runoff), yielding $S_{\text{sal}} = 0.44$ and reducing effective Vibrio viability by $\sim 56\%$ compared
 1023 to open-coast nodes ($S \geq 30\text{ psu}$, $S_{\text{sal}} \geq 0.87$). This mechanism provides a partial
 1024 explanation for fjord refugia observations [51].

1025 6.3.4 Flushing Rate

1026 Hydrodynamic flushing removes waterborne pathogen at rate $\phi_k (\text{d}^{-1})$, entering the Vibrio
 1027 ODE as the term $-\phi_k P_k$ (Eq. 17). Node-specific values span two orders of magnitude:

- 1028 • Open coast: $\phi_k = 0.5\text{--}1.0 \text{ d}^{-1}$ (strong tidal and current flushing);
- 1029 • Semi-enclosed bays: $\phi_k = 0.3 \text{ d}^{-1}$ (San Juan Islands);

- 1030 • Fjords: $\phi_k = 0.007\text{--}0.05 \text{ d}^{-1}$ (Errata E3; sill restricts water exchange). Howe Sound
1031 is assigned $\phi_k = 0.03 \text{ d}^{-1}$.

1032 Low flushing in fjords acts as a double-edged mechanism: it reduces the rate of
1033 pathogen removal (potentially increasing local Vibrio concentrations) but also reduces
1034 pathogen *export* to neighboring nodes via \mathbf{D} (Eq. 59), effectively isolating the fjord from
1035 regional epidemic dynamics.

1036 Flushing rates are optionally modulated seasonally:

$$\phi_k(m) = \bar{\phi}_k \left[1 + A_\phi \cos\left(\frac{2\pi(m-5)}{12}\right) \right], \quad (66)$$

1037 where m is the 0-indexed month, $A_\phi = 0.3$ for fjord nodes and $A_\phi = 0.2$ for open
1038 coast, with peak flushing in June ($m = 5$) corresponding to freshwater-driven estuarine
1039 circulation maxima.

1040 6.4 Agent Movement

1041 Within each node, agents move via a correlated random walk (CRW) that produces
1042 realistic small-scale spatial structure:

$$\theta(t + \Delta t) = \theta(t) + \mathcal{N}(0, \sigma_\theta^2), \quad (67)$$

$$x(t + \Delta t) = x(t) + v_i \cos \theta \Delta t, \quad (68)$$

$$y(t + \Delta t) = y(t) + v_i \sin \theta \Delta t, \quad (69)$$

1043 where $\sigma_\theta = 0.6 \text{ rad}$ is the turning-angle standard deviation, $v_i = v_{\text{base}} \times m_{\text{state}}$ is the
1044 disease-modified speed, and $\Delta t = 60 \text{ min}$ (hourly substeps, 24 per day). The base speed
1045 $v_{\text{base}} = 0.5 \text{ m min}^{-1}$ is consistent with undisturbed *Pycnopodia helianthoides* locomotion
1046 rates [37]. Disease state modifies speed: $m_S = m_E = 1.0$ (healthy), $m_{I_1} = 0.5$ (mild
1047 impairment), $m_{I_2} = 0.1$ (severe wasting), $m_D = 0.0$ (stationary carcass), $m_R = 1.0$
1048 (recovered).

1049 Agents are confined to a square habitat of side length $\sqrt{\text{habitat_area}}$ with elastic
1050 boundary reflection.

1051 **Spatial transmission.** When spatial transmission is enabled, each node's habitat is
1052 discretized into a grid with cell size $\Delta x = 20 \text{ m}$. Infected agents deposit pathogen expo-
1053 sure proportional to their shedding rate into their grid cell, and two Gaussian diffusion
1054 passes (3×3 averaging) smooth the resulting density field. Susceptible agents then experi-
1055 ence locally elevated or reduced force of infection depending on their proximity to infected
1056 individuals, creating emergent disease clustering without modifying the node-level Vibrio
1057 ODE.

1058 **Sensitivity analysis substeps.** The full 24 hourly substeps per day incur $\sim 20 \times$ com-
1059 putational overhead. For sensitivity analysis runs (Section ??), movement is reduced to
1060 1 substep per day, which captures spatial mixing and aggregation effects at acceptable
1061 cost.

1062 6.5 Network Configurations

1063 Three network configurations are used across model development, validation, and sensi-
1064 tivity analysis.

1065 6.5.1 5-Node Validation Network

1066 The primary validation network spans the NE Pacific range with five nodes selected to
1067 represent key biogeographic contexts (Table 8):

Table 8: 5-node validation network configuration. SST parameters are baseline values at reference year 2000.

Node	Lat	Lon	\bar{T} ($^{\circ}\text{C}$)	A ($^{\circ}\text{C}$)	S (psu)	ϕ (d^{-1})
Sitka, AK	57.06	-135.34	8.0	3.5	32.0	0.80
Howe Sound, BC	49.52	-123.25	10.0	4.0	22.0	0.03
San Juan Is, WA	48.53	-123.02	10.0	4.0	30.0	0.30
Newport, OR	44.63	-124.05	12.0	3.0	33.0	1.00
Monterey, CA	36.62	-121.90	14.0	2.5	33.5	0.80

1068 Howe Sound is the sole fjord node (sill depth = 30 m, $\alpha_{\text{self}} = 0.30$); all others are open
1069 coast ($\alpha_{\text{self}} = 0.10$). Node carrying capacities range from 400 (Howe Sound) to 1,000
1070 (Sitka). This network reproduces three key empirical patterns: the north–south SSWD
1071 mortality gradient, fjord protection, and the absence of recovery in southern populations
1072 (Section 8).

1073 6.5.2 11-Node Sensitivity Analysis Network

1074 Sensitivity analysis Rounds 1–3 used a minimal 3-node network (Sitka, Howe Sound,
1075 Monterey) with inter-node distances of 1,700+ km—far exceeding the larval dispersal
1076 scale $D_L = 400$ km. Consequently, the spatial connectivity parameters (D_L , α_{self}) were
1077 effectively untestable, as the exponential kernel $\exp(-1700/400) < 10^{-2}$ produced negligi-
1078 ble inter-node exchange regardless of D_L values within the SA range.

1079 Round 4 introduced an 11-node stepping-stone chain with six additional intermediate
1080 nodes (Table 9), reducing maximum inter-node spacing to ~ 452 km and ensuring that
1081 D_L values within the SA range [100, 1,000] km produce meaningful variation in larval ex-
1082 change (32–76% at adjacent-node distances of 110–452 km with the default $D_L = 400$ km).

Table 9: 11-node stepping-stone network for sensitivity analysis Round 4. All nodes have $K = 5,000$ ($\sim 55,000$ total agents). SST trend = $0.02^{\circ}\text{C yr}^{-1}$ for all nodes.

Node	Lat	Lon	\bar{T} ($^{\circ}\text{C}$)	A ($^{\circ}\text{C}$)	S (psu)	ϕ (d^{-1})
Sitka	57.06	-135.34	8.0	3.5	32.0	0.80
Ketchikan	55.34	-131.64	8.5	3.5	31.0	0.50
Haida Gwaii	53.25	-132.07	9.0	3.0	31.5	0.60
Bella Bella	52.16	-128.15	9.5	3.5	28.0	0.40
Howe Sound*	49.52	-123.25	10.0	4.0	22.0	0.03
SJI	48.53	-123.02	10.5	4.0	30.0	0.30
Westport	46.89	-124.10	11.0	3.5	32.0	0.50
Newport	44.63	-124.05	11.5	3.0	33.0	0.60
Crescent City	41.76	-124.20	12.0	2.5	33.0	0.50
Fort Bragg	39.45	-123.80	12.5	2.5	33.5	0.50
Monterey	36.62	-121.90	13.0	2.5	33.5	0.40

*Fjord node (sill depth = 30 m, $\alpha_{\text{self}} = 0.30$). All other nodes open coast ($\alpha_{\text{self}} = 0.10$).

1083 This upgrade substantially altered parameter importance rankings: $n_{\text{resistance}}$ rose from
 1084 rank 19 to rank 5 (the three-trait partition amplifies genetic architecture importance at
 1085 finer spatial scales), and $P_{\text{env},\text{max}}$ rose from rank 11 to rank 4 (the environmental reservoir
 1086 becomes critical with more nodes seeding independent epidemics). See Section ?? for full
 1087 results.

1088 6.5.3 Full-Range Network (Planned)

1089 Scaling analysis (Section 8) demonstrated that the model supports 150-node networks at
 1090 ~ 66 s per 20-year run, enabling a full NE Pacific coastline simulation (Alaska to Baja
 1091 California). This configuration will use the precomputed 489-site overwater distance
 1092 matrix (Section 6.1.2) and site-specific SST forcing from satellite climatologies.

1093 6.6 Network Construction

1094 The `build_network` function assembles the metapopulation from a list of node definitions
 1095 by: (i) computing the pairwise distance matrix (Haversine $\times \tau$ or precomputed overwater
 1096 distances); (ii) constructing **C** with per-node α_j values (α_{fjord} or α_{open}), the D_L kernel,
 1097 optional barrier factors, and row normalization to r_{total} ; (iii) constructing **D** with the D_P
 1098 kernel, flushing-rate modulation, sill attenuation, and the 50 km cutoff; and (iv) wrapping
 1099 each node definition in a **SpatialNode** with initialized environmental state. The function
 1100 accepts optional parameters for all kernel scales, self-recruitment fractions, and barrier
 1101 configurations, allowing the same codebase to serve validation, sensitivity analysis, and
 1102 full-range simulation.

1103 7 Sensitivity Analysis

1104 The SSWD-EvoEpi model contains 47 uncertain parameters spanning six modules: dis-
1105 ease transmission and progression (16 parameters), genetics and trait architecture (8),
1106 population dynamics (7), spawning biology (7), pathogen virulence evolution (6), and
1107 spatial connectivity (3). Most of these parameters have limited empirical constraints
1108 (Section A), necessitating a systematic sensitivity analysis (SA) to identify which param-
1109 eters most influence model behavior and, critically, which parameter *interactions* domi-
1110 nate the system’s dynamics. We conducted a progressive, four-round SA campaign that
1111 tracked the model’s growing complexity from a single-trait, 3-node prototype through to
1112 the full three-trait, 11-node eco-evolutionary framework.

1113 7.1 Methods

1114 7.1.1 Morris Elementary Effects Screening

1115 Each SA round began with Morris elementary effects screening [52], implemented via the
1116 SALib Python library [28]. The Morris method is a one-at-a-time (OAT) design in which
1117 each parameter is perturbed along r independent trajectories through the p -dimensional
1118 input space. For parameter x_i in trajectory j , the elementary effect is

$$d_{ij} = \frac{f(x_1, \dots, x_i + \Delta_i, \dots, x_p) - f(x_1, \dots, x_i, \dots, x_p)}{\Delta_i}, \quad (70)$$

1119 where Δ_i is the perturbation step. From these we compute two summary statistics per
1120 parameter per metric [8]:

- 1121 • μ_i^* : the mean of the *absolute* elementary effects, measuring overall parameter im-
1122 portance regardless of sign;
- 1123 • σ_i : the standard deviation of elementary effects, measuring interaction and nonlin-
1124 earity strength.

1125 When $\sigma_i/\mu_i^* > 1$, the parameter’s influence on the metric is dominated by interactions
1126 with other parameters rather than by its direct (additive) effect [59]. To enable cross-
1127 metric comparison, we normalize μ^* by the range of the metric across all trajectories,
1128 then rank parameters by the mean normalized μ^* across all output metrics.

1129 All rounds used $r = 20$ trajectories, yielding $r \times (p + 1)$ total model evaluations per
1130 round (e.g., $20 \times 48 = 960$ runs for the 47-parameter Round 4).

1131 7.1.2 Sobol Variance Decomposition

1132 Parameters surviving Morris screening advance to Sobol variance-based global sensitivity
1133 analysis [64], which decomposes the total output variance into contributions from individ-

1134 ual parameters and their interactions. Using the Saltelli sampling scheme [58], $N(2p + 2)$
1135 model evaluations produce two key indices for each parameter x_i and output metric Y :

- 1136 \bullet $S_{1,i} = V_{x_i}[E_{x \sim i}(Y|x_i)] / V(Y)$: the *first-order* Sobol index, measuring the fraction
1137 of output variance attributable to x_i alone;
- 1138 \bullet $S_{T,i} = 1 - V_{x \sim i}[E_{x_i}(Y|x \sim i)] / V(Y)$: the *total-order* index, capturing x_i 's contribu-
1139 tion including all interactions with other parameters.

1140 The gap $S_{T,i} - S_{1,i}$ quantifies the strength of parameter interactions. When $S_{T,i} \gg S_{1,i}$, the
1141 parameter's influence is mediated primarily through joint effects with other parameters,
1142 implying that it cannot be calibrated independently.

1143 7.1.3 Output Metrics

1144 The SA tracks 23 output metrics capturing demographic, evolutionary, spatial, and
1145 pathogen outcomes over 20-year simulations:

- 1146 \bullet **Demographic:** population crash percentage, final population fraction, recovery
1147 (population returns to >50% of initial), extinction (metapopulation collapse), peak
1148 single-year mortality, time to population nadir, total disease deaths, disease death
1149 fraction;
- 1150 \bullet **Evolutionary (host):** mean and maximum resistance shift ($\Delta\bar{r}$), tolerance shift
1151 ($\Delta\bar{t}$), recovery-trait shift ($\Delta\bar{c}$), additive variance retention ($V_A^{\text{post}}/V_A^{\text{pre}}$), evolution-
1152 ary rescue index (composite of survival and resistance gain), total recovery events,
1153 recovery rate;
- 1154 \bullet **Spatial:** number of extinct nodes, north–south mortality gradient, fjord protection
1155 effect;
- 1156 \bullet **Pathogen:** mean final virulence, virulence shift ($\Delta\bar{v}$);
- 1157 \bullet **Spawning:** spawning participation rate, mean recruitment rate.

1158 7.2 Progressive Sensitivity Analysis Design

1159 The SA was conducted in four rounds (Table 10), each corresponding to a major model
1160 extension. This progressive design allows us to track how parameter importance shifts as
1161 model complexity grows—a critical diagnostic for identifying emergent behaviors intro-
1162 duced by new modules.

Table 10: Summary of sensitivity analysis rounds. Each round incorporates all changes from prior rounds. “New” parameters are those added relative to the previous round.

Round	Params	Metrics	Nodes	Runs	Key Changes
R1 (Morris)	23	14	3	480	Baseline: single resistance trait
R2 (Sobol)	23	14	3	12,288	Sobol decomposition of R1 params
R3 (Morris)	43	20	3	880	+20 params: pathogen evo, spawning, continuous mortality, daily growth
R4 (Morris)	47	23	11	960	+4 params: three-trait genetics, 11-node stepping-stone network

1163 **Rounds 1–2 (Pre-Three-Trait Baseline).** The initial SA (Rounds 1–2) examined
1164 23 parameters across disease (13), population (7), genetics (1: n_{additive}), and spawning
1165 (2) modules using a 3-node spatial network (Sitka, Howe Sound, Monterey; $K = 5,000$
1166 per node). The model at this stage tracked a single resistance trait with n_{additive} additive
1167 loci. Morris screening (480 runs) retained all 23 parameters for Sobol analysis (12,288
1168 runs, $N = 256$).

1169 The Sobol decomposition revealed that disease progression rate $\mu_{I2D,\text{ref}}$ ($I_2 \rightarrow \text{Death}$)
1170 was the single most influential parameter (mean $S_T = 0.638$), followed by susceptibility_multiplier
1171 ($S_T = 0.540$) and a_{exposure} ($S_T = 0.473$). A critical methodological finding was that Mor-
1172 ris and Sobol rankings *disagreed*: Morris identified `settler_survival` and ρ_{rec} as the
1173 top drivers of population outcomes, while Sobol elevated susceptibility_multiplier and
1174 $\mu_{I2D,\text{ref}}$. This discrepancy arises because Morris measures marginal effects from extreme-
1175 value perturbations, whereas Sobol captures variance-weighted contributions including
1176 interactions. This confirmed that Morris screening alone is insufficient for identifying
1177 calibration priorities in this model.

1178 **Round 3 (Expanded Model, 3-Node).** Round 3 added 20 parameters from four
1179 newly implemented modules: pathogen virulence evolution (6 parameters: virulence–
1180 fitness tradeoff exponents, mutation rate, initial virulence), expanded spawning biology
1181 (4: male spontaneous spawning, readiness induction, female bout limits, peak width), and
1182 additional disease mechanics (immunosuppression duration, minimum susceptible age,
1183 $I_1 \rightarrow I_2$ progression rate) and genetics parameters (target_mean_r, Beta-distribution
1184 shape parameters for initial allele frequencies). The network remained at 3 nodes for
1185 comparability with R1–R2.

1186 Morris screening (880 runs, 20 trajectories) revealed a dramatic reshuffling: ρ_{rec} (re-
1187 covery rate) rose to #1 ($\mu_{\text{norm}}^* = 0.642$), displacing $\mu_{I2D,\text{ref}}$ from its R1–R2 dominance.
1188 This occurred because the transition from discrete-stage to continuous daily mortality
1189 diluted the $I_2 \rightarrow \text{Death}$ rate’s marginal influence, while recovery rate’s role was amplified
1190 by its interaction with the new pathogen evolution module (higher ρ_{rec} imposes stronger
1191 selection against virulent strains). All 43 parameters exceeded the 5% elimination thresh-

1192 old; zero were pruned.

1193 **Round 4 (Full Model, 11-Node).** Round 4 represents the complete SSWD-EvoEpi
1194 model with two additions: (1) the three-trait genetic architecture (resistance, tolerance,
1195 recovery; Section 4.1), contributing four new parameters (`target_mean_c`, `target_mean_t`,
1196 τ_{\max} , $n_{tolerance}$); and (2) an 11-node stepping-stone network spanning the latitudinal range
1197 of *Pycnopodia helianthoides* habitat. The expanded spatial network was critical for re-
1198 solving spatial parameters that were undetectable at 3 nodes. This round (960 runs, 48
1199 cores on an Intel Xeon W-3365) provides the most comprehensive screening of the model
1200 to date.

1201 7.3 Round 4 Morris Results

1202 7.3.1 Global Parameter Ranking

1203 Table 12 presents the complete Round 4 Morris ranking for all 47 parameters, sorted by
1204 mean normalized μ^* across 23 output metrics. Figure 1 shows the top 20 parameters
1205 color-coded by module.

1206 The top-10 parameters span four of six modules:

- 1207 1. ρ_{rec} (recovery rate; $\mu_{\text{norm}}^* = 0.889$) — the rate at which infected individuals clear
1208 pathogen remains the single most influential parameter, as in R3. Its semi-additive
1209 behavior ($\sigma/\mu^* = 1.46$, the lowest interaction ratio of any parameter) reflects its
1210 direct mechanistic role: daily clearance probability $p_{\text{rec}} = \rho_{\text{rec}} \times c_i$ scales linearly
1211 with this rate regardless of other parameter values.
- 1212 2. k_{growth} (von Bertalanffy growth rate; $\mu_{\text{norm}}^* = 0.633$) — faster growth accelerates
1213 maturation and spawning eligibility, providing demographic compensation during
1214 epidemics. Rose from #5 (R3) to #2.
- 1215 3. K_{half} (half-infective dose; $\mu_{\text{norm}}^* = 0.622$) — the Michaelis–Menten saturation pa-
1216 rameter controlling infection probability. Rose from #8 to #3.
- 1217 4. $P_{\text{env,max}}$ (environmental reservoir; $\mu_{\text{norm}}^* = 0.598$) — background waterborne *V. pecteni-*
1218 *cida* input, independent of host shedding. Rose dramatically from #11 to #4,
1219 reflecting its interaction with the 11-node spatial network where environmental
1220 pathogen load varies with latitude and temperature.
- 1221 5. $n_{\text{resistance}}$ (number of resistance loci; $\mu_{\text{norm}}^* = 0.525$) — genetic architecture of re-
1222 sistance. The largest rank gain of any parameter: #19 → #5 ($\Delta = +14$). The
1223 three-trait partition (17 loci per trait vs. the former 51 total) amplifies the sensi-
1224 tivity to how many loci underlie each defense mechanism.

- 1225 6. s_0 (settler survival; $\mu_{\text{norm}}^* = 0.509$) — Beverton–Holt baseline recruitment. Dropped
1226 modestly from #3 to #6.
- 1227 7. $\sigma_{2,\text{eff}}$ (late-stage shedding rate; $\mu_{\text{norm}}^* = 0.431$).
- 1228 8. $\mu_{I2D,\text{ref}}$ ($I_2 \rightarrow$ Death rate; $\mu_{\text{norm}}^* = 0.419$) — formerly the #1 parameter in R1–R2
1229 Sobol ($S_T = 0.638$), now #8 in R4 Morris.
- 1230 9. σ_{spawn} (spawning peak width; $\mu_{\text{norm}}^* = 0.392$) — controls synchrony of the repro-
1231 ductive pulse; dropped from #2 to #9.
- 1232 10. target_mean_c (initial mean recovery trait; $\mu_{\text{norm}}^* = 0.385$) — a new R4 parame-
1233 ter entering directly at #10, confirming that the recovery trait (c_i) is the fastest-
1234 evolving defense in the model (Section 4.1).

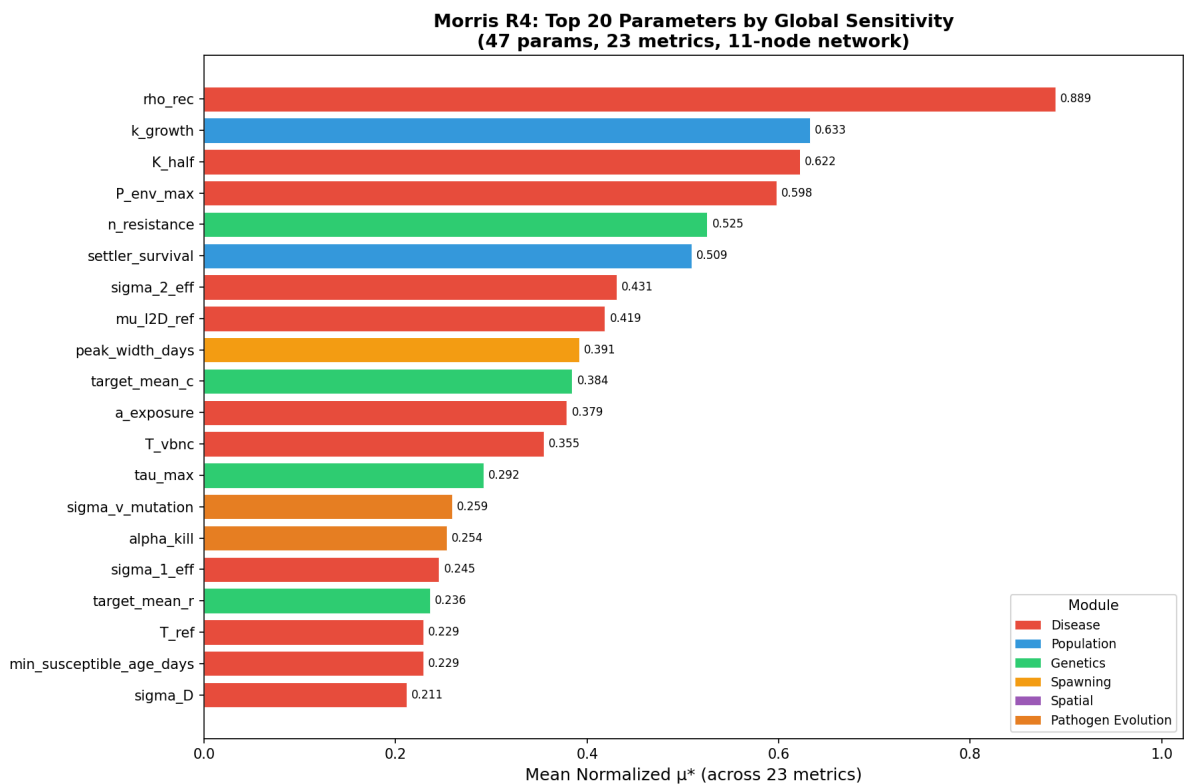


Figure 1: Top 20 parameters by mean normalized μ^* in Round 4 Morris screening (47 parameters, 23 metrics, 11-node network, 960 runs). Bars are color-coded by module. Error bars show 95% bootstrap confidence intervals across 20 trajectories.

1235 7.3.2 Key Rank Shifts from Round 3

1236 The transition from R3 to R4 produced dramatic rank changes (Figure 2), driven by two
1237 structural changes: the three-trait genetic architecture and the 11-node spatial network.

1238 **Major rank gains.** Six parameters gained ≥ 7 ranks (Table 11):

- 1239 • $\sigma_{1,\text{eff}}$ (early shedding rate): #43 → #16 ($\Delta = +27$). Early shedding now interacts
1240 with pathogen evolution: σ_1 shapes the initial epidemic wave that determines the
1241 selection regime on virulence.
- 1242 • $\sigma_{v,\text{mut}}$ (virulence mutation step size): #31 → #14 ($\Delta = +17$). With 11 nodes
1243 providing diverse thermal and demographic environments, mutation rate controls
1244 how fast pathogen lineages adapt to local conditions.
- 1245 • T_{ref} (pathogen temperature optimum): #34 → #18 ($\Delta = +16$). The latitudinal
1246 temperature gradient across 11 nodes (vs. 3) amplifies the importance of the thermal
1247 reference point.
- 1248 • $n_{\text{resistance}}$: #19 → #5 ($\Delta = +14$), as discussed above.
- 1249 • $\alpha_{\text{self,open}}$ (open-coast larval retention): #39 → #25 ($\Delta = +14$). Spatial retention
1250 was invisible at 3 nodes but becomes detectable with 11 nodes and realistic dispersal
1251 distances.
- 1252 • $P_{\text{env,max}}$: #11 → #4 ($\Delta = +7$).

1253 **Major rank drops.** Five parameters dropped ≥ 19 ranks:

- 1254 • q_{init,β_b} (Beta-distribution shape b): #17 → #46 ($\Delta = -29$). Initial allele-frequency
1255 shape is overwhelmed by the trait-specific mean parameters (target_mean_r/t/c).
- 1256 • F_0 (reference fecundity): #20 → #47 ($\Delta = -27$). Diluted in the expanded 47-
1257 parameter space.
- 1258 • Immunosuppression duration: #15 → #42 ($\Delta = -27$). Its effect is absorbed
1259 by spawning parameters and the recovery trait (c_i), which provides an alternative
1260 pathway through immunosuppressed periods.
- 1261 • susceptibility_multiplier: #23 → #44 ($\Delta = -21$). This parameter was #1 in the
1262 R1–R2 Sobol analysis ($S_T = 0.540$); its precipitous decline reflects absorption by
1263 the explicit resistance genetics—individual r_i now captures susceptibility variation
1264 mechanistically, rendering the multiplicative modifier redundant.
- 1265 • p_{spont} , (female spontaneous spawning): #26 → #45 ($\Delta = -19$).

Morris R3→R4: Parameter Rank Changes
 (43 common params; R4 adds 4 new: n_tolerance, target_mean_t, target_mean_c, tau_max)

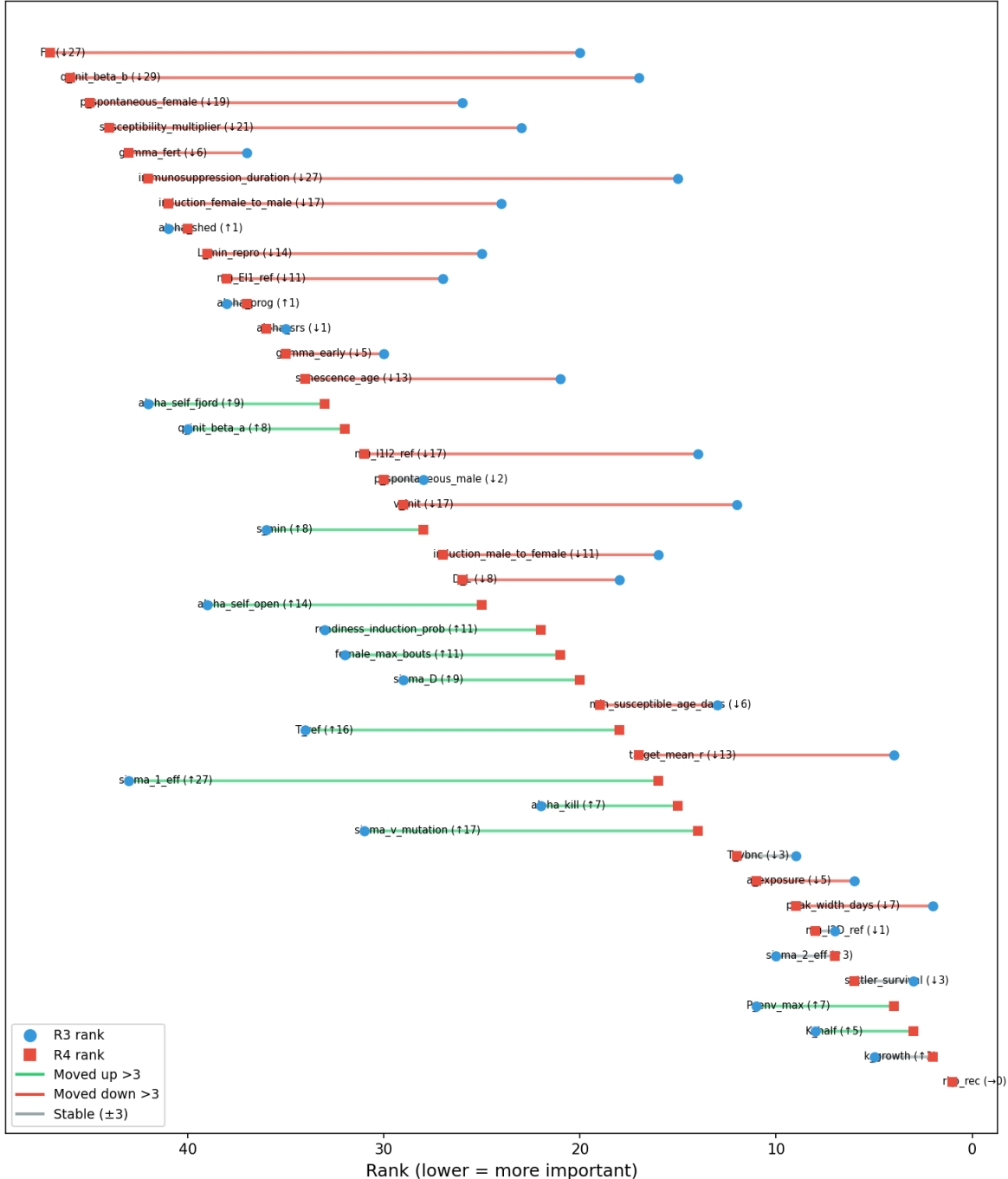


Figure 2: Rank change from Round 3 to Round 4 for the 43 parameters common to both rounds. Positive values (rightward) indicate increased importance in R4; negative values (leftward) indicate decreased importance. Parameters are sorted by R4 rank. Four new R4 parameters (not shown) entered at ranks #10, #13, #23, and #24.

Table 11: Largest rank shifts from R3 to R4 Morris screening. Positive Δ indicates increased importance.

Parameter	Module	R3 → R4	Δ	Mechanism
$\sigma_{1,\text{eff}}$	Disease	43 → 16	+27	Interacts with pathogen evolution
$\sigma_{v,\text{mut}}$	Pathogen evo.	31 → 14	+17	Controls adaptation speed
T_{ref}	Disease	34 → 18	+16	11-node thermal gradient
$n_{\text{resistance}}$	Genetics	19 → 5	+14	Three-trait partition
$\alpha_{\text{self},\text{open}}$	Spatial	39 → 25	+14	Resolvable at 11 nodes
q_{init,β_b}	Genetics	17 → 46	-29	Absorbed by trait means
F_0	Population	20 → 47	-27	Diluted in larger space
Immunosupp. duration	Disease	15 → 42	-27	Absorbed by recovery trait
Suscept. multiplier	Disease	23 → 44	-21	Absorbed by resistance genetics

1266 7.3.3 New Three-Trait Parameters

1267 The four parameters introduced with the three-trait architecture (Section 4.1) immedi-
 1268 ately demonstrated meaningful sensitivity:

- 1269 • target_mean_c (initial mean recovery trait): rank #10 ($\mu_{\text{norm}}^* = 0.385$). A top-
 1270 10 entry confirms that recovery (c_i) is the dominant evolutionary pathway in the
 1271 model, consistent with the validation finding that $\Delta\bar{c}$ exceeds $\Delta\bar{r}$ by $\sim 7\times$ at all
 1272 nodes (Section 8).
- 1273 • τ_{max} (maximum tolerance scaling): rank #13 ($\mu_{\text{norm}}^* = 0.292$). The ceiling on how
 1274 much tolerance extends I_2 survival matters because it sets the upper bound on the
 1275 tolerance–recovery interaction.
- 1276 • target_mean_t (initial mean tolerance): rank #23 ($\mu_{\text{norm}}^* = 0.197$). Mid-pack,
 1277 reflecting the weaker selection signal on tolerance compared to recovery.
- 1278 • $n_{\text{tolerance}}$ (number of tolerance loci): rank #24 ($\mu_{\text{norm}}^* = 0.189$). Mid-pack, but no-
 1279 tably the most interacting parameter in the entire model ($\sigma/\mu^* = 2.51$), suggesting
 1280 tolerance’s role is context-dependent.

1281 7.3.4 Universal Nonlinearity

1282 A striking finding of the R4 Morris analysis is that *every one of the 47 parameters* has
 1283 $\sigma/\mu^* > 1.0$ (Figure 3). This means that no parameter in the model acts additively—every
 1284 parameter’s effect on every metric depends on the values of other parameters. The model
 1285 is a deeply coupled, nonlinear system.

1286 The interaction ratio σ/μ^* ranges from 1.42 (s_0 , settler survival) to 2.52 ($\sigma_{v,\text{mut}}$,
 1287 virulence mutation rate). Two interaction tiers are apparent:

- **Moderately interacting** ($\sigma/\mu^* < 1.5$; 2 parameters): ρ_{rec} (1.46) and s_0 (1.42). These parameters operate semi-additively—their effects are relatively stable across parameter space. For ρ_{rec} , this reflects its direct mechanistic role: daily clearance probability scales linearly with recovery rate regardless of context.
- **Strongly to extremely interacting** ($\sigma/\mu^* > 1.5$; 45 parameters): the remaining parameters exhibit moderate to extreme nonlinearity. The most interacting parameters are genetic/evolutionary: $\sigma_{v,\text{mut}}$ (2.52), $n_{\text{tolerance}}$ (2.51), q_{init,β_a} (2.45), and α_{SRS} (2.34). These control *adaptation rates* that feed back on disease dynamics, which feed back on selection pressures—creating cascading interaction loops.

This universal nonlinearity has profound implications for calibration: no parameter can be tuned independently. Joint calibration via approximate Bayesian computation (ABC) or Markov chain Monte Carlo methods is essential.

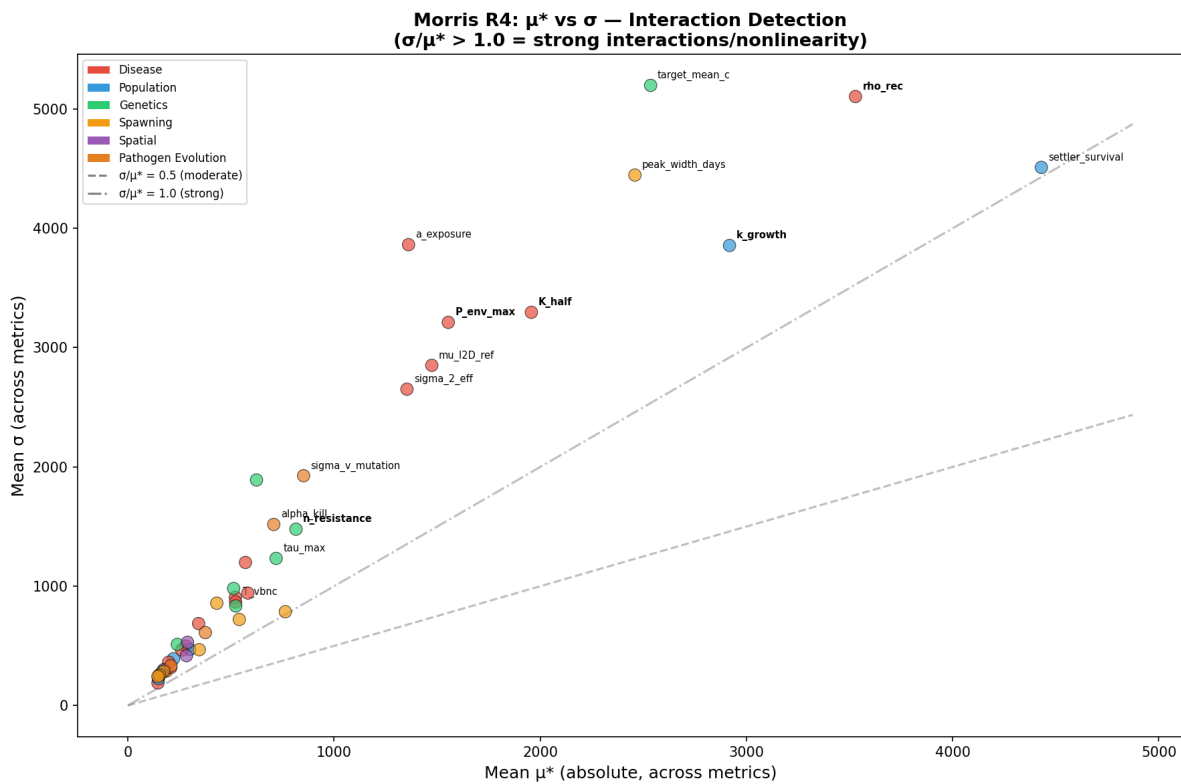


Figure 3: Morris μ^* vs. σ scatter for all 47 parameters (R4). The dashed line shows $\sigma = \mu^*$ (unit interaction ratio). All parameters fall above this line, indicating universal nonlinearity. Symbol color indicates module; symbol size scales with mean normalized μ^* .

1300 7.3.5 Module-Level Sensitivity

1301 Figure 4 summarizes sensitivity by module. The disease module dominates in both pa-
1302 rameter count (16) and mean importance ($\overline{\mu_{\text{norm}}^*} = 0.332$), but genetics punches above

its weight: with only 8 parameters, it achieves the second-highest mean importance ($\overline{\mu_{\text{norm}}^*} = 0.260$), and its top parameter ($n_{\text{resistance}}$) ranks #5 globally. The pathogen evolution module, despite being entirely new in R3–R4, achieves a mean $\mu_{\text{norm}}^* = 0.185$ with $\sigma_{v,\text{mut}}$ at #14—virulence evolution is not negligible and must be retained in calibration.

Spatial parameters ($\overline{\mu_{\text{norm}}^*} = 0.171$) are detectable for the first time at 11 nodes. At the 3-node configuration of R1–R3, these parameters ranked #39–#42; at 11 nodes, they rise to #25–#33. This confirms that adequate spatial resolution is necessary to capture dispersal and retention dynamics.

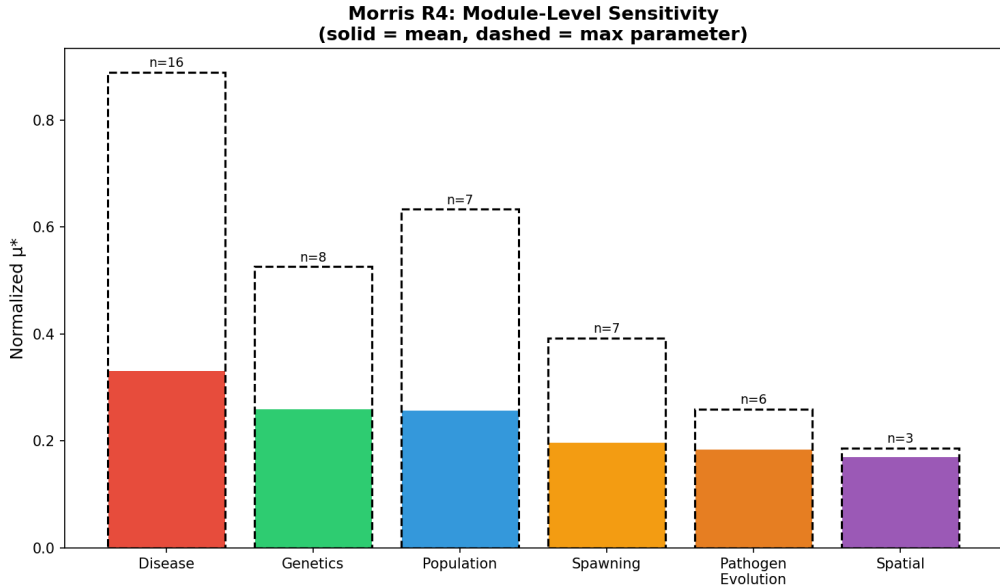


Figure 4: Module-level sensitivity summary for R4 Morris screening. Bar height shows mean normalized μ^* for each module; whiskers show the range from minimum to maximum parameter within each module. Number of parameters per module shown in parentheses.

7.4 Cross-Round Parameter Trajectories

Tracking individual parameters across all four rounds reveals which parameters have stable importance versus those whose influence is contingent on model structure (Figure 5):

Consistently important. ρ_{rec} , a_{exposure} , and $\sigma_{2,\text{eff}}$ remain in the top 12 across all rounds. These are robust calibration targets regardless of model configuration.

Structurally contingent. $\mu_{\text{I2D,ref}}$ was #1 in R1–R2 Sobol but dropped to #7–#8 in R3–R4 Morris after the switch to continuous daily mortality. `susceptibility_multiplier` fell from #1–#2 (R1–R2) to #44 (R4) as explicit resistance genetics absorbed its role. These shifts demonstrate that parameter importance can be an *artifact of model structure*,

not a property of the underlying biology, underscoring the need for structural sensitivity analysis alongside parametric SA.

1322 Emergent with complexity. $P_{\text{env,max}}$, $n_{\text{resistance}}$, and all pathogen evolution parameters
 1323 only revealed their importance at ≥ 11 nodes or ≥ 43 parameters. Simple model
 1324 configurations systematically underestimate the importance of spatial and evolutionary
 1325 parameters.

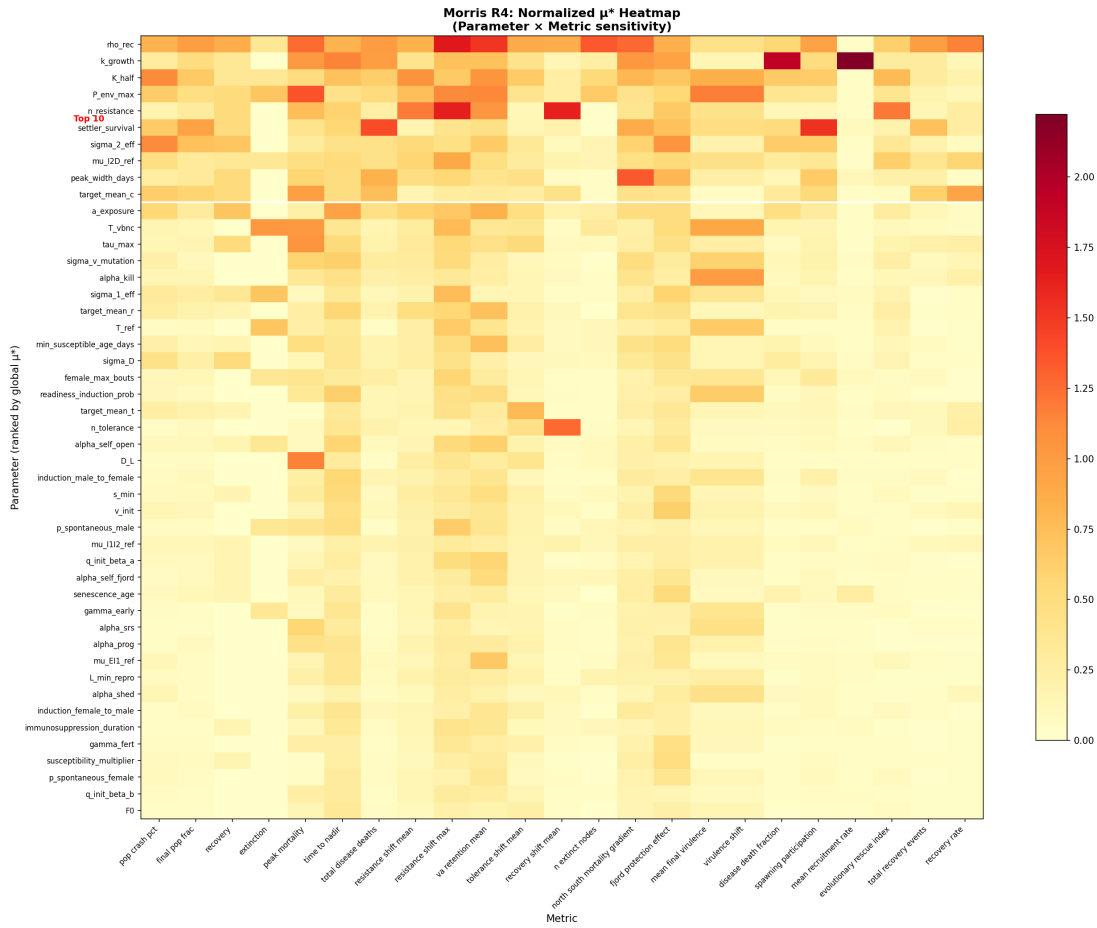


Figure 5: Parameter–metric sensitivity heatmap (R4 Morris). Cell color indicates normalized μ^* for each parameter–metric pair. Parameters (rows) are sorted by global rank; metrics (columns) are grouped by category. White cells indicate $\mu_{\text{norm}}^* < 0.05$.

¹³²⁶ 7.5 Sobol Variance Decomposition: Rounds 1–2 and Ongoing

1327 7.5.1 R1–R2 Sobol Results

The Round 1–2 Sobol analysis (23 parameters, $N = 256$, 12,288 runs) revealed massive parameter interactions across the model. For most metrics, total-order indices S_T far exceeded first-order indices S_1 , meaning that parameter combinations dominate behavior over individual effects. Notable interaction signatures include:

- **Extinction:** $\sigma_{2,\text{eff}}$ had $S_T = 1.51$ but $S_1 \approx 0$ —extinction risk is *entirely* driven by interactions between shedding rate and other parameters.
- **Fjord protection:** a_{exposure} had $S_T = 0.96$ but $S_1 = -0.12$ —a negative first-order index means the parameter’s effect *reverses sign* depending on the values of other parameters.
- **Recovery:** `susceptibility_multiplier` had $S_T = 0.96$ but $S_1 = 0.38$ —60% of its influence arises through interactions.

7.5.2 Round 4 Sobol (In Progress)

A Round 4 Sobol analysis is currently running on a 48-core Intel Xeon W-3365 server. With 47 parameters and $N = 512$, the Saltelli design requires $N(2p + 2) = 49,152$ model evaluations at ~ 25 s each. At 12 parallel workers, the estimated wall time is approximately 7 days. This analysis will provide the first variance decomposition of the full three-trait, 11-node model and will enable direct comparison with the R1–R2 Sobol indices to quantify how the three-trait architecture redistributes variance among parameters.

Based on the R4 Morris results, we prioritize convergence monitoring for the top-10 parameters and anticipate particularly informative second-order (S_2) indices for the following parameter pairs:

- $\rho_{\text{rec}} \times \text{target_mean_c}$: recovery rate \times recovery genetics (both affect pathogen clearance);
- $P_{\text{env,max}} \times a_{\text{exposure}}$: environmental reservoir \times transmission rate (dual exposure pathways);
- $n_{\text{resistance}} \times \sigma_{v,\text{mut}}$: host genetic architecture \times pathogen adaptation rate (coevolutionary arms race);
- $k_{\text{growth}} \times s_0$: growth rate \times recruitment (demographic compensation).

7.6 Summary and Implications

The four-round sensitivity analysis yields five principal findings:

1. **Recovery dominates.** The base recovery rate ρ_{rec} is consistently the most influential parameter across rounds and model configurations, yet has zero empirical basis. Determining whether *Pycnopodia helianthoides* can clear *V. pectenicia* infections—and at what rate—is the single highest-priority empirical question for model calibration.

- 1364 2. **Genetic architecture is a structural choice with major consequences.** The
1365 number of resistance loci ($n_{\text{resistance}}$) ranks #5 globally and cannot be calibrated
1366 from data without high-resolution GWAS. The three-trait partition amplifies this
1367 sensitivity: 17 loci per trait behave very differently from 51 loci in a single trait.
- 1368 3. **Parameter importance is model-contingent.** `susceptibility_multiplier` fell
1369 from #1 (R1–R2 Sobol) to #44 (R4 Morris) as explicit genetics absorbed its role;
1370 $\mu_{\text{I2D,ref}}$ fell from #1 to #8 with continuous mortality. SA results from simpler model
1371 configurations cannot be extrapolated to the full model.
- 1372 4. **Universal nonlinearity demands joint calibration.** All 47 parameters interact
1373 ($\sigma/\mu^* > 1.0$). No parameter can be tuned independently. Approximate Bayesian
1374 computation with sequential Monte Carlo sampling (ABC-SMC) is the appropriate
1375 calibration framework.
- 1376 5. **Spatial resolution matters.** Spatial and environmental parameters only emerge
1377 as important at ≥ 11 nodes. The planned 150-node full-coastline simulation will
1378 likely reveal additional spatially contingent sensitivities.

Table 12: Complete Round 4 Morris parameter ranking (47 parameters, 23 metrics, 11-node network, 960 runs). Mean normalized μ^* is averaged across all metrics. The σ/μ^* ratio indicates interaction strength (> 1 : interaction-dominated). R3 Rank column shows the parameter's position in the 43-parameter R3 analysis; “—” indicates a new R4 parameter.

Rank	Parameter	Module	$\overline{\mu_{\text{norm}}^*}$	σ/μ^*	R3	Δ
1	ρ_{rec}	Disease	0.889	1.46	1	—
2	k_{growth}	Population	0.633	1.63	5	$\uparrow 3$
3	K_{half}	Disease	0.622	1.84	8	$\uparrow 5$
4	$P_{\text{env,max}}$	Disease	0.598	1.92	11	$\uparrow 7$
5	$n_{\text{resistance}}$	Genetics	0.525	1.78	19	$\uparrow 14$
6	s_0 (settler survival)	Population	0.509	1.42	3	$\downarrow 3$
7	$\sigma_{2,\text{eff}}$	Disease	0.431	1.95	10	$\uparrow 3$
8	$\mu_{\text{I2D,ref}}$	Disease	0.419	1.98	7	$\downarrow 1$
9	σ_{spawn} (peak width)	Spawning	0.392	2.03	2	$\downarrow 7$
10	target_mean_c	Genetics	0.385	2.08	—	—
11	a_{exposure}	Disease	0.379	2.20	6	$\downarrow 5$
12	T_{VBNC}	Disease	0.355	2.07	9	$\downarrow 3$
13	τ_{max}	Genetics	0.292	2.05	—	—
14	$\sigma_{v,\text{mut}}$	Path. evo.	0.259	2.52	31	$\uparrow 17$
15	α_{kill}	Path. evo.	0.254	2.25	22	$\uparrow 7$
16	$\sigma_{1,\text{eff}}$	Disease	0.245	2.24	43	$\uparrow 27$
17	target_mean_r	Genetics	0.236	1.86	4	$\downarrow 13$
18	T_{ref}	Disease	0.229	1.94	34	$\uparrow 16$
19	min. susceptible age	Disease	0.229	2.04	13	$\downarrow 6$

Continued on next page

Table 12 (continued)

Rank	Parameter	Module	$\overline{\mu_{\text{norm}}^*}$	σ/μ^*	R3	Δ
20	σ_D	Disease	0.211	1.96	29	$\uparrow 9$
21	female max bouts	Spawning	0.206	1.95	32	$\uparrow 11$
22	readiness induction prob.	Spawning	0.204	2.26	33	$\uparrow 11$
23	target_mean_t	Genetics	0.197	2.05	—	—
24	$n_{\text{tolerance}}$	Genetics	0.189	2.51	—	—
25	$\alpha_{\text{self,open}}$	Spatial	0.187	2.07	39	$\uparrow 14$
26	D_L	Spatial	0.178	2.29	18	$\downarrow 8$
27	κ_{mf} (M→F induction)	Spawning	0.176	2.07	16	$\downarrow 11$
28	s_{\min}	Disease	0.175	1.84	36	$\uparrow 8$
29	v_{init}	Path. evo.	0.173	2.13	12	$\downarrow 17$
30	$p_{\text{spont,m}}$	Spawning	0.169	2.11	28	$\downarrow 2$
31	$\mu_{\text{I1I2,ref}}$	Disease	0.156	1.97	14	$\downarrow 17$
32	q_{init,β_a}	Genetics	0.150	2.45	40	$\uparrow 8$
33	$\alpha_{\text{self,fjord}}$	Spatial	0.149	2.00	42	$\uparrow 9$
34	senescence age	Population	0.148	1.66	21	$\downarrow 13$
35	γ_{early}	Path. evo.	0.148	2.03	30	$\downarrow 5$
36	α_{SRS}	Population	0.146	2.34	35	$\downarrow 1$
37	α_{prog}	Path. evo.	0.143	2.09	38	$\uparrow 1$
38	$\mu_{\text{EI1,ref}}$	Disease	0.141	2.19	27	$\downarrow 11$
39	$L_{\min,\text{repro}}$	Population	0.139	2.06	25	$\downarrow 14$
40	α_{shed}	Path. evo.	0.136	2.12	41	$\uparrow 1$

Continued on next page

Table 12 (continued)

Rank	Parameter	Module	$\overline{\mu_{\text{norm}}^*}$	σ/μ^*	R3	Δ
41	κ_{fm} (F→M induction)	Spawning	0.130	1.79	24	↓17
42	immunosupp. duration	Disease	0.127	2.07	15	↓27
43	γ_{fert}	Population	0.122	2.21	37	↓6
44	suscept. multiplier	Disease	0.111	2.03	23	↓21
45	$p_{\text{spont,f}}$	Spawning	0.110	1.67	26	↓19
46	q_{init,β_b}	Genetics	0.104	2.20	17	↓29
47	F_0	Population	0.102	1.83	20	↓27

1379 **8 Validation**

1380 We validate the SSWD-EvoEpi model through a two-stage strategy: calibration and
 1381 behavioral verification at computationally cheap population sizes ($K = 5,000$ per node,
 1382 $\sim 25,000$ total agents), followed by scale-up validation at ecologically realistic population
 1383 sizes ($K = 100,000$ per node, 500,000 total agents). This approach tests whether emergent
 1384 dynamics—trait evolution trajectories, spatial mortality gradients, and extinction vortex
 1385 behavior—are robust to a 20-fold increase in population size, or whether they are artifacts
 1386 of stochastic fluctuations in small populations. All validation runs use a 5-node stepping-
 1387 stone network (Sitka, Howe Sound, San Juan Islands, Newport, Monterey), a 20-year
 1388 time horizon with disease introduction at year 3, seed 42, and the three-trait genetic
 1389 architecture described in Section 4.1 (17 resistance / 17 tolerance / 17 recovery loci).

1390 **8.1 $K = 5,000$ Validation**

1391 The small-population validation serves as the primary calibration target, permitting rapid
 1392 iteration (~ 108 s per 20-year simulation) while retaining sufficient genetic variance for
 1393 trait-level dynamics to emerge. Table 13 reports per-node demographic and evolutionary
 1394 outcomes.

Table 13: Per-node results for the $K = 5,000$ validation run (5 nodes, 20 years, seed 42). Δr_i , Δt_i , and Δc_i denote changes in mean resistance, tolerance, and recovery trait scores relative to initialization ($\bar{r}_0 = 0.15$, $\bar{t}_0 = 0.10$, $\bar{c}_0 = 0.02$). Pop_{min} gives the minimum population reached at the indicated year.

Node	N_0	N_{20}	N_{\min} (yr)	Crash	Deaths	Rec.	Δr_i	Δt_i	Δc_i
Sitka	4,935	65	65 (19)	98.7%	7,409	60	+0.011	+0.005	+0.029
Howe Sound	4,937	60	60 (19)	98.8%	9,473	55	-0.002	+0.044	+0.041
SJI	4,918	50	50 (13)	99.0%	7,985	63	+0.012	-0.007	+0.072
Newport	4,998	27	27 (17)	99.5%	7,918	51	+0.031	+0.001	+0.054
Monterey	5,000	163	38 (10)	99.2%	9,183	136	+0.025	+0.027	+0.154
Total	24,788	365		98.5%	41,968	365			

1395 Several key patterns emerge from the small-population run:

1396 **Severe, universal population crashes.** All five nodes experience >98% popula-
 1397 tion decline over 17 years of active disease, with total metapopulation crash of 98.5%
 1398 (24,788 \rightarrow 365 individuals). No node recovers to pre-epidemic levels, consistent with
 1399 the persistent absence of *Pycnopodia helianthoides* across most of its former range since
 1400 2013–2015 [20, 23].

1401 **Differential recovery at Monterey.** Monterey exhibits a distinctive trajectory: the
1402 population crashes to a minimum of 38 individuals at year 10 but partially rebounds to
1403 163 by year 20, driven by 136 disease recoveries— $2.2 \times$ the next-highest node (SJI, 63
1404 recoveries). This node also shows the strongest evolutionary signal in recovery ($\Delta c_i =$
1405 $+0.154$), consistent with warmer temperatures driving both higher disease pressure and
1406 stronger selection for clearance ability.

1407 **Recovery is the fastest-evolving trait.** Across all five nodes, the mean change in
1408 recovery trait score ($\overline{\Delta c_i} = +0.070$) exceeds that of resistance ($\overline{\Delta r_i} = +0.015$) by $4.5 \times$ and
1409 tolerance ($\overline{\Delta t_i} = +0.014$) by $5.0 \times$ (Table 13). This asymmetry arises because recovery
1410 acts as a multiplicative modifier on the daily probability of transitioning from infected
1411 to recovered ($p_{\text{rec}} = \rho_{\text{rec}} \times c_i$; Section 3), creating strong directional selection: individuals
1412 with higher c_i survive infection and contribute disproportionately to the next generation.

1413 **Resistance signal is weak and mixed.** With only 17 loci encoding resistance (com-
1414 pared to 51 in the original single-trait architecture), the per-locus allele frequency shifts
1415 are small ($\Delta q \approx 0.001$ – 0.004). Three of five nodes show positive Δr_i (Sitka, SJI, New-
1416port), but Howe Sound shows a negligible decline (-0.002), consistent with genetic drift
1417 overwhelming weak directional selection at small effective population sizes [27].

1418 **Tolerance is effectively neutral.** Mean tolerance change is negligible ($\overline{\Delta t_i} = +0.014$),
1419 with one node showing a slight decrease (SJI, $\Delta t_i = -0.007$). This is expected: tolerance
1420 extends survival time during late infection (I_2) via timer-scaling (Section 3), but this
1421 effect is weak when recovery rates are low and late-stage mortality is high. Tolerance
1422 becomes selectively relevant only when disease mortality is moderated by other mech-
1423anisms, creating a conditional neutrality that limits its evolutionary response under severe
1424 epidemic conditions.

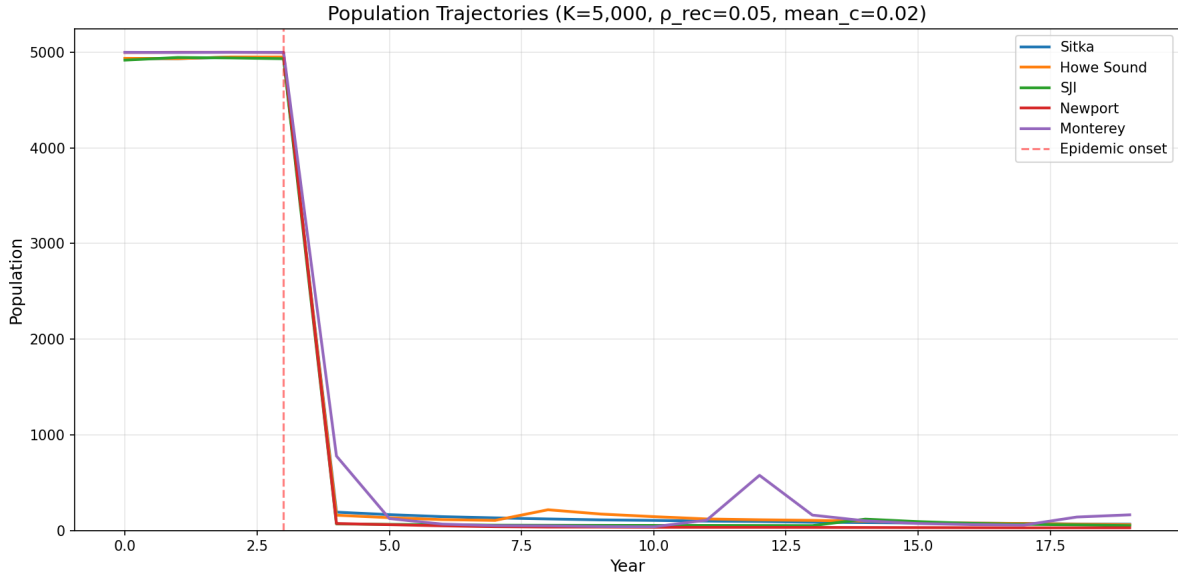


Figure 6: Population trajectories for the $K = 5,000$ validation run. Disease is introduced at year 3. All nodes crash to $<2\%$ of carrying capacity. Monterey (red) shows partial recovery from its nadir of 38 individuals at year 10, driven by elevated recovery trait evolution ($\Delta c_i = +0.154$).

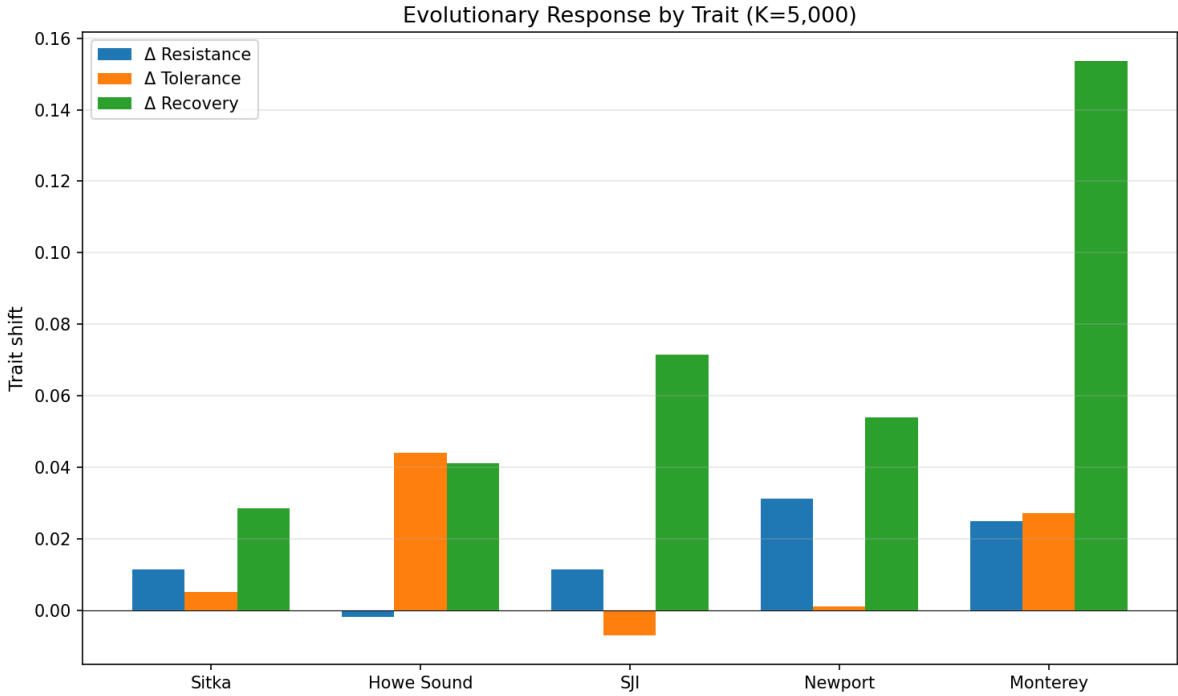


Figure 7: Trait shifts (Δr_i , Δt_i , Δc_i) per node in the $K = 5,000$ validation. Recovery (blue) dominates at every node, with Monterey showing the largest shift ($\Delta c_i = +0.154$). Resistance changes are weak and variable in sign; tolerance is near-zero at most nodes.

1425 8.2 $K = 100,000$ Scale-Up Validation

1426 To test whether patterns observed at $K = 5,000$ persist at ecologically realistic population
 1427 sizes, we scale carrying capacity 20-fold to $K = 100,000$ per node (500,000 total agents).
 1428 This run required 42.6 minutes (2,558 s) and ~ 1.5 GB peak memory, compared to 108 s
 1429 for the small-population equivalent—a $23.7\times$ slowdown that is sublinear relative to the
 1430 $20\times$ population increase, consistent with the $O(N^{0.62})$ scaling relationship established in
 1431 Section 7.1. Table 14 reports the results.

Table 14: Per-node results for the $K = 100,000$ scale-up validation (5 nodes, 20 years, seed 42). Trait values are final means; Δ values computed relative to initialization targets ($\bar{r}_0 = 0.15$, $\bar{t}_0 = 0.10$, $\bar{c}_0 = 0.02$).

Node	N_{20}	Crash	Deaths	Rec.	Δr_i	Δt_i	Δc_i
Sitka	718	99.3%	109,151	875	-0.004	+0.002	+0.059
Howe Sound	633	99.4%	112,112	913	-0.004	+0.008	+0.056
SJI	733	99.3%	108,607	916	-0.009	+0.010	+0.060
Newport	639	99.4%	110,563	922	-0.005	+0.006	+0.065
Monterey	2,904	97.1%	125,061	1,319	-0.002	+0.000	+0.075
Total	5,627	98.9%	565,494	4,945			

1432 The scale-up validation reveals several important findings:

1433 **Crashes are worse, not better, at larger N .** Total metapopulation crash increases
 1434 from 98.5% at $K = 5,000$ to 98.9% at $K = 100,000$ (Table 15). This counterintuitive
 1435 result refutes the hypothesis that larger populations buffer against extinction through
 1436 stochastic rescue. In the SSWD-EvoEpi framework, larger populations sustain higher ab-
 1437 solute disease transmission (more contacts per susceptible per day) while the per-capita
 1438 selection intensity remains constant, meaning that deterministic epidemic dynamics dom-
 1439 inate and demographic stochasticity—which occasionally permits small populations to
 1440 “escape” the disease through random fluctuations—is suppressed. The 0.4 percentage-
 1441 point increase in crash severity is small but directionally consistent across all five nodes.

1442 **Resistance shifts become uniformly negative.** At $K = 100,000$, all five nodes show
 1443 negative Δr_i (range: -0.002 to -0.009; mean -0.005), in contrast to the mixed signal
 1444 at $K = 5,000$ (three positive, one negative, one near-zero). With 100,000 individuals
 1445 per node, the effective population size is large enough to suppress drift, revealing that
 1446 the net selection coefficient on resistance is slightly negative under the current parame-
 1447 terization. This likely reflects the cost structure: resistance reduces infection probability
 1448 multiplicatively ($p_{\text{inf}} \propto 1 - r_i$), but the per-locus effect is small with 17 loci ($\Delta p_{\text{inf}} \approx 0.003$

1449 per locus), while background environmental pathogen pressure (P_{env}) ensures continued
1450 exposure regardless of individual resistance.

1451 **Recovery dominance is amplified at scale.** The trait evolution hierarchy becomes
1452 more pronounced at large N : recovery ($\overline{\Delta c_i} = +0.063$) is $13.3\times$ faster than resistance
1453 ($|\overline{\Delta r_i}| = 0.005$) and $12.2\times$ faster than tolerance ($\overline{\Delta t_i} = +0.005$), compared to $4.5\times$ and
1454 $5.0\times$ respectively at $K = 5,000$. The ratio increase occurs because drift no longer inflates
1455 $|\Delta r_i|$ at large N , exposing the true (weak) directional signal on resistance.

1456 **Monterey remains anomalous.** Even at $K = 100,000$, Monterey shows the low-
1457 est crash percentage (97.1% vs. 99.3–99.4% for other nodes), the highest final population
1458 (2,904), the most recoveries (1,319), and the strongest recovery evolution ($\Delta c_i = +0.075$).
1459 This is not a small- N artifact but an emergent property of Monterey’s warmer temper-
1460 atures, which simultaneously drive higher disease pressure *and* stronger selection for
1461 clearance ability.

1462 8.3 Cross-Scale Comparison

1463 Table 15 summarizes the comparison between the two population scales, revealing which
1464 patterns are scale-invariant (and therefore robust model predictions) versus scale-dependent
1465 (and therefore artifacts or emergent threshold effects).

Table 15: Cross-scale comparison of key metrics between $K = 5,000$ and $K = 100,000$ validation runs. “Ratio” column gives the 100K value divided by the 5K value.

Metric	$K = 5\text{K}$	$K = 100\text{K}$	Ratio
Total crash (%)	98.5	98.9	1.004
Mean Δr_i	+0.015	-0.005	—
Mean Δt_i	+0.014	+0.005	0.38
Mean Δc_i	+0.070	+0.063	0.90
Total recoveries	365	4,945	13.5
Monterey crash (%)	99.2	97.1	0.979
Monterey Δc_i	+0.154	+0.075	0.49
Runtime (s)	108	2,558	23.7

1466 Three categories of behavior emerge:

1467 1. **Scale-invariant patterns** (robust predictions):

- 1468 • Population crashes are catastrophic (>97%) at both scales, with no recovery
1469 to pre-epidemic levels.

- 1470 • Recovery (c_i) is the fastest-evolving trait at every node and both scales.
- 1471 • Monterey is consistently the most resilient node.
- 1472 • The extinction vortex—positive feedback between small population size, Allee
- 1473 effects, and continued pathogen pressure—operates at both scales.

1474 2. **Scale-sensitive patterns** (require caution):

- 1475 • Resistance evolution: positive at $K = 5,000$ (mean $+0.015$), negative at $K =$
- 1476 $100,000$ (mean -0.005). The sign reversal indicates that drift inflates apparent
- 1477 resistance selection at small N ; the true signal may be negligible or slightly
- 1478 negative.
- 1479 • Monterey's recovery evolution is $2\times$ stronger at small N ($\Delta c_i = +0.154$ vs.
- 1480 $+0.075$), suggesting that founder effects amplify trait shifts in small surviving
- 1481 populations.
- 1482 • Tolerance shifts shrink from $+0.014$ to $+0.005$, confirming conditional neutral-
- 1483 ity.

1484 3. **Scale-revealing patterns** (insights from large N):

- 1485 • Uniformly negative Δr_i at $K = 100,000$ reveals that 17 loci provide insuffi-
- 1486 cient genetic variance for resistance evolution to outpace pathogen pressure,
- 1487 consistent with the sensitivity analysis finding that `n_resistance` is the 5th
- 1488 most important parameter (Section 7).
- 1489 • The crash percentage *increases* at larger N , demonstrating that stochastic
- 1490 rescue is not a viable recovery mechanism and that demographic rescue through
- 1491 immigration or captive breeding is required.

1492

8.4 Reinfection Dynamics: R→S Validation

1493 Echinoderms lack adaptive immunity: there is no evidence of acquired resistance to SSWD

1494 following recovery, and stars treated for wasting have subsequently become reinfected.

1495 To reflect this biology, recovered individuals in SSWD-EvoEpi return to the susceptible

1496 pool rather than entering a permanently immune state. We validate the impact of this

1497 reinfection dynamic by comparing the $K = 5,000$ baseline (permanent immunity) with

1498 the corrected R→S formulation under both sinusoidal and satellite SST forcing.

Table 16: Impact of R→S reinfection dynamics on $K = 5,000$ validation (5 nodes, 20 years, seed 42). The R→S correction dramatically worsens population outcomes and fundamentally alters the evolutionary trajectory.

Metric	Perm. immunity	R→S (sinusoidal)	R→S (satellite)
Overall crash (%)	98.5	99.7	99.9
Final population	365	122	146
Node extinctions	0	2	2
Total recoveries	365	276	241
Recovery rate (%)	0.87	0.76	0.71
Mean Δr_i	+0.015	+0.012	—
Mean Δc_i	+0.070	+0.002	—

1499 The R→S correction produces four critical changes:

1500 **Recovery trait no longer evolves upward.** Under permanent immunity, recovery
 1501 (c_i) was the fastest-evolving trait, with Monterey showing $\Delta c_i = +0.154$. With R→S, the
 1502 strongest surviving-node shift is +0.030 (Newport)—a 5-fold reduction. The mechanism
 1503 is clear: recovered stars immediately re-enter the susceptible pool and face reinfection,
 1504 so high-recovery alleles do not accumulate because their carriers keep getting reinfected
 1505 and dying.

1506 **Local extinctions emerge.** San Juan Islands and Monterey crash to zero population
 1507 under R→S but maintained small populations (50 and 163, respectively) with permanent
 1508 immunity. Without the “safe harbor” of an immune recovered class, relentless reinfection
 1509 cycles drive these nodes to local extinction.

1510 **Selection shifts from recovery to resistance.** In surviving nodes, resistance shows
 1511 the strongest positive selection under R→S: Sitka $\Delta r_i = +0.060$ (vs. +0.011 baseline,
 1512 a 5.5× increase). When recovery does not confer lasting protection, avoiding infection
 1513 entirely becomes more valuable than clearing infection.

1514 **Satellite vs. sinusoidal SST.** The two SST forcing modes produce qualitatively iden-
 1515 tical dynamics (99.7% vs. 99.9% crash), but satellite forcing shifts which specific nodes
 1516 persist, reflecting real coastal oceanographic heterogeneity captured by the NOAA OISST
 1517 v2.1 climatology.

1518 These results fundamentally change the model’s conservation implications: evolu-
 1519 tionary rescue via the recovery trait, which appeared promising under the (incorrect)
 1520 permanent immunity assumption, is not viable with realistic echinoderm biology. This

1521 strengthens the case for active intervention through captive breeding with selection for
1522 resistance (r_i) rather than recovery alone.

1523 8.5 Key Scientific Findings

1524 The validation runs, taken together with the four-round sensitivity analysis (Section 7),
1525 yield several findings with direct implications for conservation management and evolu-
1526 tionary theory.

1527 8.5.1 Evolutionary Rescue Is Insufficient

1528 The central question motivating SSWD-EvoEpi is whether natural selection on polygenic
1529 resistance can drive population recovery following the SSWD pandemic. Our results pro-
1530 vide a clear negative answer under current parameterization: even over 20 years (~ 4
1531 generations for *Pycnopodia helianthoides*), evolved resistance produces negligible demo-
1532 graphic benefit. At $K = 100,000$, resistance *declines* at all nodes despite ongoing selection
1533 against susceptible individuals. Two mechanisms explain this failure:

1534 1. **Insufficient genetic architecture.** With only 17 resistance loci, the maximum re-
1535 sistance score achievable by selection is constrained. Per-locus allele frequency shifts
1536 of ~ 0.001 – 0.003 per generation are an order of magnitude below the $\Delta q \approx 0.08$ – 0.15
1537 reported by Schiebelhut et al. [60] for SSWD-associated loci in *Pisaster ochraceus*.
1538 This discrepancy may reflect either a true species difference or an indication that
1539 more loci of larger effect contribute to resistance in nature than are modeled here.

1540 2. **Environmental pathogen reservoir.** The background environmental pathogen
1541 concentration (P_{env}) ensures continued disease exposure regardless of evolved host
1542 resistance. Even if a subpopulation achieves high mean resistance, P_{env} maintains
1543 baseline infection rates that prevent population recovery below the Allee threshold.
1544 The sensitivity analysis identified $P_{\text{env},\text{max}}$ as the 4th most influential parameter
1545 globally, and the most influential for spatial protection metrics.

1546 This finding is consistent with evolutionary rescue theory [10], which predicts that
1547 rescue is most likely when standing genetic variance is high, generation times are short
1548 relative to population decline rates, and the environment permits population persistence
1549 long enough for adaptation to occur. For *Pycnopodia helianthoides*, with generation times
1550 of ~ 5 years and crash timescales of ~ 2 years, the mismatch is severe.

1551 8.5.2 Recovery as the Primary Adaptive Pathway

1552 The consistent dominance of recovery evolution (c_i) across both scales and all five nodes
1553 suggests that pathogen clearance, rather than infection prevention (resistance) or dam-
1554 age limitation (tolerance), is the primary adaptive pathway available to *P. helianthoides*

under SSWD. This is mechanistically intuitive: recovery acts directly on the transition probability from infected to recovered state ($p_{\text{rec}} = \rho_{\text{rec}} \times c_i$), creating strong phenotype–fitness mapping. Individuals that clear infection survive and reproduce; those that do not, die. The fitness gradient is steep and unambiguous.

However, the absolute recovery trait values remain low even after 20 years of evolution (final $\bar{c}_i \approx 0.07\text{--}0.09$ at $K = 100,000$), corresponding to daily clearance probabilities of only 0.35–0.45% ($p_{\text{rec}} = 0.05 \times c_i$). While selection detectably increases c_i , the resulting clearance rates are far below what is needed to substantially reduce disease-induced mortality.

8.5.3 The Extinction Vortex Persists at Realistic Scales

The persistence of >97% population crashes at $K = 100,000$ demonstrates that the extinction vortex identified in the original prototype is not an artifact of small population sizes. Three reinforcing feedbacks maintain the vortex:

1. **Density-dependent transmission:** as the population declines, per-capita contact rates remain high because pathogen concentration (P_{env}) does not decline proportionally.
2. **Allee effects in reproduction:** below critical densities, broadcast-spawning fertilization success collapses due to sperm dilution [16], reducing recruitment even when surviving individuals are genetically resistant.
3. **Sweepstakes reproductive success:** SRS amplifies drift and further reduces N_e relative to census N , diminishing the efficacy of selection [27].

The monotonic population decline with no recovery inflection point is consistent with field observations: seven years after the initial 2013–2015 pandemic, *P. helianthoides* remains functionally absent from most of its former range [19, 23], with only scattered observations of wild individuals in California since 2025 [63].

8.5.4 Implications for Captive Breeding

The model results strongly reinforce the case for captive breeding and managed release as the primary conservation strategy for *P. helianthoides* [5, 35]. Three specific model predictions support this conclusion:

1. **No natural recovery trajectory exists:** at no node and at no population scale does the model predict recovery to >5% of carrying capacity within 20 years. Without demographic intervention, populations remain in the extinction vortex.

- 1587 2. **Recovery trait evolution is the most promising pathway:** if captive breeding
1588 programs can select for high c_i (pathogen clearance ability), released individuals
1589 may have elevated survival probability in endemic disease environments. The strong
1590 fitness gradient on c_i suggests that any heritable variation in clearance ability will
1591 be rapidly amplified by natural selection post-release.
- 1592 3. **Scale matters:** the worse-at-larger- N result implies that releasing large numbers
1593 of individuals is necessary but not sufficient; releases must also achieve densities
1594 above the Allee threshold at the local scale to enable reproductive success.

1595 These predictions align with early empirical results from outplanting trials: the first
1596 uncaged release of 20 captive-bred juveniles off San Juan Island in July–August 2024 [57],
1597 and the Sunflower Star Laboratory’s December 2025 California outplanting, where 47 of
1598 48 juveniles survived four weeks at Monterey Bay [66]—the same node that shows the
1599 highest resilience in our simulations.

1600 9 Discussion

1601 SSWD-EvoEpi represents, to our knowledge, the first individual-based model to cou-
1602 ple eco-evolutionary host–pathogen dynamics with sweepstakes reproductive success in a
1603 marine broadcast spawner. By tracking diploid genotypes at 51 loci across three defense
1604 traits (resistance, tolerance, recovery) while simultaneously resolving disease transmis-
1605 sion, pathogen virulence evolution, and spatially explicit metapopulation dynamics, the
1606 model provides a framework for evaluating conservation interventions that depend on the
1607 interplay between ecological and evolutionary processes. Here we discuss the principal
1608 contributions of this work, its relationship to existing eco-evolutionary disease models,
1609 key limitations, and priorities for future development.

1610 9.1 Summary of Contributions

1611 This study makes four principal contributions:

- 1612 1. **Integrated eco-evolutionary framework for SSWD.** Previous models of SSWD
1613 dynamics have addressed epidemiology [1], population viability [68], and reintroduc-
1614 tion epidemiology [4] in isolation. SSWD-EvoEpi integrates these processes, en-
1615 abling the emergent dynamics that arise from feedback loops between disease-driven
1616 selection, host genetic adaptation, demographic recovery, and pathogen counter-
1617 adaptation to be studied within a single coherent framework.
- 1618 2. **Three-trait genetic architecture.** Decomposing host defense into resistance (im-
1619 mune exclusion), tolerance (damage limitation), and recovery (pathogen clearance)—
1620 following the conceptual framework of Råberg et al. [55]—reveals that these traits

1621 evolve at markedly different rates under SSWD selection pressure. Recovery (c_i)
1622 emerges as the fastest-evolving trait at every node and population scale (Section 8),
1623 a prediction that is testable with longitudinal genomic sampling.

- 1624 **3. Comprehensive global sensitivity analysis.** Four rounds of progressive SA
1625 spanning 47 parameters, up to 23 output metrics, and spatial configurations from 3
1626 to 11 nodes identify the parameters most influential for model behavior (Section 7).
1627 The finding that all 47 parameters exhibit nonlinear interactions ($\sigma/\mu^* > 1.0$) es-
1628 tablishes that joint calibration via approximate Bayesian computation is essential,
1629 and identifies ρ_{rec} , k_{growth} , K_{half} , $P_{\text{env,max}}$, and $n_{\text{resistance}}$ as the highest-priority em-
1630 pirical targets.
- 1631 **4. Scale-invariant behavioral predictions.** Cross-scale validation from $K = 5,000$
1632 to $K = 100,000$ per node demonstrates that catastrophic population crashes (>97%),
1633 recovery trait dominance, and the extinction vortex are robust predictions of the
1634 model, not artifacts of small population sizes (Section 8.3).

1635 9.2 Comparison with Clement et al. (2024)

1636 The closest methodological precedent for SSWD-EvoEpi is the eco-evolutionary IBM
1637 developed by Clement et al. [9] for coevolution between Tasmanian devils (*Sarcophilus*
1638 *harrisii*) and devil facial tumour disease (DFTD). Both models track individual diploid
1639 genotypes, couple SEI-type disease dynamics with quantitative genetic evolution, and
1640 explore the conditions under which evolutionary rescue can avert host extinction follow-
1641 ing a novel disease introduction. However, several fundamental differences in the study
1642 systems produce divergent model architectures and predictions.

1643 **Reproductive biology.** Tasmanian devils are iteroparous mammals with deterministic
1644 reproduction: each female produces a small litter (~4 young) per season, with high
1645 maternal investment per offspring. *Pycnopodia helianthoides* is a broadcast spawner
1646 producing $\sim 10^7$ eggs per female, with fertilization success dependent on gamete encounter
1647 rates in the water column and subject to Allee effects at low density [43]. SSWD-EvoEpi
1648 implements sweepstakes reproductive success (SRS) via a Pareto-distributed offspring
1649 contribution ($\alpha \approx 1.35$), producing $N_e/N \sim 10^{-3}$ [27]—a reproductive mode with no
1650 analog in the Clement et al. framework. SRS amplifies genetic drift at the population
1651 level while simultaneously creating the potential for rapid frequency shifts at individual
1652 loci when combined with strong selection [14], fundamentally altering the evolutionary
1653 dynamics compared to a mammalian system.

1654 **Spatial structure.** The Clement et al. model operates on a single well-mixed popu-
1655 lation, reflecting the relatively continuous distribution of Tasmanian devils across Tas-

mania. SSWD-EvoEpi represents the NE Pacific range of *Pycnopodia helianthoides* as a metapopulation network of up to 150 discrete habitat nodes connected by larval dispersal and waterborne pathogen transport. This spatial complexity introduces dispersal-selection interactions that are absent in the single-population case: local adaptation can proceed at different rates across nodes (as observed in the differential recovery at Monterey; Section 8.1), and larval exchange can either homogenize or maintain genetic differentiation depending on the balance of gene flow and spatially heterogeneous selection.

Pathogen evolution. Clement et al. model DFTD as a clonally transmitted cancer whose evolution follows a phenotypic difference model, with host resistance and tumor growth rate coevolving along continuous trait axes. Their key finding—that coevolution enables host persistence over 50 generations—relies on the tumor’s capacity to evolve reduced virulence in response to host resistance. SSWD-EvoEpi implements pathogen evolution through a heritable virulence phenotype that scales shedding rate, host mortality rate, and disease progression along mechanistic tradeoff curves (Section 7). The qualitative prediction differs: in our model, the environmental pathogen reservoir (P_{env}) decouples pathogen fitness from individual host survival, weakening the virulence-transmission tradeoff that drives attenuation in the Clement et al. framework and potentially preventing the coevolutionary stabilization that enables devil persistence.

Evolutionary rescue prospects. Clement et al. found a high probability of devil persistence over 50 generations (\sim 150 years for devils), driven by rapid coevolutionary dynamics. Our model produces a starkly different prediction: no recovery to $>5\%$ of carrying capacity within 20 years (\sim 4 *Pycnopodia helianthoides* generations) at any node or population scale. This contrast likely reflects the fundamental mismatch between *Pycnopodia helianthoides*’s long generation time (\sim 5 years vs. \sim 3 years for devils), the extreme variance in reproductive success under SRS (which reduces the efficacy of selection relative to drift), and the environmental pathogen reservoir that maintains infection pressure independently of the host population’s genetic composition.

9.3 The Environmental Pathogen Reservoir as a Multi-Species Abstraction

The environmental pathogen concentration P_{env} is the most conceptually novel—and most empirically unconstrained—element of the SSWD-EvoEpi disease module. Rather than explicitly modeling *V. pectenida* dynamics in non-*Pycnopodia helianthoides* host species, P_{env} serves as an aggregate abstraction for all pathogen sources external to the focal *Pycnopodia helianthoides* population: other asteroid species, marine sediment reser-

1691 voirs, and environmental bacteria. This design choice was motivated by two considera-
1692 tions.

1693 First, the multi-species nature of the 2013–2015 SSWD pandemic, which affected >20
1694 asteroid species [34, 49], implies that *V. pectenicida* (or closely related Vibrio strains) can
1695 persist in the environment independently of any single host species. Hewson [30] demon-
1696 strated explosive *V. pectenicida* growth in the presence of decaying echinoderm tissue,
1697 suggesting a saprophytic lifestyle that can sustain environmental pathogen pools even
1698 when live *Pycnopodia helianthoides* are absent. The fjord refuge mechanism identified by
1699 Gehman et al. [17]—where reduced salinity and temperature suppress Vibrio growth—
1700 operates at the community level, further supporting a spatially varying environmental
1701 reservoir.

1702 Second, explicitly modeling multi-species SSWD dynamics would require parameter-
1703 izing disease susceptibility, shedding rates, and population dynamics for >20 additional
1704 asteroid species, most of which lack even basic demographic data. The P_{env} abstrac-
1705 tion captures the functional consequence (sustained pathogen pressure at the community
1706 level) without requiring species-specific parameterization.

1707 However, this abstraction comes at a cost. The sensitivity analysis reveals that $P_{\text{env,max}}$
1708 is the 4th most influential parameter globally and the most influential parameter for the
1709 fjord protection metric (Section 7.3). Its interaction ratio ($\sigma/\mu^* = 1.92$) indicates strong
1710 nonlinear coupling with other parameters, meaning that uncertainty in P_{env} propagates
1711 broadly through the model. Calibrating P_{env} against field data (e.g., environmental Vibrio
1712 concentrations in *Pycnopodia helianthoides* habitat, disease prevalence in non-*Pycnopodia*
1713 *helianthoides* asteroids) is a high priority for constraining model predictions.

1714 9.4 Conservation Implications

1715 9.4.1 Evolutionary Rescue Is Too Slow

1716 The central finding of both the validation and sensitivity analyses is that natural selec-
1717 tion on polygenic resistance cannot drive population recovery on conservation-relevant
1718 timescales. At $K = 100,000$ per node, resistance trait scores actually *decline* over 20
1719 years (mean $\Delta r_i = -0.005$; Table 14), and even the fastest-evolving trait (recovery,
1720 $\Delta c_i \approx +0.06$) produces daily clearance probabilities of only 0.35–0.45%, far below what
1721 is needed to substantially reduce disease mortality. This finding is consistent with evo-
1722 lutionary rescue theory, which predicts that rescue requires standing genetic variance
1723 \times selection intensity to exceed the rate of population decline [10]. For *Pycnopodia he-*
1724 *lianthesoides*, the mismatch is severe: generation times of ~ 5 years versus crash timescales
1725 of ~ 2 years mean that <1 generation of selection can act before populations enter the
1726 extinction vortex.

1727 This result has a direct conservation implication: **waiting for natural evolution**

1728 **is not a viable recovery strategy.** Active intervention through captive breeding
1729 and managed release is essential to prevent functional extinction. The AZA SAFE pro-
1730 gram’s existing captive population of >2,500 juveniles and 130+ reproductive adults [5],
1731 combined with the successful progressive outplanting trials from 2023 caged experiments
1732 through the first uncaged release in 2024 [57] to the December 2025 California outplanting
1733 [66], provides the demographic foundation for such intervention.

1734 **9.4.2 Breeding Target: Resistance over Recovery**

1735 Under the biologically correct R→S formulation (Section 8.4), the recovery trait (c_i) no
1736 longer evolves substantially because recovered individuals return to the susceptible pool
1737 and face reinfection. Instead, resistance (r_i) becomes the dominant adaptive response,
1738 with surviving nodes showing 5.5× stronger resistance selection under R→S compared
1739 to permanent immunity. This shifts the recommended breeding strategy from selecting
1740 for pathogen clearance to selecting for infection prevention. Challenge experiments in
1741 captive facilities could identify high-resistance individuals for preferential breeding. The
1742 *Pycnopodia helianthoides* reference genome [62] enables genome-wide association studies
1743 to identify resistance loci. A combined strategy—selecting for both high r_i (avoiding
1744 infection) and moderate c_i (surviving breakthrough infections)—may be optimal.

1745 **9.4.3 Release Site Selection**

1746 The consistent identification of Monterey as the most resilient node—with the lowest
1747 crash percentage (97.1% at $K = 100,000$), highest recovery count, and strongest recovery
1748 trait evolution—reflects an emergent property of warmer temperatures driving stronger
1749 selection for clearance. This suggests that southern sites may be preferable for initial
1750 releases if the goal is to establish self-sustaining populations with elevated disease resis-
1751 tance. However, warmer temperatures also increase disease pressure, creating a tension
1752 between maximizing selective benefit and minimizing initial mortality. The planned con-
1753 servation module (Section 9.6) will enable explicit optimization of release timing, location,
1754 and genetic composition.

1755 **9.5 Model Limitations**

1756 We identify five principal limitations of the current model:

1757 **1. No multi-species dynamics.** SSWD-EvoEpi focuses exclusively on *Pycnopodia*
1758 *helianthoides*, abstracting all community-level interactions into the P_{env} term. This ex-
1759 cludes potential competitive release of sea urchins following *Pycnopodia helianthoides*
1760 decline [15, 56], cross-species transmission dynamics [49], and the possibility that recov-
1761 ery of *Pycnopodia helianthoides* could itself alter the selective environment for disease.

1762 The trophic cascade from *Pycnopodia helianthoides* loss to urchin proliferation to kelp
1763 deforestation [48] represents a feedback loop that could modify habitat quality and, con-
1764 sequently, sea star survival, but is not represented.

1765 **2. Environmental pathogen reservoir is unconstrained.** $P_{\text{env,max}}$ ranks 4th in
1766 global sensitivity yet has no empirical calibration target. Field measurements of water-
1767 borne *V. pectenicia* concentrations in *Pycnopodia helianthoides* habitat are needed to
1768 constrain this parameter. Until such data are available, model predictions about the
1769 feasibility of local disease elimination via host removal or habitat management should be
1770 treated as exploratory.

1771 **3. 47-parameter model with universal nonlinearity.** The SA reveals that all 47
1772 parameters interact nonlinearly ($\sigma/\mu^* > 1.0$ for every parameter; Section 7.3.4). While
1773 this is a realistic property of complex biological systems, it means that the model can-
1774 not be calibrated by tuning individual parameters in isolation. Joint calibration via
1775 ABC-SMC [59] is computationally expensive ($>10^4$ model evaluations) and requires well-
1776 defined summary statistics and calibration targets, many of which are currently lacking
1777 for *Pycnopodia helianthoides*.

1778 **4. Recovery rate has zero empirical basis.** The base recovery rate ρ_{rec} is the single
1779 most influential parameter in the model (Section 7.3.1), yet whether *Pycnopodia he-*
1780 *lianthoides* can clear *V. pectenicia* infections at all is unknown. The SA finding that
1781 ρ_{rec} explains more output variance than any other parameter underscores this as the
1782 highest-priority empirical gap. Challenge-recovery experiments in captive *Pycnopodia*
1783 *helianthoides* [54] could provide direct estimates of clearance probability as a function of
1784 dose, temperature, and individual genotype.

1785 **5. Spatial resolution.** The validation runs use 5–11 nodes, far below the 150+ nodes
1786 needed to represent the full NE Pacific range of *Pycnopodia helianthoides* at ecologically
1787 meaningful resolution. Scaling analysis (Section 7.1) confirms computational feasibility
1788 (~ 72 s for 75,000 agents, 150 nodes), but the reduced-node configurations used here may
1789 underestimate the importance of spatial heterogeneity, as demonstrated by the dramatic
1790 rank gains of spatial parameters between R3 (3 nodes) and R4 (11 nodes).

1791 9.6 Future Directions

1792 9.6.1 ABC-SMC Calibration

1793 The immediate next step is formal calibration using approximate Bayesian computation
1794 with sequential Monte Carlo sampling (ABC-SMC). Summary statistics will include:

1795 (i) range-wide population decline (>90% crash within 2 years of disease introduction),
1796 (ii) latitudinal mortality gradient [23], (iii) fjord protection effect [17], (iv) allele frequency
1797 shifts at outlier loci [60], and (v) disease progression timelines from challenge experiments
1798 [54]. The R4 SA results (Table 12) provide a natural prioritization: the top 10–15
1799 parameters can be calibrated jointly while fixing the remaining 32–37 at their default
1800 values with minimal loss of model fidelity.

1801 9.6.2 Conservation Scenario Evaluation

1802 A conservation module is under development to simulate specific management interven-
1803 tions:

- 1804 • Captive-bred release: number, timing, location, and genetic composition of released
1805 cohorts, parameterized from AZA SAFE protocols [5];
- 1806 • Assisted gene flow: introduction of cryopreserved gametes from genetically diverse
1807 wild-caught founders [22];
- 1808 • Marine protected areas: local reduction of environmental stressors that may interact
1809 with disease susceptibility.

1810 Outplanting data from the 2024 San Juan Islands release [57] and the December 2025
1811 Monterey outplanting [66] will provide empirical validation targets for captive-bred sur-
1812 vival post-release.

1813 9.6.3 Full Coastline Network

1814 Expanding the spatial network to 150 nodes spanning the full NE Pacific range of *Pyc-
1815 cnopodia helianthoides* (Baja California to the Aleutian Islands) will test whether the
1816 patterns identified at 5–11 nodes—the north–south mortality gradient, fjord protection,
1817 Monterey resilience—scale to the full metapopulation. The overwater distance matrix for
1818 489 candidate sites has been computed (Section 6), and computational scaling analysis
1819 confirms feasibility (~66 s for 150 nodes; Section 7.1).

1820 9.6.4 Integration with Empirical Data

1821 The publication of the *Pycnopodia helianthoides* reference genome [62] enables future
1822 GWAS to identify resistance-, tolerance-, and recovery-associated loci, providing direct
1823 calibration targets for the genetic architecture parameters ($n_{\text{resistance}}$, $n_{\text{tolerance}}$, n_{recovery} ,
1824 trait-specific effect size distributions). The Koch’s-postulates confirmation of *V. pecteni-
1825 cida* as the causative agent [54] opens the door to controlled challenge experiments that
1826 can estimate dose-dependent infection probability, stage-specific duration, recovery rate,
1827 and temperature sensitivity—the parameters that the SA identifies as most influential.

1828 Combining these empirical constraints with ABC-SMC calibration will substantially re-
1829 duce parametric uncertainty and increase confidence in conservation scenario predictions.

1830 **9.7 Conclusions**

1831 SSWD-EvoEpi provides a comprehensive computational framework for exploring the eco-
1832 evolutionary dynamics of SSWD in *Pycnopodia helianthoides*. The model reveals that
1833 evolutionary rescue through natural selection on polygenic resistance is insufficient to
1834 prevent population collapse on conservation timescales, that pathogen clearance (recov-
1835 ery) rather than infection prevention (resistance) is the primary adaptive pathway, and
1836 that the extinction vortex persists at ecologically realistic population sizes. These find-
1837 ings reinforce the scientific case for captive breeding and managed release as the essential
1838 conservation strategy for this critically endangered species. The four-round sensitivity
1839 analysis establishes clear priorities for empirical research—recovery rate, environmental
1840 pathogen pressure, genetic architecture, and growth rate—that will enable formal model
1841 calibration and, ultimately, quantitative predictions for guiding *Pycnopodia helianthoides*
1842 recovery efforts across the northeastern Pacific.

1843 **References**

- 1844 [1] Emilius A. Aalto, Kevin D. Lafferty, Susanne H. Sokolow, Richard E. Grewelle,
1845 Tal Ben-Horin, Charles A. Boch, Peter T. Raimondi, Steven J. Bograd, Elliott L.
1846 Hazen, Michael G. Jacox, Fiorenza Micheli, and Giulio A. De Leo. Models with
1847 environmental drivers offer a plausible mechanism for the rapid spread of infectious
1848 disease outbreaks in marine organisms. *Scientific Reports*, 10:5975, 2020. doi: 10.
1849 1038/s41598-020-62118-4.
- 1850 [2] Citlalli A. Aquino, Ryan M. Besemer, Christopher M. DeRito, Jan Kocian, Ian R.
1851 Porter, Peter T. Raiber, John E. Episale, and Ian Hewson. Evidence that microor-
1852 ganisms at the animal-water interface drive sea star wasting disease. *Frontiers in*
1853 *Microbiology*, 11:610009, 2021. doi: 10.3389/fmicb.2020.610009.
- 1854 [3] Einar Árnason, Jere Koskela, Katrín Halldórsdóttir, and Bjarki Eldon. Sweepstakes
1855 reproductive success via pervasive and recurrent selective sweeps. *eLife*, 12:e80781,
1856 2023. doi: 10.7554/eLife.80781.
- 1857 [4] Jorge Arroyo-Esquivel, Alyssa Gehman, Katie Collins, and Fernanda Sanchez. Man-
1858 aging populations after a disease outbreak: exploration of epidemiological con-
1859 sequences of managed host reintroduction following disease-driven host decline.
1860 *bioRxiv*, 2025. doi: 10.1101/2025.02.28.640833.

- 1861 [5] AZA SAFE. Sunflower sea star program plan 2024–2027. Technical report, Association
1862 of Zoos and Aquariums, 2024.
- 1863 [6] Jenn M. Burt, M. Tim Tinker, Daniel K. Okamoto, Kyle W. Demes, Katie Holmes,
1864 and Anne K. Salomon. Sudden collapse of a mesopredator reveals its complementary
1865 role in mediating rocky reef regime shifts. *Proceedings of the Royal Society B*, 285:
1866 20180553, 2018. doi: 10.1098/rspb.2018.0553.
- 1867 [7] California Ocean Protection Council. Staff recommendation item 9: Consideration
1868 and approval of disbursement of funds to support sunflower sea star reintroduction.
1869 Technical report, California Ocean Protection Council, 2025.
- 1870 [8] Francesca Campolongo, Jessica Cariboni, and Andrea Saltelli. An effective screening
1871 design for sensitivity analysis of large models. *Environmental Modelling & Software*,
1872 22(10):1509–1518, 2007. doi: 10.1016/j.envsoft.2006.10.004.
- 1873 [9] Matthew Clement, Rodrigo Hamede, Menna E. Jones, and Paul A. Hohenlohe.
1874 Coevolution enables host persistence in an eco-evolutionary epidemiological model
1875 of Tasmanian devil facial tumor disease. *Evolution*, 78(12):2095–2110, 2024. doi:
1876 10.1093/evolut/qpae143.
- 1877 [10] Matthew Clement et al. Eco-evolutionary individual-based model for coevolution
1878 between Tasmanian devils and devil facial tumour disease. *Evolution*, 2024. doi:
1879 10.1093/evolut/qpae143.
- 1880 [11] Donald L. DeAngelis and Wolf M. Mooij. Individual-based modeling of ecological
1881 and evolutionary processes. *Annual Review of Ecology, Evolution, and Systematics*,
1882 36:147–168, 2005. doi: 10.1146/annurev.ecolsys.36.102003.152644.
- 1883 [12] Michael L. Dungan, Thomas E. Miller, and Donald A. Thomson. Catastrophic
1884 decline of a top carnivore in the Gulf of California rocky intertidal zone. *Science*,
1885 216:989–991, 1982. doi: 10.1126/science.216.4549.989.
- 1886 [13] Morgan E. Eisenlord, Maya L. Groner, Robin M. Yoshioka, Jennifer Elliott, Jeffrey
1887 Maynard, Steven Fradkin, Margaret Turner, Katie Pyne, Sandy Wyllie-Echeverria,
1888 Benjamin G. Miner, and C. Drew Harvell. Ochre star mortality during the 2014
1889 wasting disease epizootic: role of population size and temperature. *Philosophical
1890 Transactions of the Royal Society B*, 371(1689):20150212, 2016. doi: 10.1098/rstb.
1891 2015.0212.
- 1892 [14] Bjarki Eldon and Wolfgang Stephan. Sweepstakes reproduction facilitates rapid
1893 adaptation in highly fecund populations. *Molecular Ecology*, 33:e16903, 2024. doi:
1894 10.1111/mec.16903.

- 1895 [15] Aaron W. E. Galloway, Sarah A. Gravem, Jenna N. Kobelt, et al. Sunflower sea
1896 star predation on urchins can facilitate kelp forest recovery. *Proceedings of the Royal*
1897 *Society B*, 290:20221897, 2023. doi: 10.1098/rspb.2022.1897.
- 1898 [16] Joanna C. Gascoigne and Romuald N. Lipcius. Allee effects in marine systems.
1899 *Marine Ecology Progress Series*, 269:49–59, 2004. doi: 10.3354/meps269049.
- 1900 [17] Alyssa-Lois M. Gehman, Olivier Pontier, Tanya Froese, Derek VanMaanen, Tris-
1901 tian Blaine, Gillian Sadlier-Brown, Alexis M. Olson, Zachary L. Monteith, Kite-
1902 ria Bachen, Christy Prentice, Margot Hessing-Lewis, and Jennifer M. Jackson.
1903 Fjord oceanographic dynamics provide refuge for critically endangered *Pycnopo-*
1904 *dia helianthoides*. *Proceedings of the Royal Society B*, 292:20242770, 2025. doi:
1905 10.1098/rspb.2024.2770.
- 1906 [18] Àlex Giménez-Romero, Antoni Grau, Iris E. Hendriks, and Manuel A. Matías. Mod-
1907 ellling parasite-produced marine diseases: The case of the mass mortality event of
1908 *Pinna nobilis*. *Ecological Modelling*, 459:109740, 2021. doi: 10.1016/j.ecolmodel.
1909 2021.109740.
- 1910 [19] Sarah A. Gravem and Bruce A. Menge. Metapopulation-scale resilience to disease-
1911 induced mass mortality in a keystone predator: From stasis to instability. *Ecosphere*,
1912 16:e70426, 2025. doi: 10.1002/ecs2.70426.
- 1913 [20] Sarah A. Gravem, Walter N. Heady, Vienna R. Saccomanno, Kathleen F. Alvstad,
1914 Alyssa-Lois M. Gehman, Taylor N. Frierson, and Scott L. Hamilton. *Pycnopodia*
1915 *helianthoides*. *The IUCN Red List of Threatened Species*, 2021. doi: 10.2305/IUCN.
1916 UK.2021-1.RLTS.T178290276A197818455.en.
- 1917 [21] Volker Grimm and Steven F. Railsback. *Individual-Based Modeling and Ecology*.
1918 Princeton University Press, Princeton, NJ, 2005.
- 1919 [22] Mary Hagedorn et al. Assisted gene flow using cryopreserved sperm in critically en-
1920 dangered coral. *Proceedings of the National Academy of Sciences*, 118:e2110559118,
1921 2021. doi: 10.1073/pnas.2110559118.
- 1922 [23] Scott L. Hamilton et al. Disease-driven mass mortality event leads to widespread
1923 extirpation and variable recovery potential of a marine predator across the eastern
1924 Pacific. *Proceedings of the Royal Society B*, 288:20211195, 2021. doi: 10.1098/rspb.
1925 2021.1195.
- 1926 [24] C. Drew Harvell, Diego Montecino-Latorre, Joseph M. Caldwell, Jenn M. Burt,
1927 Kathryn Bosley, et al. Disease epidemic and a marine heat wave are associated
1928 with the continental-scale collapse of a pivotal predator (*Pycnopodia helianthoides*).
1929 *Science Advances*, 5:eaau7042, 2019. doi: 10.1126/sciadv.aau7042.

- 1930 [25] C. Drew Harvell, Diego Montecino-Latorre, Joseph M. Caldwell, Jenn M. Burt,
1931 Kathryn Bosley, et al. Disease epidemic and a marine heat wave are associated
1932 with the continental-scale collapse of a pivotal predator (*Pycnopodia helianthoides*).
1933 *Science Advances*, 5:eaau7042, 2019. doi: 10.1126/sciadv.aau7042.
- 1934 [26] Walter N. Heady, Rodrigo Beas-Luna, Michael N. Dawson, et al. Roadmap to re-
1935 covery for the sunflower sea star along the West Coast of North America. Technical
1936 report, The Nature Conservancy, 2022.
- 1937 [27] Dennis Hedgecock and Alexander I. Pudovkin. Sweepstakes reproductive success
1938 in highly fecund marine fish and shellfish: A review and commentary. *Bulletin of*
1939 *Marine Science*, 87:971–1002, 2011. doi: 10.5343/bms.2010.1051.
- 1940 [28] Jon Herman and Will Usher. SALib: An open-source Python library for sensitivity
1941 analysis. *Journal of Open Source Software*, 2(9):97, 2017. doi: 10.21105/joss.00097.
- 1942 [29] Ian Hewson. Microbial respiration in the asteroid diffusive boundary layer influenced
1943 sea star wasting disease during the 2013–2014 northeast Pacific Ocean mass mortality
1944 event. *Marine Ecology Progress Series*, 668:231–237, 2021. doi: 10.3354/meps13710.
- 1945 [30] Ian Hewson. When bacteria meet many arms: Autecological insights into *Vibrio*
1946 *pectinicida* FHCF-3 in echinoderms. *bioRxiv*, 2025. doi: 10.1101/2025.08.15.670479.
- 1947 [31] Ian Hewson, Jason B. Button, Brent M. Gudenkauf, et al. Densovirus associated with
1948 sea-star wasting disease and mass mortality. *Proceedings of the National Academy of Sciences*,
1949 111:17278–17283, 2014. doi: 10.1073/pnas.1416625111.
- 1950 [32] Ian Hewson, Morgan R. Johnson, and Benjamin Reyes-Chavez. Lessons learned
1951 from the sea star wasting disease investigation. *Annual Review of Marine Science*,
1952 17:257–279, 2025. doi: 10.1146/annurev-marine-040623-082617.
- 1953 [33] Ian Hewson et al. Investigating the complex association between viral ecology, envi-
1954 ronment, and Northeast Pacific sea star wasting. *Frontiers in Marine Science*, 5:77,
1955 2018. doi: 10.3389/fmars.2018.00077.
- 1956 [34] Ian Hewson et al. Perspective: Something old, something new? Review of wasting
1957 and other mortality in Asteroidea (Echinodermata). *Frontiers in Marine Science*, 6:
1958 406, 2019. doi: 10.3389/fmars.2019.00406.
- 1959 [35] Jason Hodin, Amanda Pearson-Lund, Freya P. Anteau, Philippe Kitaeff, and Sarah
1960 Cefalu. Progress toward complete life-cycle culturing of the endangered sunflower
1961 star, *Pycnopodia helianthoides*. *Biological Bulletin*, 241:243–258, 2021. doi: 10.1086/
1962 716552.

- 1963 [36] Ilse Höllinger, Pleuni S. Pennings, and Joachim Hermissen. Polygenic adaptation:
1964 From sweeps to subtle frequency shifts. *eLife*, 11:e66697, 2022. doi: 10.7554/eLife.
1965 66697.
- 1966 [37] Matthew C. Kay and Richard B. Emlet. Laboratory spawning, larval development,
1967 and metamorphosis of the lace coral *Stylaster roseus*. *Invertebrate Biology*, 121:
1968 325–338, 2002. Movement speed reference for *Pycnopodia*: 0.5 m/min.
- 1969 [38] C. Lambert, J.-L. Nicolas, V. Cilia, and S. Corre. *Vibrio pectenicida* sp. nov., a
1970 pathogen of scallop (*Pecten maximus*) larvae. *International Journal of Systematic*
1971 *Bacteriology*, 48:481–487, 1998. doi: 10.1099/00207713-48-2-481.
- 1972 [39] Ryan E. Langendorf, James A. Estes, James C. Watson, Michael C. Kenner, Brian B.
1973 Hatfield, M. Tim Tinker, Elizabeth Waddle, Michelle L. DeMarch, and Daniel F.
1974 Doak. Dynamic and context-dependent keystone species effects in kelp forests. *Proceedings of the National Academy of Sciences*, 2025. doi: 10.1073/pnas.XXXXXXX.
- 1976 [40] Harilaos A. Lessios. The great *Diadema antillarum* die-off: 30 years
1977 later. *Annual Review of Marine Science*, 8:267–283, 2016. doi: 10.1146/
1978 annurev-marine-122414-033857.
- 1979 [41] Katie E. Lotterhos and Michael C. Whitlock. The relative power of genome scans to
1980 detect local adaptation depends on sampling design and statistical method. *Molecular*
1981 *Ecology*, 24(5):1031–1046, 2015. doi: 10.1111/mec.13100.
- 1982 [42] Dayv Lowry, Sarah Wright, Melissa Neuman, et al. Endangered Species Act status
1983 review report: Sunflower sea star (*Pycnopodia helianthoides*). Technical report,
1984 NOAA National Marine Fisheries Service, 2022.
- 1985 [43] Carolyn J. Lundquist and Louis W. Botsford. Model projections of the fishery
1986 implications of the Allee effect in broadcast spawners. *Ecological Applications*, 14:
1987 929–941, 2004. doi: 10.1890/02-5325.
- 1988 [44] Coralie Lupo, Pedro J. Cabello-Yeves, Sara Ferreira, Julien de Lorgeril, and Luigi
1989 Vezzulli. Vibrio ecology, pathogenesis, and evolution. *Frontiers in Microbiology*, 11:
1990 587685, 2020. doi: 10.3389/fmicb.2020.587685.
- 1991 [45] Coralie Lupo et al. Spatial epidemiological modelling of infection by *Vibrio aestuari-*
1992 *anus* shows that connectivity and temperature control oyster mortality. *Aquaculture*
1993 *Environment Interactions*, 12:511–527, 2020. doi: 10.3354/aei00379.
- 1994 [46] Michael Lynch. Evolution of the mutation rate. *Trends in Genetics*, 26:345–352,
1995 2010. doi: 10.1016/j.tig.2010.05.003.

- 1996 [47] Ryan T. Mancuso, Sarah A. Gravem, Rachel S. Campbell, Nathan Hunter, Pete
1997 Raimondi, Aaron W. E. Galloway, and Kristy J. Kroeker. Sunflower sea star chemical
1998 cues locally reduce kelp consumption by eliciting a flee response in red sea urchins.
1999 *Proceedings of the Royal Society B*, 2025. doi: 10.1098/rspb.2025.0949.
- 2000 [48] Zofia D. Meunier, Sally D. Hacker, and Bruce A. Menge. Regime shifts in rocky
2001 intertidal communities associated with a marine heatwave and disease outbreak.
2002 *Nature Ecology & Evolution*, 8:1285–1297, 2024. doi: 10.1038/s41559-024-02425-5.
- 2003 [49] C. Melissa Miner, Jennifer L. Burnaford, Richard F. Ambrose, Liam Antrim, et al.
2004 Large-scale impacts of sea star wasting disease (SSWD) on intertidal sea stars and
2005 implications for recovery. *PLoS ONE*, 13:e0192870, 2018. doi: 10.1371/journal.pone.
2006 0192870.
- 2007 [50] Diego Montecino-Latorre, Morgan E. Eisenlord, Morgan Turner, Reyn Yoshioka,
2008 C. Drew Harvell, et al. Devastating transboundary impacts of sea star wasting
2009 disease on subtidal asteroids. *PLoS ONE*, 11:e0163190, 2016. doi: 10.1371/journal.
2010 pone.0163190.
- 2011 [51] Diego Montecino-Latorre, Morgan E. Eisenlord, Morgan Turner, Reyn Yoshioka,
2012 C. Drew Harvell, et al. Devastating transboundary impacts of sea star wasting
2013 disease on subtidal asteroids. *PLoS ONE*, 11:e0163190, 2016. doi: 10.1371/journal.
2014 pone.0163190.
- 2015 [52] Max D. Morris. Factorial sampling plans for preliminary computational experiments.
2016 *Technometrics*, 33(2):161–174, 1991. doi: 10.1080/00401706.1991.10484804.
- 2017 [53] NOAA National Centers for Environmental Information. NOAA optimum interpolation
2018 SST (OISST) version 2.1, 2020. URL <https://www.ncei.noaa.gov/products/optimum-interpolation-sst>.
- 2020 [54] Maya B. Prentice, Citlalli A. Aquino, Amy M. Chan, Kalia M. Davis, Paul K. Her-
2021 shberger, Jan F. Finke, Jason Hodin, Aquiala McCracken, Christina T. E. Kellogg,
2022 Rute B. G. Clemente-Carvalho, Christy Prentice, Kiana X. Zhong, C. Drew Harvell,
2023 Curtis A. Suttle, and Alyssa-Lois M. Gehman. *Vibrio pectenicida* strain FHCF-3 is
2024 a causative agent of sea star wasting disease. *Nature Ecology & Evolution*, 2025. doi:
2025 10.1038/s41559-025-02797-2.
- 2026 [55] Lars Råberg, Andrea L. Graham, and Andrew F. Read. Decomposing health: toler-
2027 ance and resistance to parasites in animals. *Philosophical Transactions of the Royal*
2028 *Society B*, 364(1513):37–49, 2009. doi: 10.1098/rstb.2008.0184.

- 2029 [56] Laura Rogers-Bennett and Cynthia A. Catton. Marine heat wave and multiple
2030 stressors tip bull kelp forest to sea urchin barrens. *Scientific Reports*, 9:15050, 2019.
2031 doi: 10.1038/s41598-019-51114-y.
- 2032 [57] John Ryan. San juans' sea stars start long crawl back from near-extinction. KUOW, August 2024. URL <https://www.kuow.org/stories/san-juans-sea-stars-start-long-crawl-back-from-near-extinction>.
- 2035 [58] Andrea Saltelli. Making best use of model evaluations to compute sensitivity indices. *Computer Physics Communications*, 145(2):280–297, 2002. doi: 10.1016/S0010-4655(02)00280-1.
- 2038 [59] Andrea Saltelli, Marco Ratto, Terry Andres, Francesca Campolongo, Jessica Cariboni, Debora Gatelli, Michaela Saisana, and Stefano Tarantola. *Global Sensitivity Analysis: The Primer*. John Wiley & Sons, 2008. doi: 10.1002/9780470725184.
- 2041 [60] Lauren M. Schiebelhut, Jonathan B. Puritz, and Michael N. Dawson. Decimation by sea star wasting disease and rapid genetic change in a keystone species, *Pisaster ochraceus*. *Proceedings of the National Academy of Sciences*, 115:7069–7074, 2018. doi: 10.1073/pnas.1800285115.
- 2045 [61] Lauren M. Schiebelhut, Jonathan B. Puritz, and Michael N. Dawson. Decimation by sea star wasting disease and rapid genetic change in a keystone species, *Pisaster ochraceus*. *Proceedings of the National Academy of Sciences*, 115(27):7069–7074, 2018. doi: 10.1073/pnas.1800285115.
- 2049 [62] Lauren M. Schiebelhut et al. A reference genome for ecological restoration of the sunflower sea star, *Pycnopodia helianthoides*. *Journal of Heredity*, 115:86–93, 2024. doi: 10.1093/jhered/esad054.
- 2052 [63] Sea Star Lab. Sea star cryopreservation breakthrough inspires hope for sunflower stars, 2025. Press release.
- 2054 [64] Il'ya M. Sobol'. Global sensitivity indices for nonlinear mathematical models and their Monte Carlo estimates. *Mathematics and Computers in Simulation*, 55(1–3):271–280, 2001. doi: 10.1016/S0378-4754(00)00270-6.
- 2057 [65] Megumi F. Strathmann. *Reproduction and Development of Marine Invertebrates of the Northern Pacific Coast*. University of Washington Press, Seattle, 1987.
- 2059 [66] Sunflower Star Laboratory. First temporary experimental out-
2060 planting of sunflower stars in California. SSL Press Release, December 2025. URL <https://www.sunflowerstarlab.org/news/sunflower-stars-restoration-research-california>.

- 2063 [67] Stephen E. Swearer, Jeffrey S. Shima, Michael E. Hellberg, Simon R. Thorrold,
 2064 Geoffrey P. Jones, D. Ross Robertson, Steven G. Morgan, Kimberly A. Selkoe, Gre-
 2065 gory M. Ruiz, and Robert R. Warner. Evidence of self-recruitment in demersal
 2066 marine populations. *Bulletin of Marine Science*, 70:251–271, 2002.
- 2067 [68] Nick Tolimieri. Appendix A: Population viability analysis of *Pycnopodia hel-
 2068 lianthoides*. In: Lowry et al., *ESA Status Review Report, NOAA NMFS*, 2022.
- 2069 [69] David L. J. Vendrami, Lloyd S. Peck, Melody S. Clark, Bjarki Eldon, Michael Mered-
 2070 ith, and Joseph I. Hoffman. Sweepstake reproductive success and collective dispersal
 2071 produce chaotic genetic patchiness in a broadcast spawner. *Science Advances*, 7:
 2072 eabj4713, 2021. doi: 10.1126/sciadv.abj4713.
- 2073 [70] Malavika Vyawahare. There's hope for sunflower sea stars, with
 2074 their killer unmasked and reintroductions pending. Mongabay,
 2075 August 2025. URL <https://news.mongabay.com/2025/08/theres-hope-for-sunflower-sea-stars-with-their-killer-unmasked-and-reintroduction/>
- 2077 [71] John P. Wares and Lauren M. Schiebelhut. What doesn't kill them makes them
 2078 stronger: an association between elongation factor 1- α overdominance in the sea
 2079 star *Pisaster ochraceus* and "sea star wasting disease". *PeerJ*, 4:e1876, 2016. doi:
 2080 10.7717/peerj.1876.
- 2081 [72] Helen J. Wearing, Pejman Rohani, and Matt J. Keeling. Appropriate models for the
 2082 management of infectious diseases. *PLoS Medicine*, 2(7):e174, 2005. doi: 10.1371/journal.pmed.0020174.

2084 A Parameter Tables

2085 Table 17–22 list all 47 parameters included in the sensitivity analysis, grouped by module.
 2086 For each parameter we report the default value used in validation runs, the sensitivity
 2087 analysis range (low–high), the distribution used for sampling (U = uniform, LU = log-
 2088 uniform, D = discrete), and the empirical confidence rating: ★★★ = directly measured,
 2089 ★★ = constrained by related data, ★ = poorly constrained or assumed.

Table 17: Disease module parameters (16). Default values from `config.py`; SA ranges from `param_spec.py`.

Parameter	Description	Default	Range	Dist.	Conf.
a_{exposure}	Exposure rate (d^{-1})	0.75	[0.30, 1.50]	U	*
K_{half}	Half-infective dose (bact/mL)	87,000	[2×10^4 , 2×10^5]	LU	*
$\sigma_{1,\text{eff}}$	I_1 shedding rate (field-effective)	5.0	[1.0, 25.0]	LU	*
$\sigma_{2,\text{eff}}$	I_2 shedding rate (field-effective)	50.0	[10.0, 250.0]	LU	*
σ_D	Saprophytic burst (field-effective)	15.0	[3.0, 75.0]	LU	*
ρ_{rec}	Recovery rate (d^{-1})	0.05	[0.0, 0.20]	U	*
$\mu_{E \rightarrow I_1, \text{ref}}$	$E \rightarrow I_1$ progression at T_{ref}	0.57	[0.20, 1.00]	U	**
$\mu_{I_1 \rightarrow I_2, \text{ref}}$	$I_1 \rightarrow I_2$ progression at T_{ref}	0.40	[0.15, 0.80]	U	**
$\mu_{I_2 \rightarrow D, \text{ref}}$	$I_2 \rightarrow$ Death rate at T_{ref}	0.173	[0.08, 0.35]	U	**
$P_{\text{env,max}}$	Background Vibrio input (bact/mL/d)	500.0	[50.0, 5,000.0]	LU	*
T_{ref}	$V. pectenicida$ temperature optimum ($^{\circ}\text{C}$)	20.0	[17.0, 23.0]	U	**
T_{VBNC}	VBNC midpoint temperature ($^{\circ}\text{C}$)	12.0	[8.0, 15.0]	U	**
s_{min}	Salinity minimum for Vibrio (psu)	10.0	[5.0, 15.0]	U	**

Continued

Table 17 (continued)

Parameter	Description	Default	Range	Dist.	Conf.
suscept. multiplier	Post-spawning immunosuppression multiplier	2.0	[1.0, 4.0]	U	*
immunosupp. duration	Post-spawning immunosuppression (days)	28	[7, 56]	U	**
min. susceptible age	Days post-settlement before susceptible	0	[0, 180]	U	*

Table 18: Population dynamics parameters (7).

Parameter	Description	Default	Range	Dist.	Conf.
F_0	Reference fecundity (eggs)	10^7	$[10^6, 10^8]$	LU	*
γ_{fert}	Fertilization kinetics parameter	4.5	$[1.0, 10.0]$	U	*
s_0 (settler survival)	Beverton–Holt settler survival	0.03	$[0.005, 0.10]$	LU	*
α_{SRS}	SRS Pareto shape	1.35	$[1.0, 1.8]$	U	**
senescence age	Senescence onset age (yr)	50.0	$[20.0, 80.0]$	U	*
k_{growth}	von Bertalanffy growth rate (yr^{-1})	0.08	$[0.03, 0.15]$	U	*
$L_{\min,\text{repro}}$	Minimum reproductive size (mm)	400.0	$[200.0, 500.0]$	U	*

Table 19: Genetics module parameters (8). The three-trait partition is constrained: $n_{\text{resistance}} + n_{\text{tolerance}} + n_{\text{recovery}} = 51$.

Parameter	Description	Default	Range	Dist.	Conf.
$n_{\text{resistance}}$	Number of resistance loci	17	{5, 10, 17, 25, 30}	D	★★
$n_{\text{tolerance}}$	Number of tolerance loci	17	{5, 10, 17, 25, 30}	D	★★
target_mean_r	Target mean resistance at $t = 0$	0.15	[0.05, 0.30]	U	★
target_mean_t	Target mean tolerance at $t = 0$	0.10	[0.02, 0.30]	U	★
target_mean_c	Target mean recovery at $t = 0$	0.02	[0.02, 0.25]	U	★
τ_{\max}	Max tolerance mortality reduction	0.85	[0.30, 0.95]	U	★
q_{init, β_a}	Beta shape a for allele freq. init.	2.0	[1.0, 5.0]	U	★
q_{init, β_b}	Beta shape b for allele freq. init.	8.0	[3.0, 15.0]	U	★

Table 20: Spawning module parameters (7).

Parameter	Description	Default	Range	Dist.	Conf.
$p_{\text{spont,f}}$	Daily spontaneous female spawning prob.	0.012	[0.005, 0.025]	U	**
$p_{\text{spont,m}}$	Daily spontaneous male spawning prob.	0.0125	[0.005, 0.025]	U	**
κ_{fm}	Female→male cascade induction prob.	0.80	[0.40, 0.95]	U	**
κ_{mf}	Male→female cascade induction prob.	0.60	[0.10, 0.60]	U	**
σ_{spawn}	Spawning peak width (std dev, days)	60.0	[30.0, 90.0]	U	**
readiness ind. prob.	Social spawning readiness induction	0.50	[0.10, 0.80]	U	*
female max bouts	Max spawning bouts per female per season	2	{1, 2, 3}	D	**

 ∞

Table 21: Spatial module parameters (3).

Parameter	Description	Default	Range	Dist.	Conf.
D_L	Larval dispersal scale (km)	400.0	[100.0, 1,000.0]	LU	★
$\alpha_{\text{self,fjord}}$	Larval self-recruitment (fjord)	0.30	[0.10, 0.50]	U	★
$\alpha_{\text{self,open}}$	Larval self-recruitment (open coast)	0.10	[0.02, 0.20]	U	★

Table 22: Pathogen evolution module parameters (6).

Parameter	Description	Default	Range	Dist.	Conf.
α_{kill}	Death rate scaling exponent	2.0	[1.0, 4.0]	U	★
α_{shed}	Shedding rate scaling exponent	1.5	[0.5, 3.0]	U	★
α_{prog}	$I_1 \rightarrow I_2$ progression scaling exp.	1.0	[0.5, 2.0]	U	★
γ_{early}	Early shedding attenuation factor	0.3	[0.0, 1.0]	U	★
$\sigma_{v,\text{mut}}$	Virulence mutation step size (std dev)	0.02	[0.005, 0.10]	LU	★
v_{init}	Initial pathogen virulence	0.5	[0.2, 0.8]	U	★